Gold nanoparticles as platform for investigating epidermal growth factor receptor activation and intestinal epithelium cell metabolomics

BOSTON UNIVERSITY

GRADUATE SCHOOL OF ARTS AND SCIENCES

Dissertation

GOLD NANOPARTICLES AS PLATFORM FOR INVESTIGATING EPIDERMAL GROWTH FACTOR RECEPTOR ACTIVATION AND INTESTINAL EPITHELIUM CELL METABOLOMICS

by

QIANYUN ZHANG

B.S., University of Minnesota -Twin Cities, 2015

Submitted in partial fulfillment of the

requirements for the degree of

Doctor of Philosophy

2021

Approved by

First Reader

Björn M. Reinhard, PhD
Professor of Chemistry

Second Reader

Lawrence D. Ziegler, PhD
Professor of Chemistry

DEDICATION

To my dearest parents, I would like to dedicate this work to you. Thank you for always being supportive and respects over years. Your unconditional love has helped immensely during my pursuit of a PhD. Without you, this work would not be possible.

I would also like to thank Professor Björn M. Reinhard, my academic advisor for his guidance and help. His dedication and enthusiasm for science encourage me to pursue in this field. I feel fortunate to have him as my mentor.

And lastly, I would like to dedicate this work to lovely Hanqing Wang, thank you for taking care of me, giving me spiritual and emotional support under this special circumstances. You fill my life with love and happiness

GOLD NANOPARTICLES AS PLATFORM FOR INVESTIGATING EPIDERMAL GROWTH FACTOR RECEPTOR ACTIVATION AND INTESTINAL EPITHELIUM CELL METABOLOMICS

QIANYUN ZHANG

Boston University Graduate School of Arts and Sciences, 2021

Major Professor: Björn M. Reinhard, Professor of Chemistry

ABSTRACT

Gold nanoparticles (Au NPs) exhibit unique optical and electronic properties due to localized surface plasmon resonance (LSPR), which arises from the collective oscillation of conduction electrons on the surface of AuNPs. Plasmon coupling results in the dramatic enhancement and confinement of the electric field. The distance-dependency of the plasmon coupling and local -field enhancement have been exploited for a variety of sensing techniques. Multivalent presentation of ligands on NPs is considered a general strategy for enhancing receptor binding and activation through amplification of ligand-receptor interactions within the footprint of the NPs. To understand the interplay between ligand density and epidermal growth factor receptor (EGFR) clustering in signal amplification, we apply EGF-functionalized NP with known ligand loading as quantifiable and tractable units of EGFR activation and characterize the NP-mediated amplification of EGFR phosphorylation as function of both EGF surface density and NP-EGF. The measurements confirm that NP-EGF-clustering and the associated local

enhancement of ligand-receptor interactions are intrinsic components of the multivalent amplification of phosphorylation for the heterogeneously distributed EGFR through NP-EGF.

To investigate the potential perturbation of nanoplastics on the protective function of the intestinal membrane, we use unpatterned gold nanoparticles as Surface Enhanced Raman Spectroscopy (SERS) substrate to monitor the composition of the medium in direct contact with the intestinal cells and to detect potential polystyrene NP induced changes in the cellular metabolism. Reactive oxygen species (ROS) generation, cell viability, and intestinal membrane integrity measurements were also performed to detect and quantify PS NP-induced membrane damage under acute exposure conditions. The measurements reveal that PS NPs induce cellular stress and perturb the membrane integrity. The analysis of the SERS spectra through artificial intelligence algorithms and chemometric tools reveals concentration-, exposure time-, and surface chemistry-dependent differences in the cellular metabolism, and identifies increased hypoxanthine (C4H4N4O) levels as a spectroscopic marker for PS NP-induced loss in membrane integrity.

Table of Contents

List of Tables

List of Figures

LIST OF ABBREVIATIONS

Au..Gold

DLS ....Dynamic Light Scattering

E-field ....Electric Field

EGF...Epidermal Growth Factor

EM ....Electromagnetic

FIB.. Focused Ion Beam

ICP-MS.......................................Inductively Coupled Plasma Mass Spectroscopy

LDA..Linear Discriminant Analysis

IR ....Infrared

LDH...Lactate Dehydrogenase

LSPR ....Localized Surface Plasmon Resonance

MOC..Manders Overlap Coefficients

MTT..Microculture Tetrazolium

NP ....Nanoparticle

PCA...Principal Component Analysis

PCM ....Plasmon Coupling Microscopy

PCC........Pearson Correlation Coefficients

PEG........Polyethylene Glycol

pEGFR........Phosphorylated Epidermal Growth Factor Receptor

PR ....Plasmon Ruler

PS ....Polystyrene

RI ....Refractive Index

ROS........Reactive Oxygen Species

RTK........ Receptor Tyrosine Kinase

SEM ....Scanning Electron Microscopy

SERS ....Surface Enhanced Raman Spectroscopy

SPR ....Surface Plasmon Resonance

TEER........Transepithelial Electrical Resistance

TEM ....Transmission Electron Microscopy

t-SNE........ T-distributed Stochastic Neighbor Embedding

UV/vis........Ultraviolet-Visible

Chapter 1 Introduction

1.1 Light Scattering at Gold Nanoparticles

Gold Nanoparticles (Au NPs) have fascinating photophysical properties and provide a promising platform for sensing and biosensing.[1-3] Light scattering at Au NP excites plasmon resonances, that give rise to large light scattering cross sections and plasmon-enhanced phenomena.[1] Plasmons are collective oscillations of conduction band electrons that occur at a well-defined frequency in metals.[1-3] Plasmons in nanoparticles (NPs) with sizes much smaller than the photon wavelength are non-propagating excitations. These localized surface plasmons resonances (LSPR) are surface charge density oscillations (Figure 1.1)[2] that can generate strong local electric (E-) fields in the vicinity of the nanoparticles. Electromagnetic radiation (EM) with a frequency in resonance with the LSPR can excite the latter, and the driven electron cloud oscillates like a simple dipole in the direction of the E-field of the incident electromagnetic radiation.[2,3] A simple mass-on-a-spring damped oscillator model has been

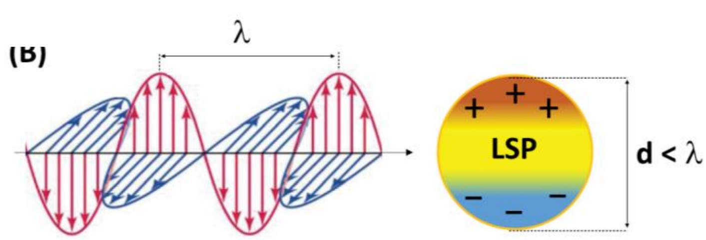

Figure 1.1 Graphical illustration of plasmons in Au NP. Localized surface plasmons are excited by light propagating in free space or dielectric media. Reprinted with permission from reference 1, ©2017 IOP Publishing.

utilized in the semi-quantitative understanding of plasmonic systems.[3] In the case of a spherical Au NP, the quasistatic expression of the scattering and absorption cross-section are:

$$\sigma_{sca} = \frac{2\pi^4 D^6}{3\lambda^4}\left[\frac{\varepsilon(\lambda)-\varepsilon_m(\lambda)}{\varepsilon(\lambda)+2\varepsilon_m(\lambda)}\right]^2 \tag{1}$$

$$\sigma_{abs} = \frac{\pi D^3}{\lambda} Im\left[\frac{\varepsilon(\lambda)-\varepsilon_m(\lambda)}{\varepsilon(\lambda)+2\varepsilon_m(\lambda)}\right] \tag{2}$$

where λ is the light wavelength, ε_m is the dielectric constant of the surrounding medium, D is the diameter of NP, and $\varepsilon(\lambda)$ is the wavelength dependent complex dielectric function. From equations (1) and (2), the plasmonic properties of Au NPs are defined by its dielectric function. The frequency of the LSPR is tunable by changing the ε_m of the surrounding medium, the NP size, and shape. The LSPR band detected in the optical extinction spectrum of Au NP colloid has contribution from scattering and absorption. The extinction cross-section of an Au NP can be expressed as sum of the absorption and scattering terms: $\sigma_{ext} = \sigma_{sca} + \sigma_{abs}$. The scattering and absorption cross-sections of Au NPs scale as D^6 and D^3, respectively. The two effects become comparable for Au NPs with diameters of about 50 nm, and scattering prevails for Au NP with diameters above 70-100 nm.[4] As Au NPs size gets bigger, the convex shape of the surface becomes flatter, the particles absorb less light and less inelastic scattering, which leads to weakening of electromagnetic field on the surface. The size dependence of σ_{sca} and σ_{abs} are relevant for applications related to optical extinction, so careful tuning of Au NPs size are exploited for optimal performances for bio-labelling and sensing with single-particle sensitivity.

1.2 Plasmon Coupling

Plasmons on individual NPs create time-dependent electromagnetic fields, which act on the conduction band electrons of other nearby NPs.[1-3] These fields can then act back on the conduction band electrons in the original NP. Due to the sum of all of these electromagnetic “near-field” interactions, the oscillations in the individual NPs are no longer independent but coupled. This near-field coupling can be conveniently detected as a shift in the scattering spectra of the NP labels using conventional far-field light microscopy.[8-10] Plasmon hybridization can be seen as a serial coupling of two or more springs.[1,2] Au NP dimers are the simplest possible NP clusters. The dimers sustain two different bright plasmon modes; a longitudinal and a vertical mode. The longitudinal mode has a larger optical cross-section and dominates the spectrum under unpolarized whitelight excitation.[5] The spectrum of the longitudinal mode is redshifted relative the resonance of an individual NP, and the redshift of the longitudinal plasmon mode in Au NP dimers decay near-exponentially with the interparticle gap over a distance:

$$\frac{\Delta\lambda_{SPR}}{\lambda_{SPR}} = Kexp(\frac{s/D}{0.23}) \qquad (3)$$

where K is constant depending on particle geometry and dielectric environment, s is the interparticle distance. The exact resonance wavelength of an Au NP or an Au NP assembly also depends on the refractive index, n_r ($n_r = {\varepsilon_m}^{1/2}$) of the ambient medium.[5-7]

The correlation between plasmon resonance wavelength and interparticle separation can be utilized to monitor distances between NPs at a constant refractive index (Fig. 1.2).[8] In the Au NP clusters containing more than two

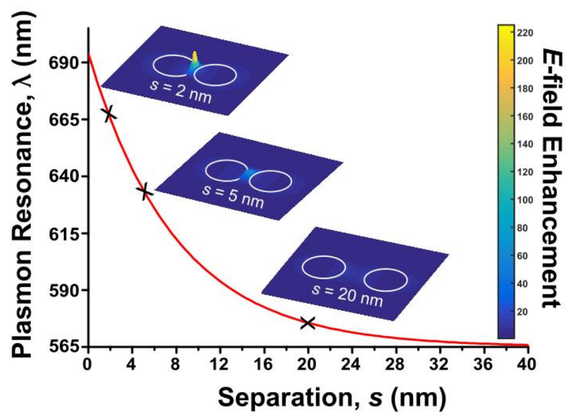

Figure 1.2 Plasmon coupling of 40 nm Au dimers. Insets show near-field maps for of NP dimers with interparticle separation (s) of 2, 5, and 20 nm, indicating increasing of E-field as s decreases. Reprinted with permission from reference 3, © 2017 World Scientific Publishing Co Pte Ltd.

NPs, the measured resonance wavelength is no longer determined by the interparticle separation alone but also depends on the number of NPs in the cluster and their geometric arrangement.[6,7] Spatial maps of plasmon coupling encode information of the local degree of NP clustering, so the cluster geometry and electromagnetic response can be accurately predicated and tuned via electromagnetic field simulation.[6-8] In particular, the generalized multiparticle Mie theory can be used to obtain the Maxwell's equations for the light scattered from coupled Au NPs. Through Mie theory simulations, the far-field scattering efficiency peaks at a larger nanoparticle size than the near-field intensity enhancement, and small particles are more efficient absorbers.[6,7] Thus, Au NPs with D= 70-80 nm emerge as the optimal elementary NP associations that combine high scattering efficiency and low absorption.[7] Through systematic characterization of the effect of the Au NP cluster configuration on its far-field scattering spectrum, the spectra collected from a diffraction limited spot in optical microscope exhibit red-shift with increasing number of Au NP in the cluster.[6,7] Therefore, the near-field coupling between lateral diffusing Au NP labels serves as an indication of the local degree of NP clustering.[9,10] The interparticle distance and geometrical arrangement dependent plasmon coupling are utilized in the Chapter 2 for monitoring cellular membrane receptor oligomerization.

1.3 Local-Field Enhancement

Excitation of the LSPR in a NP generates an increased local E-field in its immediate surrounding, and such near-field enhancement shows a volcano-type size dependence.[11] Smaller NPs suffer from nonradiative dissipation and additional field damping, whereas larger NPs have reduced field enhancements due to radiative decay and retardation.[11] The interplay of all these effects gives rise to the size dependence of near-field enhancement, which can be useful to choose the NPs most optimized for the enhancement of nonlinear optical properties in nearby objects.[5-7] The local E-field enhancement factor (EF) at a point r can be expressed as the ratio of the moduli of the local electric field E_{loc} to the incident electric field E_0:

$$EF(\vec{r}) = \frac{E_{loc}(\vec{r})}{E_0} \tag{4}$$

EF is dramatically affected by the NP structural parameters and position around the surface. The points with the largest EF in a group of them are called electromagnetic 'hot spots', which are found at the junctions between NPs.[9,10] In individual NPs in the quasistatic regime, the local field scales as $1/s^3$. This is obtained by approximating the LSPR in the Au NPs to an electric field having an oscillating dipole with dipole moment $\vec{p}$,

$$\vec{E}_{loc}(r) = \vec{E}_0 + \frac{3\vec{n}(\vec{n}\cdot\vec{p}) - \vec{p}}{4\pi\varepsilon_0\varepsilon_m s^3} \tag{5}$$

where $\vec{n}$ is the unit vector normal to the surface and pointing to the direction of interest. The decay explains why EF and hot-spot formation strongly depend on the interparticle distance. Hot spots induced by efficient coupling between Au NPs are observed for the interparticle separation lower than 0.5 times of NP diameter.[8] In the simple case of an Au NP dimer, the EF at the junction between the particles increase monotonically as the distance between the two particles is reduced to 1 nm (Figure 1.2).[3] The strong exponential dependence of the E-field intensity of the longitudinal LSPR on the dimer gap width highlights the importance of creating NP clusters with gaps below 5 nm.[7,8] Both symmetrical and asymmetrical Au NP clusters provide large near-field intensity enhancements, while asymmetrical Au NP clusters also feature multiple resonance peaks and strong polarization dependences.[7]

1.4 Surface Enhanced Raman Scattering Spectroscopy (SERS)

Raman scattering is a well-established vibrational spectroscopic technique, possessing analyte fingerprint recognition capability.[12-14] The intrinsic low efficiency of Raman scattering, typically around ~10^{-29}-10^{-31} cm^2/ molecules, can be strongly improved if molecules are placed close to the 'hot spots' of Au NPs. The surface enhanced Raman scattering signals can be expressed:

$$I_{SERS} = G_{SERS} I_{Raman} \tag{6}$$

$$G_{SERS} \sim \left(\frac{E_{loc}(v_L)}{E_0}\right)^4 \tag{7}$$

where G_{SERS} is the SERS enhancement factor, v_L is the excitation laser frequency. Equation (6) and (7) indicate that the Au NP clusters amplify the light intensity at the Au NP surface and increase the Raman scattering rate from molecules. The SERS enhancement factor, G_{SERS}, scales with E^4. In the quasistatic dipole model, the local field decays with distance from the NP surface as $1/s^3$.[13] Therefore, the efficiency of the electromagnetic enhancement quickly drops from the surface, making SERS highly selective towards molecules located in the first layers above the surface (Equation 8).

$$\frac{G_{SERS}}{G_0} = (\frac{R}{R+s})^{12} \tag{8}$$

Au NP cluster arrays have been utilized as substrates to enable SERS, and they contain holes, junctions, and crevices between few nanometer spaced Au NPs.[7,8,14] Patterned Au NP cluster arrays are observed to have higher enhancement factor due to cumulative electrodynamic interactions occurring on two different length scales: the intercluster plasmon couples and provides a first stage of strong enhancement of the incident electric field, which then further increased by the intracluster coupling between individual particles of the clusters.[7,8] However, unpatterned Au nano-structured surfaces result in a wide range of enhancement factors due to heterogeneous morphologies of the hot-spots , leading to different SERS performances. The SERS signal of an analyte not only depends on its distance of Au NP surface, but also depends on the adsorption orientation relative to the Au NP surface.[15-17] Vibrations with a change of polarizability perpendicular to the surface are most effectively enhanced due to highest coupling efficiency with the local field.[15] The Raman signal enhancement generated by Au NP clusters arrays can be maximized by matching the excitation wavelength with the dipolar resonances of the substrates.[16] In addition to their optical properties, Au NPs have several attributes that make them an ideal sensing tool: ease of synthesis,[18] chemical stability,[18,19] photophysical stability and biocompatibility[20, 21]. Au NP surface can be modified with different functionality to improve target specificity, and the high surface-to-volume ratio of Au NP enhances the binding sensitivity.[18-21] Chapter 3 reports the development and application of local field enhancement of Au NP clusters in SERS to measure biological and physiological response of cancerous cells. The plasmon-enhanced properties of Au NPs form the basis of SERS fingerprints of metabolites in the cellular process, providing a general platform on which to study cell biology.

1.5 The Scope and Organization of this Dissertation

This dissertation includes material from one publication by the author. Chapter 2 is reproduced with permission from Zhang *et al* [22]. Chapter 3 is based on unpublished work that is in submission for publication.

Chapter 2 Ligand Density and Nanoparticle Clustering Cooperate in the Multivalent Amplification of Epidermal Growth Factor Receptor Activation

Multivalent presentation of ligands on nanoparticles (NP) is considered a general strategy for enhancing receptor binding and activation through amplification of ligand-receptor interactions within the footprint of the NP. The spatial clustering of ligand-functionalized NP represents an additional, less well understood mechanism for increasing local ligand-receptor interactions, especially for receptors that form higher order assemblies, such as the epidermal growth factor (EGF) receptor (EGFR). To shed light on the interplay between ligand density (i.e. multivalency) and NP clustering in signal amplification, we apply EGF-functionalized 72±1 nm gold nanoparticles (NP-EGF) with known ligand loading (10 – 200 EGF/NP) as quantifiable and experimentally tractable units of EGFR activation and characterize the NP-mediated amplification of EGFR phosphorylation as function of both EGF surface density and NP-EGF clustering for two cancer cell lines (HeLa and MDA-MB-468). The measurements confirm a strong multivalent amplification of EGFR phosphorylation through NP-EGF on the cellular level that results in EGF-loading-dependent maximum EGFR phosphorylation levels. A microscopic analysis of NP-EGF-induced EGFR phosphorylation reveals a heterogeneous spatial distribution of EGFR activation across the cell surface. Clustering of multivalent NP-EGF on sub-diffraction limit length scales is found to result in a local enhancement of EGFR phosphorylation in signaling "hot-spots" from where the signal can spread laterally in an EGF-independent fashion. Increasing EGF loadings of the NP enhance NP-EGF clustering and intensify EGFR phosphorylation. These observations suggest that NP-EGF-clustering and the associated local enhancement of ligand-receptor interactions are intrinsic components of the multivalent amplification of phosphorylation for the heterogeneously distributed EGFR through NP-EGF.

2.1 Introduction

EGFR is a transmembrane receptor and a model receptor tyrosine kinase (RTK). EGF binding to the extracellular domain of its receptor induces a configurational change that allows receptor dimerization and subsequent cross-phosphorylation. [23-26] Effector molecules recognize the phosphorylated receptor and initiate subsequent signaling events. In cellular systems the signaling outcome is, however, subject to additional regulation mechanisms. For instance, the local signal intensity has to overcome a noise threshold to result in a measurable cellular effect. [27,28] In the case of EGFR, lateral interactions between activated and non-activated receptors facilitate a signal amplification through lateral propagation of EGFR activation. [29-33] Of particular interest from the perspective of nanomedicine is that the multivalent presentation of EGF ligands on NP

(NP-EGF) provides an alternative strategy to amplify signal activation and transduction. [34] Multivalency [35] increases the binding affinity of NP and, thus, ligand receptor-binding, [36-40] which can impact uptake rate [41] and mechanism. [42] Importantly, multiple ligand-receptor contacts within the footprint of a particle can generate a strong local receptor activation. [34,39,43,44] Previous studies applied EGF-functionalized, micron-sized beads [31,32] or surface patterns [45,46] to investigate the relationship between the "local" multivalent EGFR activation and the global EGFR phosphorylation. These studies demonstrated that an increased local EGF density can – under specific conditions – trigger a massive lateral phosphorylation propagation, but the applied probes lacked the resolution to elucidate how the spatial membrane receptor compartmentalization on sub-diffraction limit length scales affects the initial phosphorylation and its lateral spread, and were too big [47,48] for potential applications in nanomedicine.

EGFR is known to be heterogeneously distributed in the plasma membrane [49,50] and to be locally enriched in surface compartments with typical sizes on the order of 150 nm. [51] This heterogeneity in the surface distribution of EGFR is expected to aid EGFR oligomerization by creating membrane domains with high local receptor concentrations. It has been demonstrated that EGFR oligomers (assemblies larger than dimers) play an important role in enhancing the local receptor phosphorylation after initial stimulation. [50,52-54] A local enrichment of EGFR in the membrane due to receptor oligomerization or spatial confinement in a structured membrane will necessarily influence the spatial distribution of EGFR targeting NP-EGF with potential implications for signaling initiation due to a locally increased number of ligand-receptor contacts. The relationship and potential synergism between NP multivalency, NP clustering and signal amplification remains, however, insufficiently understood. To shed some light on these relationships and to elucidate potential cross-dependencies, this study characterizes EGFR phosphorylation as measure for signal initiation as function of both ligand density and NP clustering. Specifically, we apply EGF-functionalized gold nanoparticles (NP-EGF) with an approximate diameter of 72 nm and controlled EGF ligand densities as experimentally tractable stimulus of receptor activation. The binding of EGF-functionalized gold NP can be precisely measured with inductively coupled plasma mass spectroscopy (ICP-MS),[55] facilitating a quantitative characterization of the relationship between receptor phosphorylation and amount of bound ligand. Plasmonic NP also provide large cross-sections for optical detection. [56-58] Although multiple NP in a diffraction-limited spot cannot be directly resolved in conventional optical microscopy, a spatial accumulation of NP results in a measurable increase in scattering intensity ("brightness").[59] Furthermore, distance-dependent electromagnetic interactions between individual gold NP provide additional cues about their spatial organization and separation. If the separation of the NP is below approximately one NP diameter, the localized surface plasmon resonance (LSPR)[60,61] of the gold NP red-shifts due to distance-dependent plasmon coupling. [59,62-67] Scattering intensities and wavelengths are quantifiable in the far-field, [68-74] facilitating a systematic investigation of the spatial correlation between NP-EGF clustering and EGFR phosphorylation through quantitative optical darkfield microscopy. Alternative detection schemes based on differential interference contrast (DIC) have been developed, as well. [75,76] Due to advantageous physico-chemical properties and the ease of surface functionalization, gold NP-EGF are ideal probes for elucidating the relationships between ligand density, spatial NP clustering and NP-EGF enhanced EGFR phosphorylation. We emphasize that although this work focuses on EGFR as target, the findings have broader relevance as receptor oligomerization and clustering play a role in the function of other receptors than RTK.

2.2 NP Design and Characterization

All experiments were performed with approximately 72±1 diameter gold NP wrapped in a surface-assembled membrane containing the zwitterionic lipid dipalmitosylphosphatidylcholine (DPPC) and cholesterol as main components (Figure 2.1A and B). The size of the NP was chosen to maximize the optical scattering signal but still allow binding of multiple NP to EGFR-enriched membrane domains. The zwitterionic membrane coat around the NP provides a thin but efficient passivation layer of the NP surface and stabilizes the NP under the chosen experimental conditions.[78-82] The lipid layer was self-assembled around the gold NP in the presence of octadecanethiol, which binds covalently to the gold surface and generates a hydrophobic surface onto which lipids can assemble.[83,84] To facilitate the

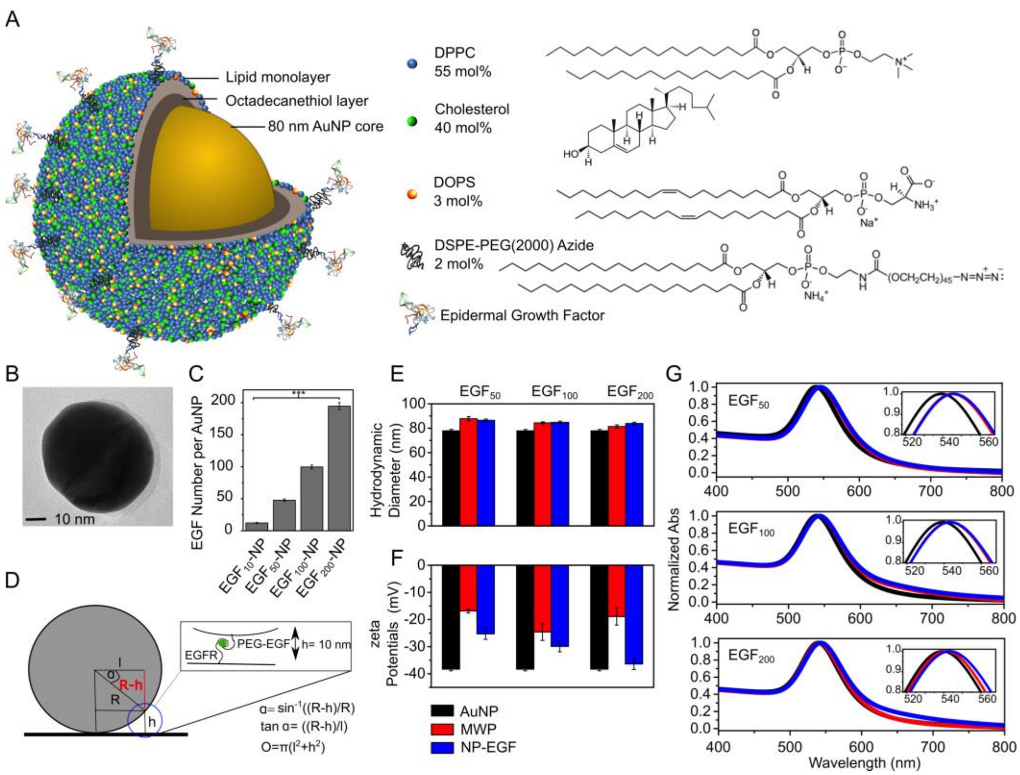

Figure 2.1 A. Schematic drawing of membrane-wrapped gold nanoparticle functionalized with EGF (NP-EGF) used in this work (left) and molecular structures and mol% of lipid components (right). The crystal structure of EGF is Protein Data Bank (pdb) structure 1JL9.[55] B. TEM image of NP-EGF. C. Number of EGF molecules bound per NP as determined by ELISA for the particles used in this study. D. Geometrical model to estimate NP surface area O that is sufficiently close to the cell surface to facilitate EGF binding to EGFR. The length of the EGFR - EGF-PEG contact is approximated as 10 nm. E. Hydrodynamic diameter and F. zeta potential for citrate stabilized gold NP (Au NP), membrane wrapped NP (MWP), and membrane wrapped NP after EGF functionalization (NP-EGF). Data are provided for NP-EGF with 50, 100, 200 EGF / NP. G. UV-Vis spectra for NP-EGF with 50, 100, 200 EGF/NP (top to bottom). The data presented in C, E, F is the average of ten independent experiments.

covalent attachment of EGF to the NP, we also included azide-terminated 1,2-Diastearoyl-sn-glycero-3-phosphoethanolamine(DSPE)-polyethylene glycol(PEG-2000) into the lipid mix to allow the introduction of alkyne-functionalized EGF using the CuI-catalyzed dipolar cycloaddition. [85] The DSPE-PEG-2000-azide provides a PEG linker of 45 ethylene glycol units between the EGF and the NP surface with a contour length of approximately 19 nm and a persistence length of 0.37 nm. [86,87] The end-to-end distance of the linker is predicted to be 3.7 nm based on the worm-like-chain estimate. [66] The conformational flexibility and contour length of the spacer linked to the compact lipid wrap provides the tethered EGF with some degree of conformational freedom. [89-91] We generated NP-EGF with average EGF loadings in the range between 10 - 200 EGF/NP (Figure 2.1C), corresponding to average ligand densities of approximately 1 EGF / 2000 nm^2 to 1 EGF / 100 nm^2. Based on the simple geometric model outlined in Figure 2.1D we estimate that these densities translate to a maximum number of approximately 1 and 25 EGF ligands, respectively, in the contact area between NP-EGF and cell surface. Figure 2.1 E and F summarizes the hydrodynamic diameters and zeta potentials of the NP before and after assembly of the membrane wrap as well as after EGF binding for different EGF surface densities. The successful membrane assembly is indicated by an increase in the hydrodynamic diameter of at least 3 nm and a less

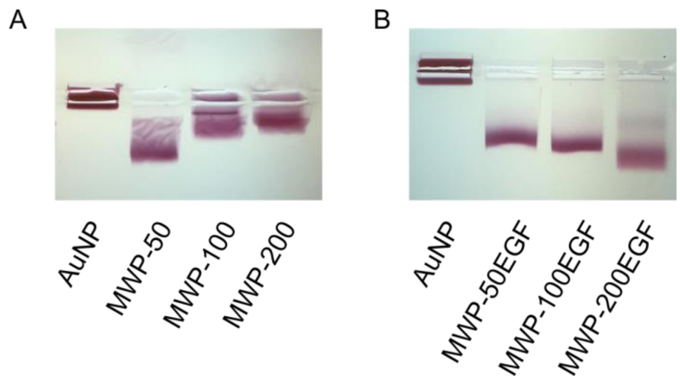

Figure 2.2. Gel electrophoresis of membrane wrapped nanoparticles with 50, 100, 200 EGF binding sites (A) before and (B) after functionalization with EGF. 100 pM solutions of NP for specified conditions were loaded in a 1% agarose gel, and run at a voltage of 150 V for 30 min. The gel running buffer was 0.5x tris/borate/edta (TBE). Citrate stabilized gold nanoparticles (AuNP) were included as reference. MWP = membrane wrapped nanoparticle.

negative zeta-potential. The latter is due to the zwitterionic nature of the lipids that generate a lower surface charge than the initial citrate ligands. Binding of EGF results only in a marginal increase in hydrodynamic diameter as the partial coverage of the surface with PEG-azide linkers bound to DSPE lipids has already expanded the hydrodynamic diameter; the small (~2.5 nm) EGF is accommodated within this PEG layer. Binding of EGF to the NP is confirmed by a decrease in zeta potential relative to the membrane-wrapped NP and by changes in gel electrophoretic mobility of the NP (Figure 2.2). The UV-Vis spectra in Figure 2.1G show a spectral red-shift of LSPR after the membrane assembly step, which is consistent with an increase in refractive index in the immediate vicinity of the NP due to successful membrane wrapping. Loading of EGF onto the PEGs has a much weaker effect and only leads to an additional discernable spectral shift for the high EGF density case with 200 EGF/NP.

2.3 Cellular NP-EGF Distribution and Multivalent Enhancement of NP Binding.

We chose HeLa and MDA-MB-468 cancer cells to study NP-EGF-induced binding in this work as these cells represent well-characterized models for cells with physiological (HeLa) or highly increased (MDA-MB-468) EGFR expression levels. [92] As EGFR signaling is spatially regulated, EGFR phosphorylation at the plasma membrane can lead to different outcomes than cytoplasmic signaling associated with endosome containing phosphorylated EGFR (pEGFR). [93,94] Knowledge of the cellular distribution of NP-EGF activated EGFR is, thus, important to understand the underlying signaling processes. We imaged the cellular distribution of NP-EGF in MDA-MB-468 cells after incubating with a 30 pM solution of NP-EGF (100 EGF/NP) for t_{inc} = 15, 30, 60 min through combined focused ion beam milling and scanning electron microscopy (FIB-SEM, Figure 2.3A). Figure 2.3B shows an individual cell before milling and Figure 2.3C summarizes the resulting depth distribution profiles for the three investigated incubation times (t_{inc}). Representative SEM images after 5s and 45 s of ion milling for cells incubated with NP-EGF for t_{inc} = 15, 30, 60 min (top, middle, bottom) are summarized in Figure 2.3D. The depths profiles reveal that for t_{inc} = 15 min NP-EGF are primarily associated with the cell surface (68%) of the NP are within one particle diameter of the cell surface), but that with

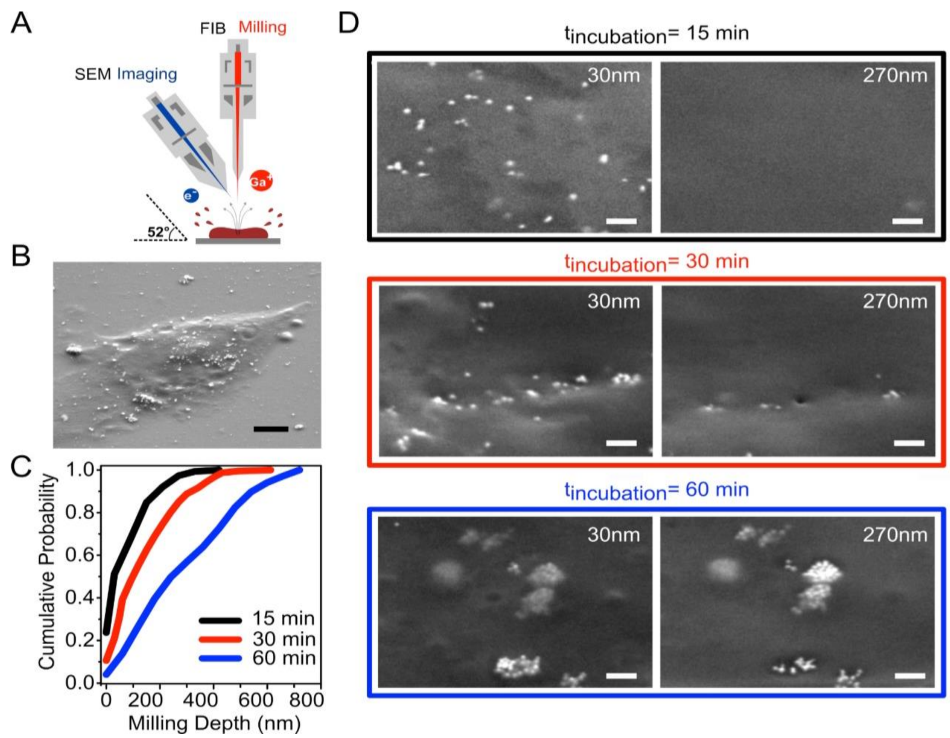

Figure 2.3 A. FIB-SEM was applied to mill MDA-MB-468 cells and to record SEM images at different depths. B. SEM image of an individual cell before milling. C. Cumulative depth distribution of NP-EGF after incubation times of t_{inc} = 15 min, 30 min, 60 min. D. SEM images of identical cellular regions for an exemplary cell recorded at milling depth of 30 nm (left) and 270 nm (right) for cells incubated with NP-EGF for t_{inc} = 15 min (top row), t_{inc} = 30 min (middle row), and t_{inc} = 60 min (bottom row). FIB milling was performed with a rate of approx. 6 nm/s, and the SEM images at depths of 30 nm and 270 nm were obtained after 5 s or 45 s of milling.

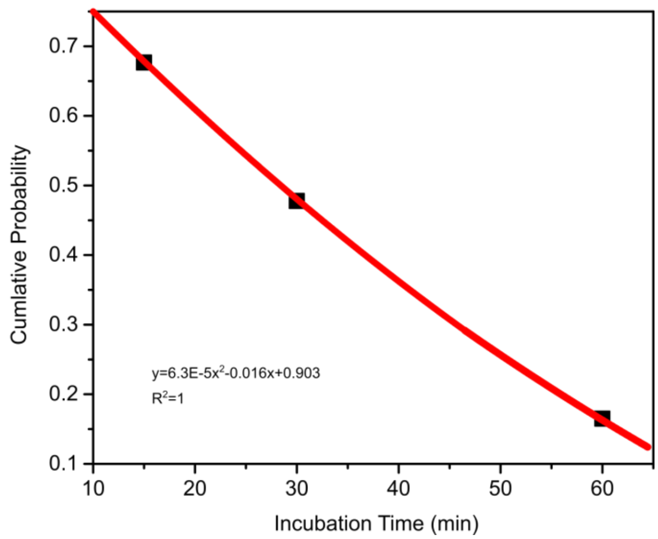

Figure 2.4 Cumulative probability to find a NP-EGF (200 EGF/NP) within 80 nm of the surface as function of the incubation time determined by FIB milling with subsequent SEM inspection. The black squares are experimental points, the red line is a fitted regression curve.

increasing time, the NP are uptaken and distributed throughout the cytoplasm. Since we focus in this work on plasma-membrane localized EGFR activation in living cells, we limited the incubation time with NP-EGF to 10 min and subsequently immediately fixed the cells to ensure that the overwhelming majority of the NP-EGF are bound but not yet internalized and that the measured phosphorylation is primarily associated with the plasma membrane. Based on the progression of the uptake established in Figure 2.3C, we project that at least 75% of NP-EGF are contained within 80 nm (~1 NP diameter) of the cell surface at t_{inc} = 10 min (Figure 2.4). Compared with alternative pharmaceutical approaches that block receptor internalization at physiological temperatures, the chosen approach of limiting the incubation time minimizes cellular stress and avoids

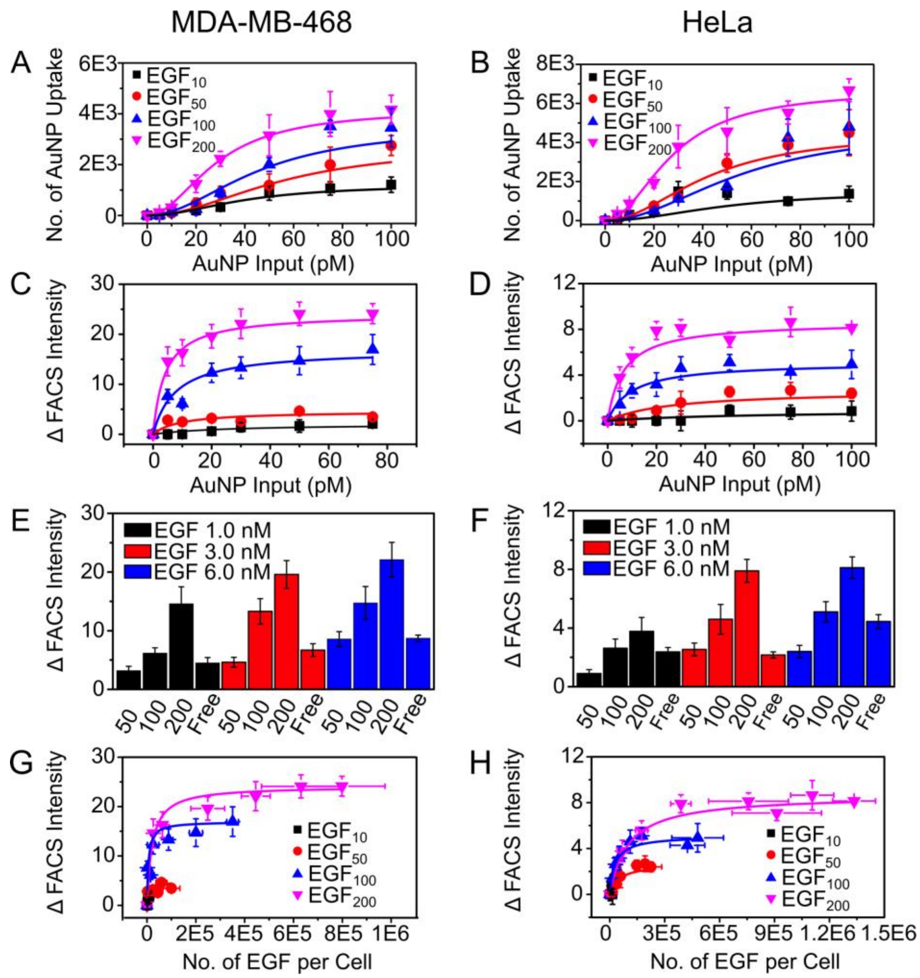

Figure 2.5 A. Number of NP-EGF per MDA-MB-468 cell, as determined by ICP-MS, as function of input concentration and EGF loading (10, 50, 100, 200 EGF/NP). The NP-EGF were incubated with cells at 37°C for 10 min. The average cell number per ICP-MS run was 20,000. B. Same data for HeLa. C., D. EGFR phosphorylation determined by flow cytometry as function of NP-EGF input for nanoconjugates with specified EGF loading for MDA-MB-468 and HeLa. The individual data points represent geometric means. The average number of cells per run was 10,000. E., F. Phosphorylation signal for NP-EGF with different EGF surface loadings (50, 100, 200 EGF/NP) and free EGF at effective EGF concentrations of 1.5, 3.0, 6.0 nM for MDA-MB-468 and HeLa. G., H. Phosphorylation signal as function of the number of EGF peptides delivered per cell for MDA-MB-468 and HeLa. The data presented in A-H are averages of eight independent experiments.

undesirable side effects.

Figure 2.5 A&B plots the number of NP-EGF per cell as function of NP input concentration [NP-EGF] for nanoconjugates as determined by inductively coupled mass spectroscopy (ICP-MS) with 10, 50, 100, or 200 EGF/NP for both HeLa and MDA-MB-468 cells after 10 min of incubation. For both MDA-MB-468 and HeLa the gold NP signal increases overall with input concentration and EGF loading, confirming a multivalent enhancement of NP-EGF binding. Control experiments with membrane wrapped NP without EGF confirmed that the NP binding was EGF-dependent (Figure 2.6).

2.4 Amplification of EGFR Phosphorylation through Multivalent EGF Presentation.

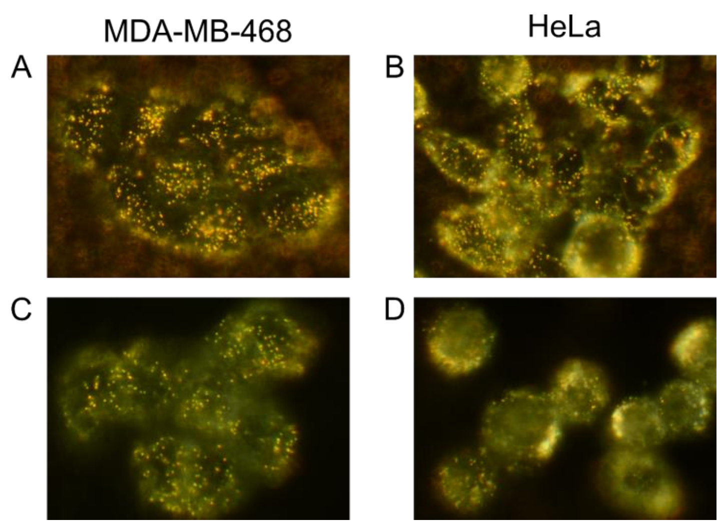

Figure 2.6 Dark-field images of MDA-MB-468 cells (A, C) and HeLa cell (B, D) after NP treatment. Cells were incubated with 30 pM of NP-EGF (200 EGF/NP) (A, B); or 30 pM of MWP (C, D) for 10 min.

NP-EGF binding induces EGFR phosphorylation, which can further spread through EGFR-EGFR-mediated transactivation. We quantified EGFR phosphorylation at Tyr1086 as function of EGF surface loading by immunolabeling and subsequent flow cytometry analysis for HeLa and MDA-MBA-468. The measured EGFR phosphorylation versus NP-EGF concentration plots show a logarithmic growth behavior for all EGF loadings (Figure 2.5C and D). Importantly, for both cell lines the efficacy (maximum phosphorylation) and potency (concentration corresponding to ½ of the maximum phosphorylation) of NP-EGF increases with increasing EGF loading. Consistent with the differences in receptor expression levels, the phosphorylation measured for EGFR-overexpressing MDA-MB-468 exceeds that of HeLa. To compare the phosphorylation obtained for NP-EGF with that of free EGF we calculated the effective EGF concentrations for the nanoconjugates by multiplying the EGF surface loading with the NP concentrations. In Figure 3E and F we compare the measured phosphorylation levels for NP-EGF with EGF loadings of 50 EGF/NP, 100 EGF/NP, or 200 EGF/NP at effective EGF concentrations of 1.5, 3.0, or 6.0 nM with each other as well as with free EGF of the same concentration. EGF loadings > 50 EGF/NP systematically yield a stronger phosphorylation levels than free EGF. The important role of the EGF density in determining cellular phosphorylation levels is evidenced by the observation that the differences in phosphorylation for NP-EGF with different EGF loading (differences within one color) are larger than those for NP-EGF with identical EGF loading but different effective EGF concentrations (differences between colors). It is interesting that NP-EGF with 50 EGF/NP show less phosphorylation than free EGF at the same effective EGF concentration despite the fact that even the initial NP-cell contact area (Figure 2.1D) contains more than one (~6) EGF to bind to EGFR on the cell side. The lower phosphorylation when compared with free ligand could result from a decrease in the binding affinity of the individual EGF after tethering to the PEG spacer[95] or from other perturbations that are associated with conjugation to NP (slower diffusion, steric hindrance, etc.) and that need to be compensated by a higher degree of multivalency.

Although the data in Figure 2.5E and F generally confirm a positive correlation between phosphorylation and EGF loading, one caveat in comparing phosphorylation levels of NP-EGF with different EGF loadings as function of NP-EGF input is that it does not provide sufficient information to differentiate between effects associated with an intrinsic gain in EGFR phosphorylation efficacy and binding affinity of the NP. Different EGF surface densities influence the binding (see Figure 2.5A and B) and, thus, the total number of delivered NP-EGF. [96-99] To eliminate trivial effects in phosphorylation that arise from differences in NP binding, we compared the phosphorylation obtained for NP-EGF with different EGF loadings at identical concentrations of delivered EGF. Figure 2.5G and H plots the phosphorylation as function of the number of delivered EGF for MDA-MB-468 and HeLa. This number was obtained by multiplying the number of delivered NP per cell determined by ICP-MS with the EGF surface loading determined by ELISA. The graph shows that NP-EGF with higher EGF loading deliver more EGF but that in the concentration ranges where NP-EGF with different EGF densities overlap, the nanoconjugates

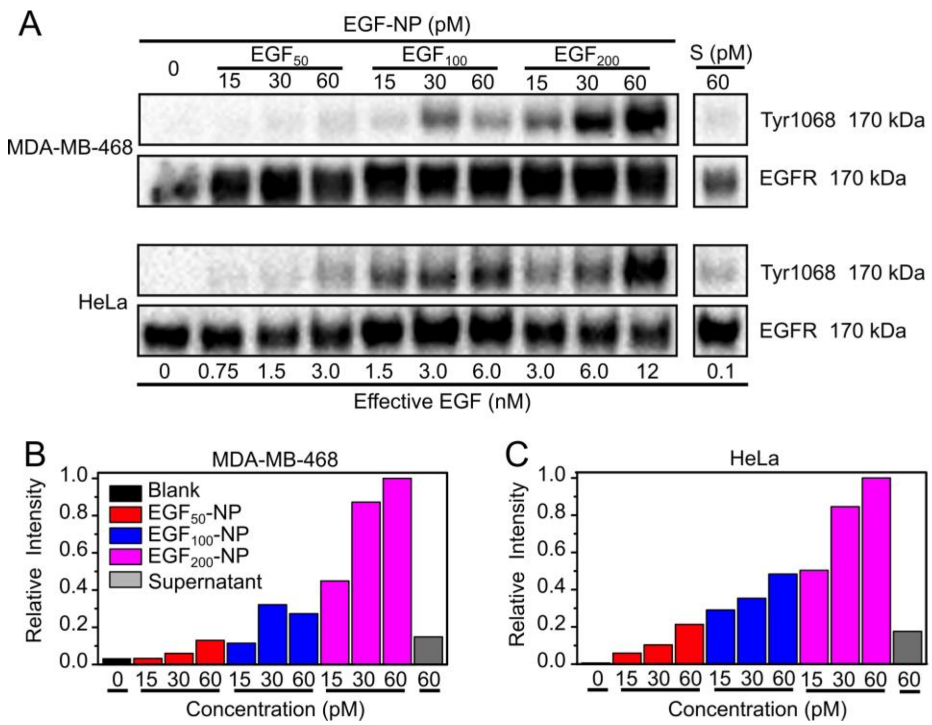

Figure 2.7 A. Immunoblots of pEGFR (Tyr 1068) and EGFR for (from left to right) blank; 15, 30, 60 pM of NP-EGF (50 EGF/NP); 15, 30, 60 pM of NP-EGF (100 EGF/NP); 15, 30, 60 pM of NP-EGF (200 EGF/NP); and supernatant of 60 pM of NP-EGF (200 EGF/NP) obtained with MDA-MB-468 (top) and HeLa (bottom). Cells were stimulated with NP-EGF and supernatant for 10 min. B. Relative phosphorylation for specified experimental conditions for MDA-MB-468. The phosphorylation was determined as ratio of pEGFR and EGFR signals. C. Same as in B. but for HeLa. The average number of cells per Western Blot was 20,000.

with higher EGF loading still achieve higher EGFR phosphorylation even though the number of delivered EGF is identical.

Intriguingly, NP-EGF with different EGF loadings do not converge against a common maximum phosphorylation level in the asymptotic limit (Figure 2.5G and H). Instead, the maximum phosphorylation increases with growing EGF loading in the sequence 10 EGF/NP < 50 EGF/NP < 100 EGF/NP < 200 EGF/NP. Different efficacies imply a non-linear amplification of EGFR phosphorylation with increasing EGF density and reveal that the effect of a lower EGF surface density on the maximum phosphorylation cannot be off-set by an increase in NP-EGF input. Multivalency is expected to increase the binding of EGF-functionalized NP, but a higher binding affinity alone cannot account for an increase of the maximum cellular phosphorylation. Instead, the increase of the asymptotic phosphorylation with growing ligand indicates a qualitatively different receptor activation mechanism in response to increasing EGF densities. We validated the phosphorylation trends by flow cytometry through independent quantitative Western Blots. Figure 2.7A contains immunoblot images of pEGFR and EGFR for MDA-MB-468 and HeLa, respectively, and Figure 2.7B and C summarizes the relative EGFR phosphorylation intensities normalized by the total EGFR protein concentration for the investigated NP-EGF conditions. The Western Blots show again an increase in EGFR phosphorylation as function of both EGF loading and NP input for

HeLa and MDA-MB-468. The phosphorylation obtained for the supernatant of 60 pM NP-EGF with 200 EGF/NP (included as control in Figure 2.7A) was low, confirming that the phosphorylation gains in Figure 2.7B and C were caused by NP-EGF, not residual free EGF.

2.5 Spatial Mapping of NP-EGF-Induced EGFR Phosphorylation.

The data in Figures 2.5 and 2.7 confirm a multivalent amplification of phosphorylation through NP-EGF with EGF loadings > 50 EGF/NP. To elucidate the spatial relationship between NP-EGF binding and EGFR phosphorylation and to account for differences in the asymptotic phosphorylation levels, we combined conventional confocal fluorescence microscopy of immunolabeled pEGFR and confocal backscattering microscopy of cell-bound NP. As benchmark we first imaged the spatial distribution of pEGFR in the dorsal plasma membrane after incubating cells with 3 nM free EGF for 10 min. The fluorescence induced by EGF is not homogenously distributed, instead the confocal scans show discrete "spots" of increased fluorescence intensity as illustrated in Figure 2.8A for MDA-MB-468. This pEGFR distribution is consistent with the activation of a heterogeneously distributed EGFR receptor that results in a spatial enrichment of EGFR in membrane domains. [28,33,100,101] An additional important baseline for evaluating the effect of EGF nanoconjugation and pEGFR distribution is the effect of residual free ligand in the washed NP-EGF preparations. The supernatant of a 30 pM NP-EGF preparation with

200 EGF/NP shows only a weak activation limited to specific spots (Figure 2.8B).

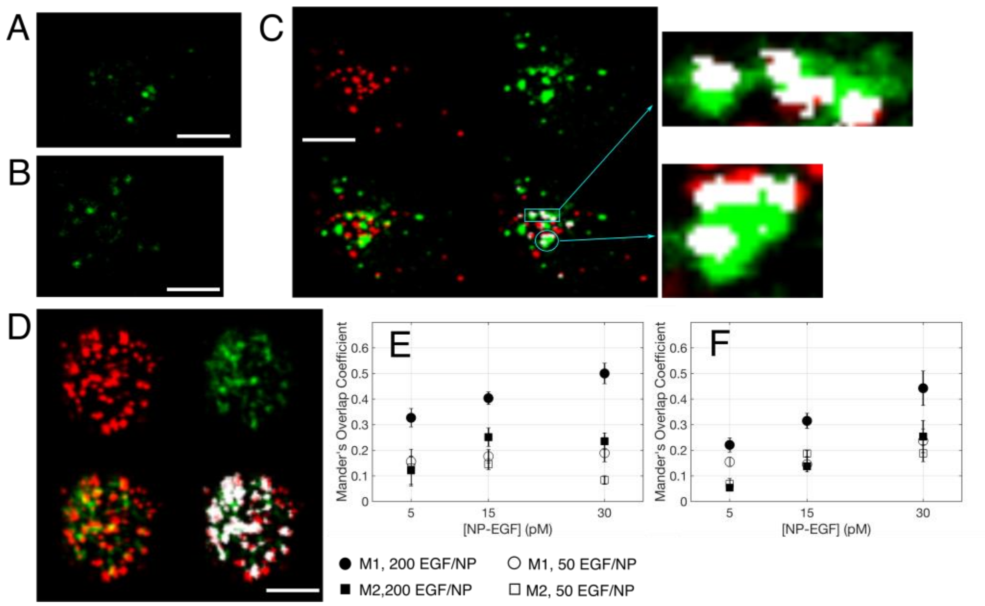

Figure 2.8 A. Confocal image of immunolabelled pEGFR in the dorsal plasma membrane of MDA-MB-468 treated with 3 nM EGF. B. Confocal map of immunolabelled pEGFR in the plasma membrane of MDA-MB-468 after treatment with the supernatant of 30 pM NP-EGF (200 EGF/NP). C. Top row: Confocal backscattering image of NP-EGF (15pM, 50 EGF/NP) bound to the plasma membrane of an MDA-MB-468 cell (left); confocal scan of the immunolabeled pEGFR in the membrane (right). Bottom Row: merged image (left); computed colocalized pixel map (right). The effective EGF concentration is 0.75 nM. D. Same as in C. but with an EGF loading of 200 NP/EGF, corresponding to an effective EGF concentration of 3 nM. E. Mander's Overlap Coefficients M1 and M2 for NP-EGF with 200 EGF/NP and 50 EGF/NP in MDA-MB-468 for three input concentrations: 5 pM, 15 pM, 30 pM. F. Same as in E. but for HeLa. Size bars are 10 μm. Data presented in E and F were collected from ten cells.

In the next step, we mapped the spatial distribution of pEGFR induced by NP-EGF with high (200 EGF/NP) and low (50 EGF/NP) ligand density. We incubated the cells again with NP-EGF at concentrations of 5, 15, 30 pM for 10 min. Figure 2.8C and D shows confocal scans obtained with MDA-MB-468 cells after treatment with a 15 pM solution of NP-EGF and surface loadings of 50 and 200 EGF/NP, respectively. The individual panels contain the backscattering scan that maps the NP-EGF distribution, the fluorescence scan that maps the pEGFR distribution, a merger of the latter two, and a computed map highlighting pixels that contain intensities on both channels. To quantitatively characterize the spatial relationship between NP-EGF binding and EGFR phosphorylation, we calculated Manders Overlap Coefficients (MOC). [102] The latter measures the fraction of pixels that have a detectable signal intensity in both monitored signal channels, independent of the magnitude of the signal. [103] We chose the MOC approach to evaluate the spatial overlap between NP and pEGFR signal as the intensities of these two species can vary significantly considering that different signals are detected (resonant backscattering versus fluorescence). A MOC value of 1 corresponds to perfect colocalization, whereas a value of 0 indicates absence of colocalization. M1 quantifies the overlap of backscattering signal with fluorescence and M2 the overlap between fluorescence and backscattering. The calculated M1, M2 values for all experimental conditions in MDA-MB-468 are summarized in Figure 2.8E. For 200 EGF/NP, M1 is systematically higher than M2 for all NP-EGF input concentrations. The M1 values increase with NP-EGF input and lie in the range 0.32±0.04 to 0.50±0.04. The maximum M1 colocalization value is consistent with a NP-EGF-induced phosphorylation but also shows that not all NP-EGF binding events are successful in inducing a measurable phosphorylation signal, presumably due to existing cellular inactivation mechanisms. [104, 105] Furthermore, not all backscattering signals are caused by NP-EGF as larger cellular structures can also contribute to the detected scattering signal so that a perfect colocalization is not expected. Importantly, the M2 values remain below 0.26±0.03 for all NP-EGF concentrations. In the case of 50 EGF/NP, both M1 and M2 remain < 0.20 due to an overall weak NP-induced EGFR phosphorylation. We performed an identical set of imaging experiments with HeLa cells and the resulting M1 and M2 values are summarized in Figure 2.8F. The MOC values show the same trends as observed for MDA-MB-468, but the M1 values for 200 EGF/NP lie lower (between 0.22±0.03 and 0.44±0.07) than for the EGFR overexpressing MDA-MB-468.

The systematic difference between M1 and M2 for NP-EGF with high ligand loading in Figure 2.8E and F is intriguing. Increased M1 values paired with low M2 values indicate that NP-EGF containing regions show significant pEGFR phosphorylation, but that the pEGFR signal also exists in areas void of NP-EGF. Part of this non-colocalizing fluorescence intensity can be attributed to background phosphorylation as observed in Figure 2.8B. However, it is noteworthy that NP-EGF binding often induces EGFR phosphorylation in direct vicinity of the NP, resulting in NP-EGF being embedded in larger pEGFR-positive regions, as shown in the magnified cell sections in Figure 2.8C. This behavior is characteristic of a lateral

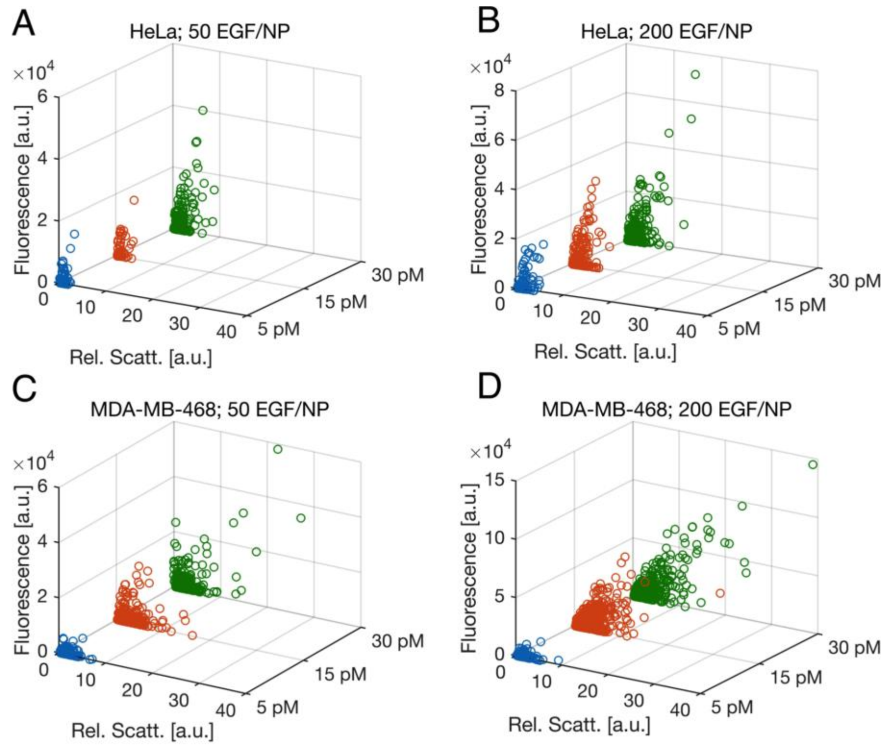

E **Pearson Correlation Coefficients (PCC)**

HeLa	**50 EGF/NP**		**200 EGF/NP**	
concentration	PCC	p-value	PCC	p-value
5 pM	0.47	<0.0001	0.48	<0.0001
15 pM	0.39	0.008	0.47	<0.0001
30 pM	0.58	<0.0001	0.67	<0.0001

MDA-MB-468	**50 EGF/NP**		**200 EGF/NP**	
concentration	PCC	p-value	PCC	p-value
5 pM	0.18	0.10	0.28	0.0014
15 pM	0.20	0.0004	0.67	<0.0001
30 pM	0.62	<0.0001	0.83	<0.0001

Figure 2.9 Local pEGFR fluorescence intensity versus relative NP backscattering signal (normalized by monomer intensity) for A. HeLa with 50EGF/NP; B. HeLa with 200 EGF/NP; C. MDA-MB-468 with 50 EGF/NP; D. MDA-MB-468 with 200 EGF/NP. Three different NP-EGF concentration were used 5 pM (blue), 15 pM (red), 30 pM (green). The scattering intensity is normalized by average scattering intensity of an individual NP. E. The table summarizes the calculated Pearson Correlation Coefficients (PCC) for fluorescence intensity and scattering signal and associated Student's t-test p-values for the individual conditions. The data in A-D were collected from ten cells per condition.

from previous studies that reported a rapid and extensive propagation of receptor phosphorylation over entire cell after local activation with EGF-functionalized multivalent beads or microfluidic flow,[30,31] the spread induced by the smaller NP-EGF observed in this work is not global but more limited to the region around the NP. Intriguingly, this spread occurs in cells with high (MDA-MB-468) or physiological (HeLa) receptor expression levels, provided the EGF loading of the NP are sufficiently high. We attribute this behavior to the heterogeneous spatial distribution of EGFR, which generates sufficiently high regional EGFR densities in the plasma membrane to facilitate a spatially limited lateral phosphorylation transfer in both HeLa and MDA-MB-468 cells.

2.6 NP-EGF Clustering and EGFR Phosphorylation

Indications of Signaling "Hot Spots: Scanning electron microscopy images of NP-EGF-treated cells show a significant clustering of the NP on the cell

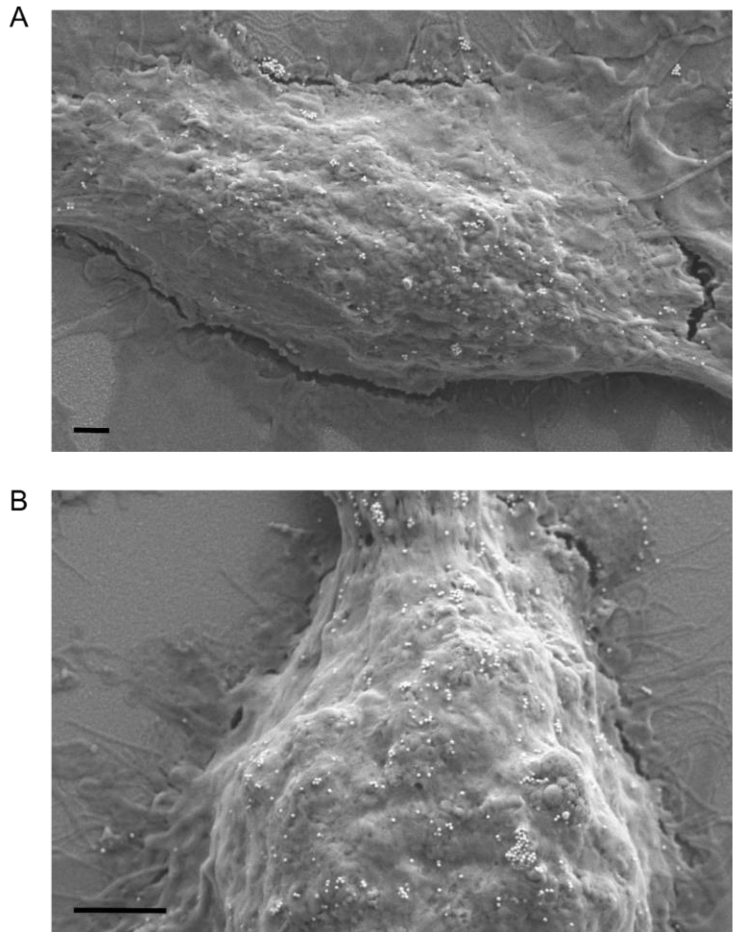

Figure 2.10 SEM images of NP-EGF on the membrane of fixed MDA-MB-468. Cells were plated in a 1 cm×1 cm silicon chip and stimulated with 30 pM of NP-EGF (100 EGF/NP) for 10 min. The working distance is 8.7 mm and electron high tension value is 3.00 kV. Clustering of NP-EGF is clearly discernable across the cell surface. Size bar = 1μM (A); Size bar = 2μM (B).

surface (Figure 2.10). To quantify the relationship between NP-EGF concentration and EGFR phosphorylation at the location of NP-EGF binding, we integrated the pEGFR fluorescence signal over the area defined by surface-bound NP-EGF and quantified the resulting fluorescence as function of NP intensity. We normalized the backscattering signal of the NP by dividing through the average intensity of an individual NP. Although electromagnetic coupling between NP (vide infra) affects signal intensities, [59] the normalized confocal backscattering intensities give an acceptable first estimate for the number of NP per investigated spot. Figure 2.9A-D summarizes the measured pEGFR fluorescence as function of normalized NP intensity for different input concentrations of NP-EGF with ligand densities of 50 EGF/NP or 200 EGF/NP for HeLa (A, B) and MDA-MB-468 (C, D). The associated Pearson correlation coefficients (PCC) for the relationship between fluorescence and backscattering intensities and their statistical p-values (two-sided Student t-test) are included in Figure 2.9E. The local NP scattering signal, or NP clustering, in Figure 2.9A-D increases with NP-EGF input and EGF loading and is in general higher for MDA-MB-468 than for HeLa. The average number of NP-EGF contained per diffraction-limited spot for the measured distributions are summarized in Table. At conditions that favor NP-EGF clustering on the cell surface, i.e. high NP-EGF input concentrations (30 pM) and high ligand densities (200

Table 1: Average confocal backscattering signal for NP-EGF bound to HeLa or MDA-MB-468 as function of EGF loading of the NP and input concentration.

EGF Loading	Conc.	HeLa		MDA-MB-468	
		Backscattering Average	STD	Backscattering Average	STD
50 EGF/NP	5 pM	0.96	0.04	1.49	0.08
	15 pM	1.04	0.07	2.35	0.10
	30 pM	1.51	0.07	2.41	0.14
200 EGF/NP	5 pM	1.80	0.09	1.53	0.07
	15 pM	1.90	0.08	2.82	0.10
	30 pM	2.21	0.11	2.92	0.14

EGF/NP), a strong positive correlation between pEGFR signal, measured as fluorescence intensity, and NP-EGF signal is observed. The peak NP and fluorescence intensities as well as the correlation are higher for the EGFR over-expressing MDA-MB-468 (PCC = 0.82) than for HeLa (PCC = 0.67). For the low EGF density case, NP-EGF clustering at high NP-EGF input concentration still achieves a moderate positive correlation between local fluorescence intensity and NP-EGF signal with PCC = 0.62 (MDA-MB-468), PCC= 058 (HeLa).

The findings that NP-EGF clustering increases with input concentration and EGF loading and that this gain in clustering is associated with a gain in EGFR phosphorylation has important implications for the interpretation of the global increase in EGFR phosphorylation as function of EGF loading and concentration in Figures 2.5 and 2.7. The data in Figure 6 reveal that the

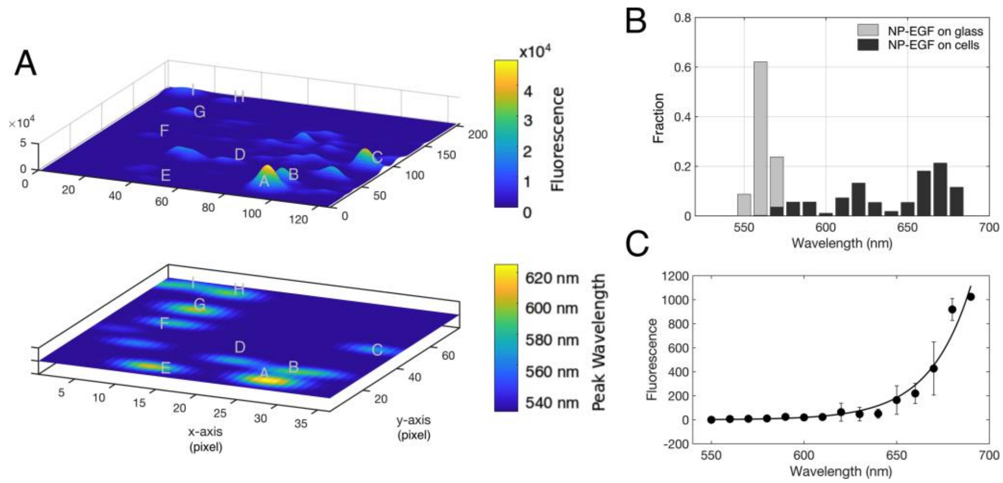

Figure 2.11 A. Confocal map of pEGFR fluorescence (top) and map of peak LSPR wavelength of the same field of view obtained with hyperspectral darkfield imaging (bottom) in a single HeLa cell. NP-EGF with 200 EGF/NP and a concentration of 15 pM were used. The individual pixels are color-coded to identify their peak resonance wavelength in the spectral range 530 nm – 700 nm. Markings a-i indicate positions of colocalizing intensities in both channels. B. Histogram of the peak wavelength of cell-bound NP-EGF and NP-EGF bound to glass. C. pEGFR fluorescence as function of peak LSPR wavelength obtained from eight individual HeLa cells.

increase in cellular phosphorylation is not simply a result of more randomly distributed NP-EGF binding with identical phosphorylation response. Instead, the total signal is enhanced by formation of NP-EGF clusters that provide stronger EGFR phosphorylation.

The confocal analysis is limited in resolution by the wave nature of light. To identify the length scale of NP-EGF clustering that is relevant for the phosphorylation enhancement, we next characterized the fluorescence signal as function of the plasmon resonance wavelength of the NP, which encodes information about NP separations on the nanometer to tens of nanometer length scale. To that end, we collected confocal fluorescence scans of fluorescently labeled pEGFR and darkfield scattering spectra maps of NP-EGF (200 EGF/NP) of the same field of view collected in a wide-field microscope. Figure 2.11A contains an example with the fluorescence scan on the top and a map of the fitted peak wavelength on the bottom. We point out that the differences in the ranges of the x,y-axes derive from the different pixelations of the used detectors. It is clear from the detected peak wavelengths that the plasmon resonances of NP-EGF bound to the cell surface are strongly red-shifted when compared with the same particles deposited on glass (Figure 2.11B). As glass has a similar refractive index (RI = 1.52) as the cell surface, we attribute these large spectral shifts to a strong electromagnetic coupling between closely spaced NP. This finding is entirely consistent with findings from Abulrob *et al*. and others who have shown that EGFR in the plasma membrane of HeLa cells is locally enriched in surface compartments with typical dimensions on the order of 150 nm. [51] Binding of multiple NP to domains of this size would result in a crowding of NP and facilitate plasmon hybridization. [106] The magnitude of the spectral shift of these clusters increases with growing number of coupling NP and decreasing interparticle separation. [59]

The positive correlation between LSPR wavelength and co-localized pEGFR signal intensity in Figure 2.11C confirms that NP-EGF association on deeply subdiffraction limit length scales is a key driver for NP-EGF-clustering-amplified EGFR phosphorylation. Importantly, the increase in phosphorylation as function of resonance wavelength is non-linear but becomes stronger with longer wavelength. Large NP clusters with short interparticle separations that achieve a strong shift of the plasmon resonance are most efficient in boosting EGFR phosphorylation.

Overall our analysis of Figures 2.9 and 2.11 confirms increasing levels of local phosphorylation due to spatial NP-EGF clustering. The strong increase in local phosphorylation associated with clustering accounts naturally for the differences in maximum phosphorylation observed for different EGF loading ratios in Figure 2.5G and H. Our data reveal that NP-EGF clustering induces the formation of sub-diffraction limit phosphorylation "hot-spots" which can enhance the phosphorylation response on a cellular level. As NP-EGF clustering increases with ligand loading (Figure 2.9, Table 1),[39,43] one must conclude the local signal enhancement through NP-EGF clustering is an intrinsic component of signal amplification through multivalent NP for a heterogeneously distributed receptor.

2.7 Conclusion

We have investigated the global cellular EGFR phosphorylation intensity and its spatial distribution in HeLa and MDA-MB-468 cells as function of both NP-EGF input concentration and EGF loading in the range of 10 – 200 EGF/NP. On the cellular level the EGFR phosphorylation generally increases with NP-EGF input. Intriguingly, the maximum phosphorylation depends on the multivalency of the NP and increases with EGF loading. This behavior is insufficiently explained by a multivalent amplification of binding affinity alone and, instead, indicates a qualitative change in the receptor activation associated with increasing ligand loading of the NP. A quantitative analysis of the spatial correlation between local NP-EGF binding and EGFR phosphorylation reveals that NP-EGF-induced EGFR phosphorylation depends on the spatial distribution of the nanoconjugated EGF and that NP-EGF clustering is an important parameter that influences maximum cellular phosphorylation levels. NP-EGF clusters induce locations of increased EGFR phosphorylation, and the intensity of these signaling “hot spots” increases with local NP-EGF concentration and EGF loading. The formation of clusters of nearly touching NP is particularly efficient for EGFR activation. EGFR phosphorylation is, however, not restricted to locations containing bound NP-EGF. We reconcile the increase in NP-EGF dependent phosphorylation detected by flow cytometry and Western Blotting with M2 values that are consistently lower than M1 through an NP-EGF-independent spread of EGFR phosphorylation, similar to what was observed before for EGF-loaded beads.[31,32] For NP-EGF this spread is not global but spatially confined to the vicinity of the NP, and both the EGFR overexpressor MDA-MB-468 as well as HeLa with physiological EGFR expression level show this regional spread of phosphorylation. We conclude that – despite a large difference in formal expression level – in both cell lines membrane domains exist in which the heterogeneously distributed receptor is sufficiently high concentrated to facilitate a lateral trans-phosphorylation. As the initial pEGFR signal at the site of the NP contact is positively correlated with NP-EGF clustering and the latter increases with ligand loading of the NP, the findings of this study demonstrate that the accumulation of EGF-EGFR contacts through spatial NP-EGF clusters is an intrinsic component of the amplification of EGFR activation through multivalent NP-EGF. The local density of formed EGF-EGFR contacts depends both on the clustering of NP-EGF in the membrane as well as the EGF loading of the individual NP. Our combined biochemical and imaging studies show that an increase in EGF-EGFR density due to clustering of multivalent NP-EGF is associated with an EGF-loading-dependent increase in the maximum EGFR phosphorylation level. This functional dependence can be attributed to the facts that a local enrichment of receptors favors interactions between activated and non-activated receptors, shifts equilibria towards oligomerization, and facilitates ligand-independent lateral spread of receptor activation. Receptor clustering also alleviates ligand rebinding [107.108]and is crucial for some second messenger driven phosphorylation [109,110] after an initial activation. All of these effects can in principle account for the increase of the EGF-loading-dependent asymptotic EGFR phosphorylation level, but the relative contributions from the individual effects remain to be quantified. Naturally, the degree of clustering of a multivalent NP on the cell surface depends not only on the NP concentration and its ligand density but also on the spatial distribution of the receptors in the membrane. Since the latter may vary between individual cells and cell lines, the spatial distribution of the receptor could result in different signaling in response to NP-EGF and, thus, provide opportunities for controlling cellular behavior with NP. In closing, we would like to note that our finding that a multivalent presentation of EGF on NP does not only enhance the binding affinity of the NP but also strengthens signaling-relevant proximity effects in EGFR clusters has mechanistic implications also for other RTK and potentially a broader range of transmembrane receptors. Our study underlines the importance of the spatial organization of receptors and ligands for key steps in signaling initiation. Conceptualized in a broader context our findings suggest that the nanoscale spatial distribution of ligands in the extracellular matrix or during cell-cell contacts can influence signaling outcomes and could, thus, be an important factor for regulating cell development and differentiation.

2.8 Materials and Methods

Colloidal Au NP Synthesis. Colloidal gold seeds were prepared by heating 20 mL of $HAuCl_4 \cdot 3H_2O$ (0.26 mM, Sigma-Aldrich, wt 393.83 g), and adding 800 μL of sodium citrate dihydrate (34.00 mM, Sigma-Aldrich, wt 294.10 g) immediately after boiling. The gold seeds were then grown to an average size of 80 nm by adding dropwise 80 mL of $HAuCl_4.3H_2O$ solution (1.00 mM), and 80 mL of a mixture of sodium citrate dihydrate (0.85 mM) and L-Ascorbic acid (2.84 mM, Sigma-Aldrich, wt 176.12 g). The gold solution was then boiled for 30 min and neutralized to pH 7 with a 10 mM aqueous solution of NaOH (Sigma-Aldrich, wt 40.00 g). Before use, the colloidal gold solution was washed by centrifugation (720g, 10 min) and resuspension in Milli-Q water.

Membrane wrapping of Au NP. A total amount of 2 μmole of lipid mixture (Avanti Polar Lipids) was prepared by mixing DPPC (10 mM), cholesterol (10 mM), DSPE-PEG (2000) azide (3 mM), and DOPS (5 mM) in a clean 25 mL round-bottom flask. The solvent chloroform in the lipid mixture was removed by rotary evaporator. A uniformly thin lipid layer formed on the bottom of the flask, which was then further dried under vacuum overnight. HEPES buffer (20 mM, Sigma-Aldrich, wt 238.30 g) was added to the dried lipid layer (1 mL 10 mM HEPES buffer per 1 μmole lipid), and the mixture was sonicated for 5 min to form a clear liposome solution. For each 500 μL of liposome solution, 50 μL of Au NP pellet (2×10^{11} particles/mL) was added. Subsequently, 40 μL of 1-Octadecanethiol (8.72 mM, Sigma-Aldrich, wt 286.56 g) dissolved in ethanol was added. The final volume was brought to 1 mL with HEPES buffer. The mixed solution was then shaken for 5 h, 18 h or 24 h, respectively. The NP were subsequently washed three times through centrifugation (720g, 10 min) and re-suspended in HEPES buffer.

NP-EGF Preparation. EGF Recombinant Human Protein (ThermoFisher, 1mg/mL, 1X PBS) was functionalized by adding 2% v/v of Propargyl-N-hydroxysuccinimidyl ester (Sigma-Aldrich, 0.44 M in DMSO, wt 225.20 g) and incubated on ice for 6 h. The functionalized EGF was then dialyzed in 1x PBS via D-Tube Dialyzers (Millipore) overnight to remove excessive NHS ester. The conjugation was completed by mixing 5 μL of functionalized EGF with membrane-wrapped NP (NP: EGF, 1:50000). The catalyst was prepared by mixing a 0.10 M solution of L-Ascorbic acid with a 5.10 mM

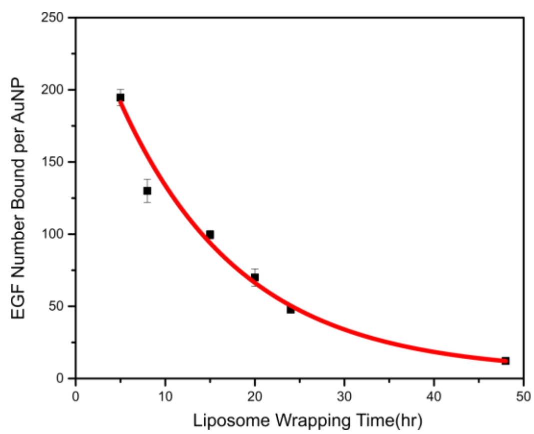

Figure 2.12 Number of EGF bound per NP (determined by ELISA) for membrane wrapped NP generated by incubating with liposomes (see Methods in the main text) for different incubation times. With increasing incubation times the sterically demanding DSPE-PEG (2000) azide lipids are exchanged with smaller lipids in the liposomes to maximize the intermolecular interactions in the self-assembled membrane. The thermodynamic optimization of the membrane reduces the number of available EGF cross-linking sites.

solution of $CuSO_4 \cdot 5H_2O$ (1:1 v/v). And 3 μL of catalyst was added to the mixture of alkyne-functionalized EGF and azide-presenting NP. The final volume of the mixture was brought to 100 μL with 0.1x PBS. To generate NP-EGF with different EGF loading, membrane-wrapped NP with different wrapping times were used (Figure 2.12). The crosslinking reaction was maintained at room temperature overnight. Subsequently, excessive EGF and catalyst were removed by dialysis with Nuclepore Track-Etched Membranes (Whatman, Pore Size 0.03 μm, Diameter 25 mm) in 0.1x PBS overnight.

Nanoparticle Characterization. The hydrodynamic radius and zeta potential of nanoparticles were measured by Zetasizer Nano ZS90 (Malvern, Worestershire, UK). The sample for size measurement contained 1×10^{11} particles/ mL in Milli-Q water. The sample concentration for zeta potential measurement was 1×10^{7} particles/ mL in 10mM NaCl (pH 7.0). The absorption spectra of particle solutions (1×10^{11} particles/ mL) were acquired on an Agilent Cary 5000 UV/vis spectrometer. Milli-Q water was

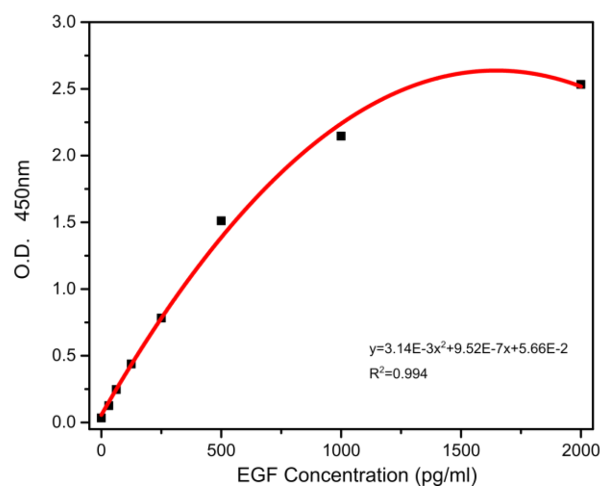

Figure 2.13 Human EGF ELISA kit calibration curve.

used for baseline correction. All spectra were normalized by dividing through the peak intensities. The number of EGF conjugated to NP was quantified with the EGF Human ELISA Kit (ThermoFisher) (Figure 2.12).

Cell Culture. The MDA-MB-468 cell lines was purchased from ATCC® (HTB-132TM). The HeLa cell line was a gift from Sam Thiagalingam at Boston University. The cells were cultured in advanced Dulbecco's modified Eagle medium (DMEM) supplemented with 10% fetal bovine serum, 2 mM L-glutamine, 50 units/mL penicillin, and grown in an incubator at 37 °C, 5% CO2 and 95% relative humidity. The cell seeding density was 1×105 cells/ mL, and experiments were conducted when the cells reached 80% confluency. HeLa cells were starved in serum-free DMEM/F-12 medium for 24 h before use. EGFR-overexpressing MDA-MB-468 cells were starved in serum-free DMEM/F-12 medium containing 20 mM of the anti-oxidant N-acetylcysteine (NAC) for 24 h before use.

Flow Cytometry Quantification of EGFR Phosphorylation. Cells were plated in 12-well dishes as described above. The cells were stimulated with a fresh medium containing NP-EGF or EGF at different concentrations for 10 min. Then, the medium was removed, and cells were washed with HBSS buffer. The cells were detached with StemProTM AccutaseTM Cell Dissociation Reagent (ThermoFisher) for 10 min at 37 °C, and collected by centrifugation (300 g, 5 min). The cells were fixed with 4% (w/v) PierceTM formaldehye (ThermoFisher) for 15 min, and permeabilized with 0.1% (w/v) TritonTM X-100 for 10 min. The cells were then incubated with

Phospho-EGFR (Tyr1086) antibody (0.5 μg/mL, ThermoFisher) for overnight at 4 °C. Subsequently, the cells were stained with an Alexa Fluor 647 conjugated secondary antibody (4 μg/mL, ThermoFisher) for 1 h at room temperature. The cells were washed three times with DPBS after each step of the fixation and labeling procedure to remove excess reagents. The fluorescence intensity distribution for each sample was measured with a BD LSRII flow cytometer and analyzed through Flowing Software 2. All fluorescence intensities are background corrected (intensity of cell control without treatment are subtracted) and the calculated difference is reported as FACS intensity.

ICP-MS Quantification of NP-EGF Binding. NP-EGF were prepared and bound to cells as described above. The number of cells in a sample were determined by a cell counter. A solution (30 μL) of cells was dissolved with 800 μL of aqua regia. The mixture was then dried overnight at 55 °C and re-dissolved in 1 mL of HCl solution (2% v/v). Subsequently, the samples were diluted 10x with HCl solution, and the gold concentration in the samples were quantified with a Thermo (VG) PlasmaQuad (PQ) ExCell inductively coupled plasma mass spectrometer.

Confocal Imaging. Cells were plated in 50 mm glass bottom dishes with a gridded glass inset (MatTek, gridded 1.5 coverslips). The gridded coverslips have an alphanumeric pattern, and offer imaging of cells and the grid in the same focal plane. The cells were stimulated with a fresh medium containing NP-EGF or free EGF at different concentrations for 10 min. Then, the medium was removed, and cells were washed with HBSS buffer. The cells were fixed with 4% (w/v) PierceTM Formaldehye (ThermoFisher) for 15 min. Then, cells were permeabilized with 0.1% (w/v) TritonTM X-100 for 10 min. Subsequently, the cells were incubated with Phospho-EGFR (Tyr1086) antibody (0.25 μg/mL, ThermoFisher) for overnight at 4 °C. Subsequently, the cells were stained with an Alexa Fluor 647 functionalized conjugated antibody (2 μg/mL, ThermoFisher) for 1h at room temperature. The cells were washed three times with DPBS after each step of the fixation and labeling procedure to remove excess reagents. Samples were imaged with scanning confocal microscope (Olympus FV 1000) at 543 and 633 nm. The backscattering signals were obtained using the 543 nm excitation line.

Dark-Field Microscopy. The cells were imaged in an inverted microscope (Olympus IX71) under dark-field illumination through a high numerical aperture (NA) oil condenser (NA= 1.2-1.4). The scattering light was collected through a 60x oil objective (NA = 0.65) and captured on an electron multiplying CCD (EMCCD, Andor Ixon+). The exposure time for each monochromatic image was 0.05 s, and the cycle time for a full set of ten images was 0.5 s. Digital color images were recorded under white-light illumination using an Olympus SP310 digital camera attached to the microscope through an eyepiece adapter.

Image Processing and Analysis. Confocal backscattering and fluorescence images were analyzed by ImageJ. [111] The Costes90 auto threshold algorithm was applied to background corrected images before MOC80 were calculated using algorithms implemented in the software. To correlate fluorescence and backscattering images, the particle finder routine was applied to localize discrete regions of interest. For these regions the intensities on the fluorescence and backscattering intensities were obtained by multiplying the average intensity with the size of the regions.

Focused Ion Beam (FIB) Sample Preparation. Cells were plated in a 1 cm ×1 cm silicon chip and treated with 50 pM of NP-EGF in fresh DMEM/F-12. Then, the medium was removed, and cells were washed with HBSS buffer. The cells were fixed with 0.4% paraformaldehyde and 1% glutaradehyde in 0.1 M sodium cacodylate buffer (pH 7.2) for 2.5 h at room temperature. After washing three times in 0.1M sodium cacodylate buffer for 10 min each time, the cells were post-fixed with 2% osmium tetroxide in distilled water for 30 min at room temperature. And cells were washed three times in Milli-Q water for 10 min each. The cells were then dehydrated by incubation in a series of solutions with ascending ethanol concentration (50%, 70%, 95%, 100%) for 15 min each and followed by three washing steps in 100% ethanol for 15 min each. Specimens were then washed three times in 100% acetone for 15 min each. Subsequently, samples were dried with Hexamethyldishilazane (HMDS) and acetone (1:1, v/v) for 10 min at room temperature, followed by overnight incubation in 100% HMDS. Samples were imaged using a Zeiss Supra40VP SEM at 10.0 kV and a working distance of 10 mm. The samples were subsequently milled and imaged with FEI Quanta 3D FIB instrument. The milling was done with 30 kV, 0.5 nA Gallium ion beam with 10-s intervals.

Western Blot. Cells were plated in 12-well dishes as described above. The cells were stimulated with a fresh medium containing NP-EGF or supernatant at different concentrations for 10 min. Then, the medium was removed, and cells were washed with HBSS buffer. Cells were harvested in lysis buffer (Cell Extraction Buffer, 1mM PMSF, 10% (v/v) protease inhibitor cocktail, ThermoFisher) on ice for 30 min. Unlysed cell fragments were removed by centrifugation at 13000 rpm for 5 min at 4 °C. Protein samples were separated by SDS-PAGE using NuPAGE 3-8% Tris-Acetate Protein Gels (Bio-Rad) and transferred to a polyvinylidene difluoride (PVDF) membrane (Bio-Rad). After transfer, the membrane was blocked with 5% milk in TBST for 30 min at 25 °C. The membrane was washed with TBST and immunoblotting was performed the following with the primary and secondary antibodies at the indicated dilutions in TBST: phosphor-EGFR (Tyr1068) antibody (Cell Singling Technology, #2234; 1:1000) at 4 °C overnight; EGF Receptor Antibody (Cell Singling Technology, #2232; 1:1000) at 4 °C overnight, and goat anti-rabbit IgG-HRP (Jackson

ImmunoResearch, 111-035-144; 1:5000) for 1 h at 25 °C. Blot imaging was developed with the ChemiDoc XRS+ system (Bio-Rad). The intensity of chemiluminescent image was quantified by ImageJ.

Chapter 3 Characterizing Nanoplastics-Induced Stress and Its Metabolomic SERS Fingerprint in an Intestinal Membrane Model

The accumulation of plastic waste in marine ecosystems results in a continuous release of nanoscale plastic particles into the environment through weathering processes. Nanoplastics ingested by animal or humans *via* food and water reaches the small intestine where interactions between non-biodegradable nanoparticles (NPs) and intestinal epithelial cells can potentially perturb the protective function of the intestinal membrane. In this work, we investigate the effect of 50 nm diameter polystyrene (PS) NPs functionalized with amine or carboxylic acid groups on a Caco-2 intestinal membrane model. Reactive oxygen species (ROS) generation, cell viability, and intestinal membrane integrity measurements were performed to detect and quantify PS NP-induced membrane damage under acute exposure conditions of 1×10^{12} – 1×10^{14} PS NPs / mL for 6 h and 18 h. The measurements reveal that both amine and carboxylic acid functionalized PS NPs induce cellular stress and perturb the membrane integrity, but that the amine functionalized NPs induce measurable effects at lower concentrations than their carboxylic acid functionalized counterparts. Surface Enhanced Raman Spectroscopy (SERS) was applied to monitor the composition of the medium in direct contact with the intestinal cells and to detect potential PS NP induced changes in the cellular metabolism in real time and in a minimally invasive fashion. The analysis of the SERS spectra through artificial intelligence algorithms and chemometric tools reveals concentration-, exposure time-, and surface chemistry-dependent differences in the cellular metabolism in response to PS NPs. The SERS spectral analysis identifies increased hypoxanthine ($C_4H_4N_4O$) levels as a spectroscopic marker for the PS NP-induced loss in membrane integrity

3.1 Introduction

Plastics is a collective term used for different classes of synthetic polymers that due to their favorable material properties have pervaded all aspects of human life. The annual production of plastics has continuously grown over the last 70 years, reaching a total output of 359 million metric tons in 2018.[113]One inevitable consequence of the anthropogenic use of plastics is its widespread accumulation in the environment. Common synthetic plastics used in packaging and consumer products include polyethylene (PE), polypropylene (PP), polystyrene (PS), polyvinyl chloride (PVC), and polyethylene terephthalate (PET), all of which are not biodegradable. When exposed to the elements, macroscopic objects from these plastics undergo photo-degradation as well as thermo-oxidative and mechanical degradation and gradually fragment into smaller and smaller pieces.[114] Synthetic polymer fragments with dimensions smaller than 5 mm are collectively referred to as microplastics, independent of their exact chemical composition.[115,116] Microplastics has become ubiquitous in aquatic ecosystems with concentrations of about 3 – 60 particles/m^3 in sea water, raising concerns about an accumulation of microplastics in the food chain.[116-118]

The weathering of plastics does not stop with micrometer-sized particles but continues on sub-micrometer length scales to generate plastic nanoparticles (NPs). Importantly, the environmental mobility, as well as the uptake and fate of these nanoscale particles in animals and humans can differ from larger microplastics of the same chemical composition.[119-121] Due to their large surface-to-volume ratio, NPs show unique interactions with cells and can serve as carriers for adsorbed toxicants.[122-124] Even materials that are benign in bulk form and free of adsorbed toxicants can show toxicity when formulated as NPs.[125-130] Given the unique physico-chemical properties associated with nanoscale sizes, it is prudent to distinguish nanoplastics from microplastics and to characterize its impact on animals and humans in detail.[131]

All plastic waste released into the environment is a potential source of nanoplastics, but the rate of NP formation from macroscopic plastic samples differs between polymers. Lambert *et al.* investigated the NP generation from seven macroscopic plastic materials (PE and PP pellets, PP film, PP sheet, PS coffee lid, PET water bottle, polylactic acid (PLA) cup) exposed to accelerated weathering conditions and found that PS and PLA generated the largest amount of NPs.[132] PS NPs can be synthesized with sharp size distributions and defined surface properties, which makes them ideal model systems for characterizing the effect of nanoplastics on cellular systems under defined conditions in this work.[133-138]

The most probable uptake route of PS NPs is *via* ingestion of contaminated food or water. After passing the stomach, the NPs reach the intestine, where nutrients are absorbed into the blood or lymph fluid for distribution throughout the body. NPs with diameters < 5 nm can cross the intestinal membrane barrier through paracellular diffusion.[139,140] Larger NPs can cross the intestinal membrane by persorption through degrading epithelial cells[121] or through energy-dependent transcytosis.[141-150] Another concern, in addition to NPs crossing the membrane, is that interactions between NPs and cells perturb cellular functions, damage the intestinal membrane integrity, and compromises its barrier function. Indeed, Thubagere *et al.* observed in an intestinal cell monolayer model that PS NP uptake can trigger oxidative stress and that the associated NP-induced hydrogen peroxide formation triggers a spread of apoptosis across the entire monolayer.[145] In another study it was shown that 4 h exposure to PS NPs disrupts iron transport across the intestinal epithelium, effectively inhibiting the absorption of the essential nutrient.[151] Although some previous studies have found no indications of PS NP-induced genotoxicity or loss of structural integrity in intestinal membranes models[152] there is also prior evidence that PS NPs can trigger genotoxicity in epithelial cells and macrophages.[153] Overall, the work performed so far confirms the possibility of detrimental interactions between nanoplastics and intestinal cells that – depending on NP concentration, surface charge, and size – poses a threat to the structural integrity of the entire intestinal membrane. A fundamental understanding of the interactions between nanoplastics and the intestinal membrane is therefore key for an accurate risk assessment and to develop effective strategies to mitigate potential detrimental effects. As interactions between NPs and intestinal cells are complex and depend on a large number of potential variables, *in vitro* intestinal membrane models are frequently used to investigate the effect of plastic NPs on the membrane integrity under defined conditions.[154-157] In these model systems, transepithelial electrical resistance (TEER) measurements facilitate a quantitative monitoring of membrane integrity and permeability.[158-160] Cytotoxicity and cell viability are quantified using MTT and Lactate dehydrogenase (LDH) assays, and the oxidative stress induced by NPs is determined through reactive oxygen species (ROS) measurements.[160-162] Optical and electron microscopies facilitate a characterization of transepithelial NP transport with subcellular spatial resolution.[163-166] These methods are well suited to characterize existing nanoplastics-induced damage to the intestinal membrane but they provide little to no direct information about the underlying molecular mechanisms and cannot detect the detrimental NP-cell interactions before they manifest in significant cellular damage. There is consequently a need for alternative tools and assays that provide deeper insights into NP-induced cellular responses and the associated mechanisms. Gene expression profiling is one such tool as it provides a detailed overview of changes in cellular function in response to NP exposure at the transcriptional level.[166,167] NPs also affect the cellular metabolism, and metabolomics is another potentially powerful approach for both detecting and characterizing cellular responses to NPs at a molecular level.[168-170] NP-induced differences in the cell metabolism cause changes in the composition of cells as well as the extracellular medium due to variations in the nature and quantity of the molecules uptaken by and released from the cells.[171] Although metabolomics is traditionally performed with mass spectroscopy, Raman spectroscopy, in particular surface enhanced Raman spectroscopy (SERS), has shown promise for the metabolic profiling of the cellular activity of bacterial cells and human cancer cells.[172-177] SERS is a vibrational spectroscopy that provides unique opportunities for signal amplification in aqueous media as water has low Raman cross-sections while the signal from Raman-active molecular vibrational modes in analytes can be enhanced by multiple orders of magnitude due to an electromagnetic enhancement effect in the vicinity of nanostructured noble metal surfaces.[178-180] This amplification of molecule-specific vibrational information facilitates a sensitive detection and identification of metabolites rapidly without the need for elaborate sample preparation or enrichment.

In this work, we combine TEER, ROS and cell viability measurements of a monolayer of intestinal cells with SERS measurements of the extracellular medium to 1.) determine PS NP conditions that result in a loss in membrane integrity and 2.) identify metabolomic changes that act as biomarkers for intestinal membrane damage.

3.2 Experimental Design and NP Characterization

We investigated PS NPs with a nominal diameter of 50 nm and with amine (NH_2-PS) or carboxylate (COOH-PS) surface ligands. The hydrodynamic diameter and zeta potential of the NPs in water and growth medium are summarized in Table 2. In water, the hydrodynamic diameter is 57 ± 5 nm for NH_2-PS, and 64 ± 8 nm for COOH-PS, and the zeta potential of NH_2-PS is

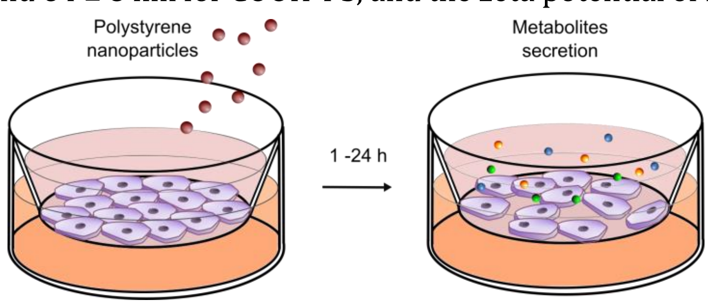

Figure 3.1 Schematic drawing of the experimental setup.

Table 2. Nanoplastic particles characterization (t=0h, n=10)

Particle	D_H in MQ water	D_H in growth medium	ζ in 10mM NaCl	ζ in growth medium
NH_2-PS	57±5 nm	96±12 nm	48.7±2.1 mV	-6.1±1.2 mV
COOH-PS	64±8 nm	89±13 nm	-50.7±2.3 mV	-9.6±0.7 mV

48.7 ± 2.1 mV compared to -50.7 ± 2.3 mV of COOH-PS. In growth medium, the initial hydrodynamic diameter increases to 96 ± 12 nm for NH_2-PS and 89 ± 13 nm for COOH-PS, and we measured a zeta potential of -6.1 ± 1.2 mV for NH_2-PS and -9.6 ± 0.7 mV for COOH-PS. We attribute the nearly identical zeta potentials for both NH_2-PS and COOH-PS and its low absolute value in growth medium that is rich in proteins and other biopolymers to non-specific protein adsorption, *i.e.* corona formation.[183-185] The hydrodynamic diameter of both NH_2-PS and COOH-PS in growth medium gradually increases as function of time and converges against approximately 350 nm

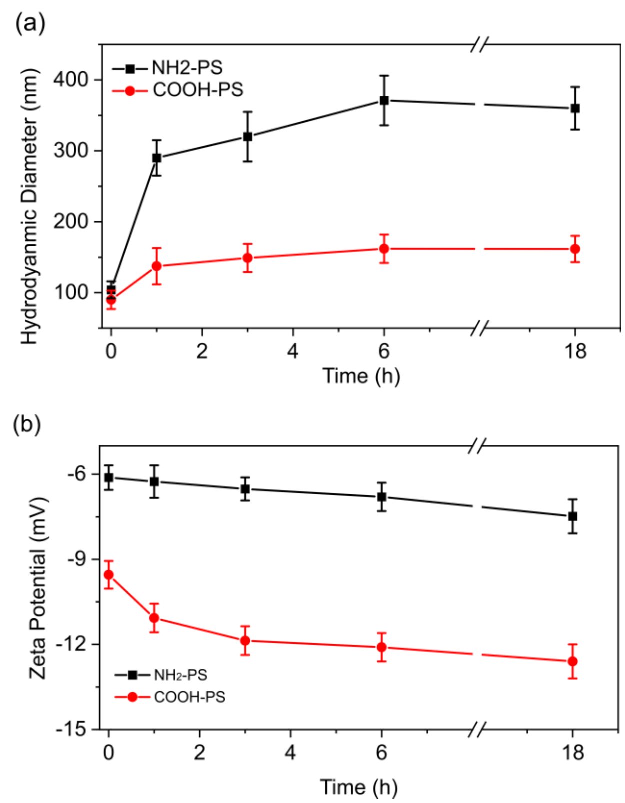

Figure 3.2 a) Hydrodynamic diameter, b) zeta potential of NH_2-PS and COOH-PS (1×10^{12} particles/mL) in growth medium as function of time. The reported results represent the mean of 3 independent experiments.

in the case of NH_2-PS and 150 nm in the case of COOH-PS after ~6 h (Figure 3.2 a). The zeta potential of two PS NPs in the culture medium decreases as function of incubation time (Figure 3.2 b). Different net increments in the size and surface charge of NH_2-PS and COOH-PS indicate different protein corona formation around particle surface. SEM images (Figure 3.3) reveal that this additional increase in the hydrodynamic diameter is due to some self-association of the PS-NPs. The different NP stabilities (*i.e.* hydrodynamic diameters) point to differences in the composition and structure of the corona formed around NH_2-PS and COOH-PS.

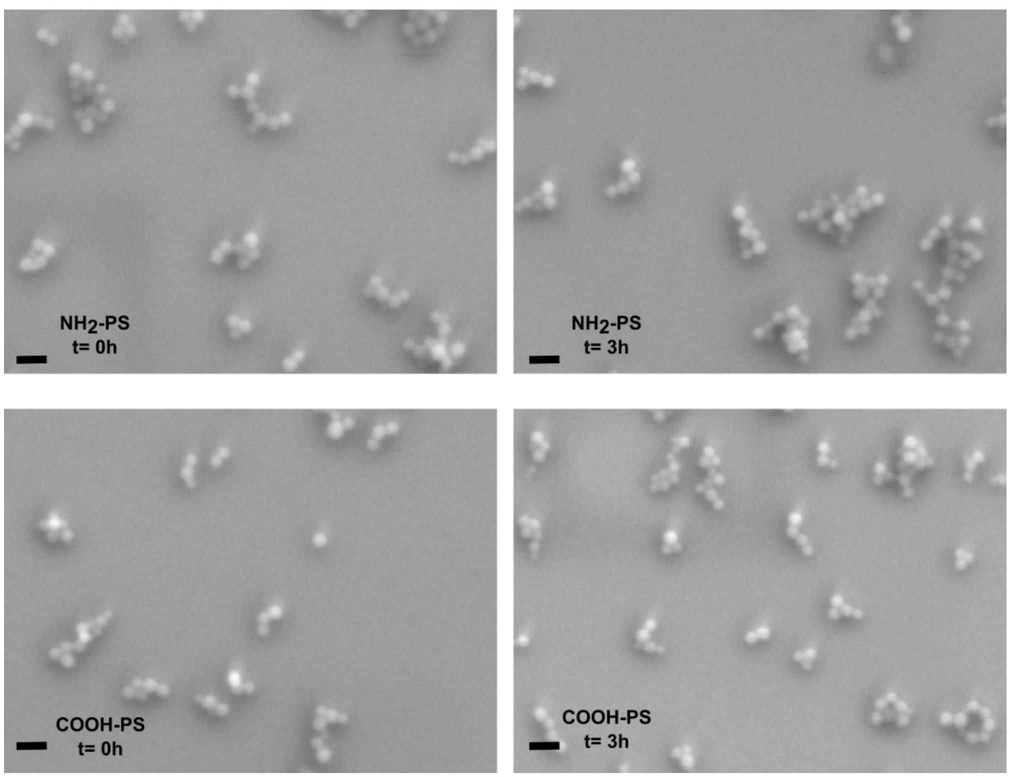

Figure 3.3 SEM images of NH_2-PS and COOH-PS in growth medium for t= 0h and t= 3h. Scale bar: 100 nm.

Caco-2 cells are human colon carcinoma cells that grow into a monolayer on permeable membranes. The cells can be induced to differentiate into mature absorptive enterocytes with well-developed microvilli, tight apical junctions, and a polarized distribution of membrane components.[154-156, 186-189] Due to the resemblance of Caco-2 cells with intestinal enterocytes, differentiated Caco-2 cell monolayers are a common model system to study the transepithelial membrane transport of various NPs, including polymeric NPs,[186-188] plastic NPs,[148-153], metal and metal-oxide NPs,[189-192] and micelles[193] at a fraction of the cost and without the ethical implications of a small animal experiment. In this work, NH_2-PS and COOH-PS were

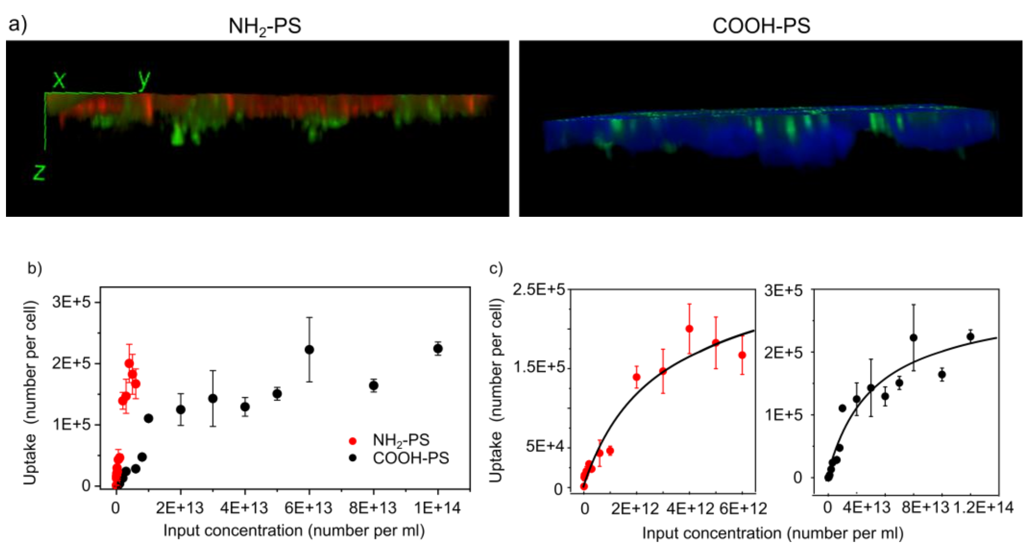

Figure 3.4 a) Confocal 3D images of a monolayer of Caco-2 cells show particle uptake (green) into the cells after 6h incubation. Cell junctions at the apical surface were stained with ZO-1 antibody (red) (top), and nuclei were stained with Hoechst 33324 (blue) (bottom). b) NH_2-PS (red) and COOH-PS (black) uptake by a monolayer of Caco-2 cells as function of NP input concentration, measured 6 hours after NP addition. c) Fits to the concentration-dependent uptake for NH_2-PS (left) and COOH-PS (right). Number of independent experiments, n=20.

incubated with differentiated monolayers of Caco-2 cells for 6 h or 18 h. Subsequently, the effect of the PS NPs on the intestinal membrane health was evaluated, and a SERS analysis of the medium was performed to identify changes in the cellular metabolism.

3.3 NH_2-PS and COOH-PS Uptake by Caco-2 Cells

Confocal microscopy scans confirmed that both NH_2-PS and COOH-PS bind to and get internalized by Caco-2 cells (Figure 3.4a). The confocal images taken after 6 h show an accumulation of NPs within the cell interior. We quantified the uptake of fluorescent NH_2-PS and COOH-PS by a Caco-2 cell monolayer for concentrations in the range of 0 – $1x10^{14}$ NPs/mL (Figure 3.4b, c). The NPs were incubated with the cells for 6 h before the number of uptaken NPs was determined by measuring their fluorescence signal. For both surface chemistries, we observed a hyperbolic increase in the number of uptaken NPs as function PS NP input, but the affinity of NH_2-PS was significantly higher than for COOH-PS. NP uptake was well described by a Hill-Langmuir like expression of the form $NP_{assoc}=NP_{\max}\frac{[NP]}{K+[NP]}$ where $NP_{assoc.}$ is the number of NPs per cell, NP_{max} is the maximum number of NPs uptaken by the cells, [NP] is the input concentration of NPs, and K is a NP-specific parameter that describes binding and uptake in differentiated Caco-2 cell monolayers. A smaller value of K indicates a higher binding affinity and increased uptake. Our fits yielded K = $2.6x10^{12}$ NPs/mL (4.1

nM) for NH_2-PS compared to $2.6x10^{13}$ NPs/mL (41.0 nM) for COOH-PS. Although the higher NH_2-PS internalization at low NP input concentrations indicate a higher binding affinity to Caco-2 cells than for COOH-PS, both NH_2-PS and COOH-PS achieved essentially the same maximum NP concentration of NP_{max} = $2.8x10^5$ NPs/cell (NH_2-PS) and $2.6x10^5$ NPs/cell (COOH-PS) in the asymptotic limit of high input concentrations.

The preferential uptake of NH_2-PS is overall consistent with previous studies that compared the uptake of amine and carboxylic-acid functionalized NPs. As the zeta potentials of NH_2-PS and COOH-PS under cell culture conditions were nearly identical (Table 2, Figure 3.2b). We attribute the differences in binding and uptake to differences in the corona assembled around NH_2-PS and COOH-PS NPs rather than the charge itself. Positively charged NPs have a higher affinity for serum proteins,[198] so that the surface properties of NH_2-PS and COOH-PS are expected to result in coronas with different composition in biological media.[189] It was shown previously that NH_2-PS contain a higher number of apolipoproteins in the corona than COOH-PS,[184] which can have a direct effect on NP uptake.[88] The difference in particle size due to self-association observed for longer incubation times (Figure 3.2a) may also contribute to differences in the uptake between NH_2-PS and COOH-PS.

The effect of PS NPs on the intestinal membrane is expected to be concentration and time dependent. Concentrations of up to 0.1 mg/mL of

PS NPs were shown to have negligible effect on membrane integrity within an exposure time of 24 h.[162] We expanded the concentration range to 0.07 – 7 mg/mL ($1x10^{12}$ – $1x10^{14}$ NPs/mL) in this work to ensure a measurable damage to the membrane within the limited observation time of our experiments (18 h). Specifically, we distinguished two separate input conditions that resulted in a "high" and "low" level of PS NP uptake. For the former we used a COOH-PS input concentration of $1x10^{14}$ NPs/mL and a NH_2-PS input concentration of $6x10^{12}$ NPs/mL, which yielded comparable uptake levels of around $2x10^5$ NPs/cell after 6 h and 18 h (Figure 3.5). These high NP concentration conditions were complemented by a set of lower NP input conditions, $6x10^{12}$ NPs/mL of COOH-PS and $1x10^{12}$ NPs/mL of NH_2-NPs, which generated a NP uptake that was lower by a factor of 4-5 at the same time points. We validated that none of the selected NP conditions affected the pH of the growth medium. The selection of NH_2-PS and COOH-PS input concentrations that yielded nearly identical uptake levels in Caco-2 facilitated a systematic comparison of the effects of NH_2-PS and COOH-PS on Caco-2 cells and the intestinal membrane model as a whole.

3.4 Effect of PS NPs on ROS Levels and Cell Viability

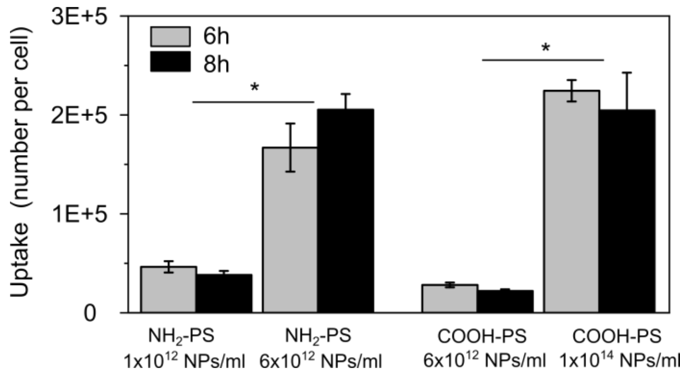

Figure 3.5 Particle uptake in the Caco-2 cell monolayer after incubation with NH_2-PS (Low: 1x10^{12} NPs/mL and high: 6x10^{12} NPs/mL) and COOH-PS (Low: 6x10^{12} NPs/mL and high: 1x10^{14} NPs/mL) for 6 and 18 h. $p<0.05$, n=20.

Reactive oxygen species (ROS) generation is a cellular stress response to the uptake of non-biodegradable NPs, including nanoplastics,[201-203] and it was shown before that NP-induced increases in ROS can result in a loss of Caco-2 membrane integrity.[145] We quantified the ROS levels in Caco-2 incubated with NH_2-PS and COOH-PS at concentrations of 1x10^{12}, 6x10^{12} NPs/mL for the former, and 6x10^{12}, 1x10^{14} NPs/mL for the latter at three time points (1h, 3 h, 6 h, 18 h) after PS NP addition (Figure 3.6a). We included cells with no treatment and cells treated with H_2O_2 as negative and positive controls, respectively. After 6 h of incubation we detected ROS concentrations that were significantly increased relative to the no treatment control for both concentrations of NH_2-PS and COOH-PS. The ROS generation increased with concentration and was generally higher for COOH-PS. After 18 h, the ROS levels had decreased and were no longer significantly different from the no-treatment control for any of the investigated experimental conditions.

In the next step, we assessed the effect of NH_2-PS ($1x10^{12}$ or $6x10^{12}$ NPs/mL) and COOH-PS ($6x10^{12}$ or $1x10^{14}$ NPs/mL) on cell viability. To that end, we performed microculture tetrazolium (MTT) assays (Figure 3.6b) 6 h and 18 h after NP addition. Living cells convert the yellow 3-(4, 5-

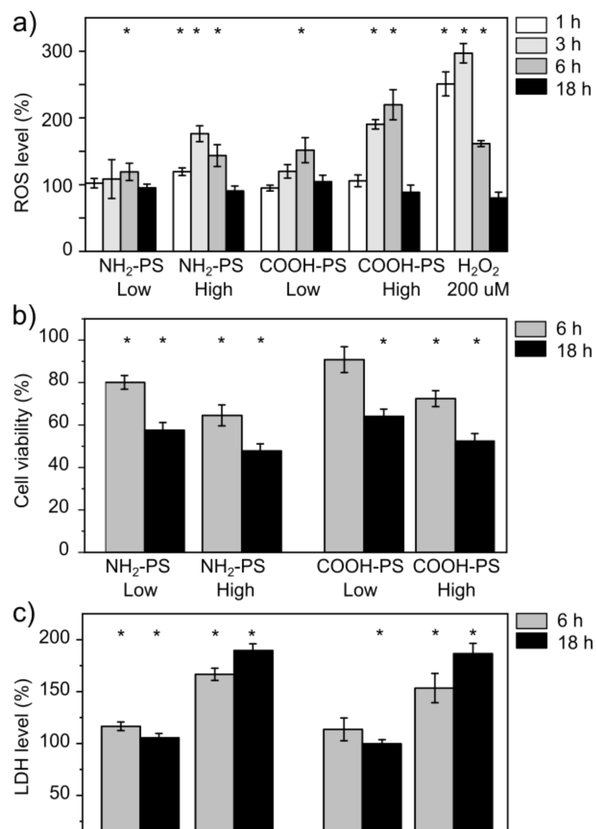

Figure 3.6 Characterization of monolayers of Caco-2 cell by a) cell viability, b) LDH level, and c) ROS level after incubation with NH2-PS (Low: $1x10^{12}$ NPs/mL and high: $6x10^{12}$ NPs/mL) and COOH-PS (Low: $6x10^{12}$ NPs/mL and high: $1x10^{14}$ NPs/mL) for 6 and 18 h. Results were normalized with the control group. $p<0.05$, $n=20$.

dimethylthiazol-2-yl)-2,5-diphenyltetrazolium bromide into a purple formazan and the conversion can be quantified colorimetrically. We detected a significant reduction in formazan signal relative to the no treatment control for high and low concentrations of NH_2-PS at both time points. In the case of low concentrations of NH_2-PS at both time points. In the case of low concentrations of COOH-PS, the MTT values are significantly reduced after 18 h but not 6 h. In the case of high concentrations of COOH-PS, both 6 h and 18 h yield significantly reduced MTT levels of incubation with low concentrations of NPs and for both 6 h and 18 h for high concentrations. For both flavors of NPs the formazan intensity decreased with input concentration and exposure time, but the reduction was overall stronger for NH_2-PS than for COOH-PS. We applied lactate dehydrogenase (LDH) assays as a second strategy to characterize the cytotoxicity of NH_2-PS and COOH-PS 6h and 18 h after addition of the PS NPs (Figure 3.6c). LDH is a cytosolic enzyme that is released into the ambient medium when the integrity of the cell plasma membrane is damaged and becomes permeable. For the low concentration conditions of NH_2-PS and COOH-PS, the LDH levels show only modest differences relative to the no-treatment control, but for high concentrations of both NH_2-PS and COOH-PS a strong increase of LDH levels is detected at both 6 h and 18 h. Both MTT and LDH assays confirm that NH_2-PS and COOH-PS can reduce the viability of Caco-2 cells and that the effect increases with NP input concentration and incubation time. Overall, we find that NH_2-PS and COOH-PS have similar effects on the cell viability for input concentrations that yield similar NP uptake.

3.5 Characterizing the effect of PS NPs on the Caco-2 Membrane Integrity

To test for a potential PS-NP induced damage to the Caco-2 cell monolayer, we mapped dead cells with a live/dead stain through fluorescence microscopy (Figure 3.7a). We performed these experiments with both NH_2-PS and COOH-PS at high and low input concentrations 6 h and 18 h

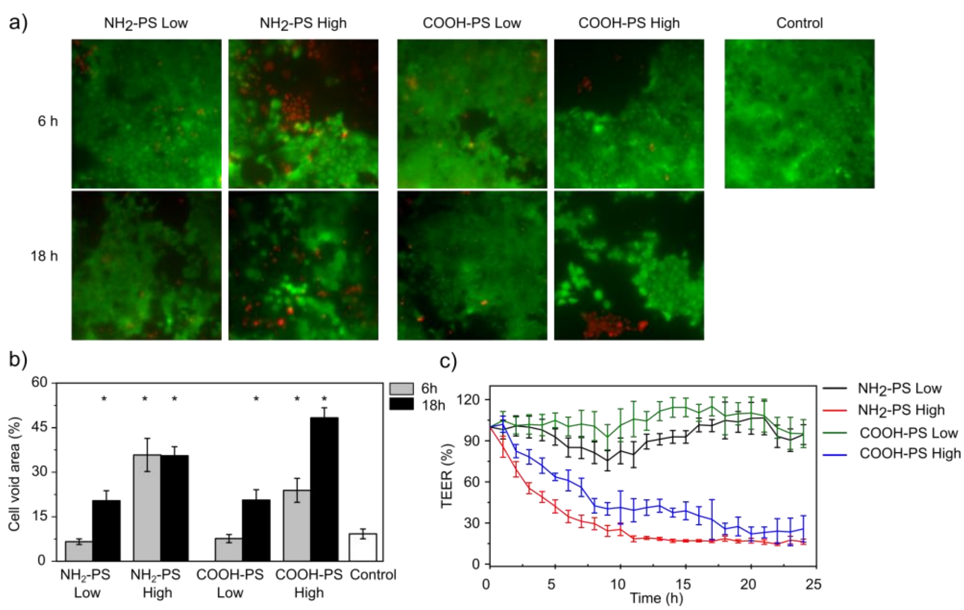

Figure 3.7 a) Fluorescence images of Caco-2 cell monolayer treated with NH_2-PS (low: 1×10^{12} and high: 6×10^{12} NPs/mL) and COOH-PS (low: $6x10^{12}$ and high: $1x10^{14}$ NPs/mL) for 6 and 18h and treated with a live (green) / dead (red) stain. b) Quantification of the membrane areas void of cells (in %). $p<0.05$, n=10. c) TEER for monolayers of differentiated Caco-2 cells as function of time when incubated with NH_2-PS and COOH-PS. Results were normalized with the control group. n=10.

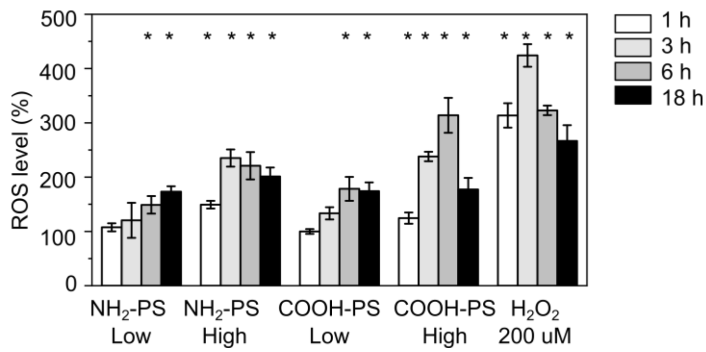

Figure 3.8 Characterization of ROS after incubation of monolayers of Caco-2 cell with NH_2-PS ($1x10^{12}$ NPs/mL and $6x10^{12}$ NPs/mL) and COOH-PS ($6x10^{12}$ NPs/mL and $1x10^{14}$ NPs/mL) for 6 and 18 h. ROS level were normalized with cell numbers in each condition. The data was then normalized with the control group and are given in % (100% = control). H_2O_2 was included in as positive control. n=20, $p<0.05$.

after addition of PS NPs. We also included images of controls not exposed to NPs. In the absence of PS NPs and at low NP input concentrations the fluorescence images show an intact membrane of living (green) cells with only a few dead (red) cells whose frequency is higher for 18 h than for 6 h. For the high concentration conditions of NH_2-PS and COOH-PS, the number of dead cells increases and large areas void of cells emerge, presumably because dead cells have detached from the membrane support in these areas. Figure 3.7 b summarizes the area in % in the cell monolayer that is void of cells. The plot confirms that the "holes" in the cell monolayer increase in size with time and concentration of NPs. One exception is NH_2-PS at high concentrations, for which essentially identical areas void of cells were detected at 6 and 18h. A detachment of dead cells from the membrane also provides a potential explanation for the drop in cellular ROS levels observed for NP-treated cells between 6 h and 18 h in Figure 3.6a. Dead, detached cells are removed during the wash step, and a lower number of cells with increased ROS levels adherent to the filter support after 18 h of NP treatment could provide ROS levels that are comparable to those of a higher number of healthy control cells that generate less ROS per cell (Figure 3.8).

The observation of nanoplastics-induced cellular stress, reduced cell viability and holes in the cell monolayer indicate a loss in the stability of the intestinal model membrane after addition of PS NPs. The TEER is a convenient observable for quantifying the integrity of a monolayer of Caco-2 cells.[158-160] We measured the TEER of a Caco-2 cell monolayer when exposed to NH_2-PS at concentrations of 1×10^{12} and 6×10^{12} NPs/mL, or COOH-PS at concentrations of $6x10^{12}$ or $1x10^{14}$ NPs/mL every hour for a total of 24h (Figure 3.7c). All TEER values are normalized relative to the no treatment control at the same time point. The TEER values show a NP concentration dependent response. For NH_2-PS NPs with an input concentration of 1×10^{12} NPs/mL, the TEER value remains constant for the first 2h before it transiently decreases by approximately 30%. After approximately 10 h, the TEER starts to increase again and finally converges against the starting value prior to NP exposure. If the NH_2-PS NP concentration is increased to 6×10^{12} NPs/mL, a fast, continuous and non-reversible drop of the TEER value by nearly 80% of its initial value is observed within the first 10 h.

In the case of COOH-PS, we did not detect a clear decrease in TEER over the entire observation time for the low input concentration of $6x10^{12}$ NPs/mL, but an increase of the input concentration to $1x10^{14}$ NPs/mL resulted in a rapid and continuous decrease in TEER. The drop in TEER is similar in magnitude but slightly slower than the one observed for NH_2-PS with a concentration of 6×10^{12} NPs/mL. The need for a higher input concentration to achieve a comparable drop in TEER than for NH_2-PS is again attributed to the less efficient uptake of COOH-PS. The observed reductions in TEER for high concentrations of NH_2-PS and COOH-PS indicate an increased permeability of the cell monolayer due to a PS NP induced perturbation of the Caco-2 membrane. The strong increase in membrane permeability for high concentrations of NH_2-PS and COOH-PS is consistent with the substantial detachment of dead cells from the membrane observed for these conditions in the live/dead staining experiments in Figure 3.7a.

3.6 Vibrational Characterization of the Growth Medium of Caco-2 Cell Monolayers through SERS

After identifying PS NP conditions that result in a decrease of the Caco-2 cell monolayer integrity, we apply in this section SERS for a vibrational characterization of the medium in which the Caco-2 cells are cultured to screen for metabolomic changes induced by the PS NPs (Figure 3.9 a). The underlying hypothesis is that PS NP-induced changes in the cellular metabolism lead to changes in the extracellular medium through changes in the cellular uptake of nutrients from the medium or release of metabolites into the medium, and that these changes can be sensitively detected with no special sample preparation through SERS. Our approach aims to take advantage of the highly specific molecular information and the strong signal amplification provided by SERS and is further motivated by previous reports of a successful detection of biomarkers in serum using SERS in combination with chemometric analysis.[172, 204, 205]

The electromagnetic amplification of the Raman signal in SERS depends on the fourth power of the electric (E-)field ($\sim E^4$). SERS spectra are consequently typically recorded on nanostructured noble metal surfaces that provide strong local E-fields through excitation of Localized Surface Plasmon Resonances (LSPRs).[178-180,206] In this work, we prepared monolayers of gold NPs with a diameter of 78±1 nm by the Langmuir-Blodgett (LB) technique and transferred them onto a glass coverslip as SERS substrates (see Methods). An optical darkfield image of a substrate is shown in Figure 3.9b. SEM micrographs show a layer of closely packed NPs with nanoscale crevices and junctions between individual NPs (Figure 3.9d). Under resonant excitation, these nanogap structures form electromagnetic "hot-spots" that provide strong E-fields to amplify the

Raman signal of molecules localized to these gaps.[207] The scattering spectrum of the gold NP film (Figure 3.9c) shows a broad plasmon band that is strongly broadened and red-shifted when compared with the colloidal gold NP building blocks (inset in Figure 3.9c). The strong spectral shift of the plasmon confirms strong electromagnetic coupling between the NPs in the film. All SERS measurements reported in this study were

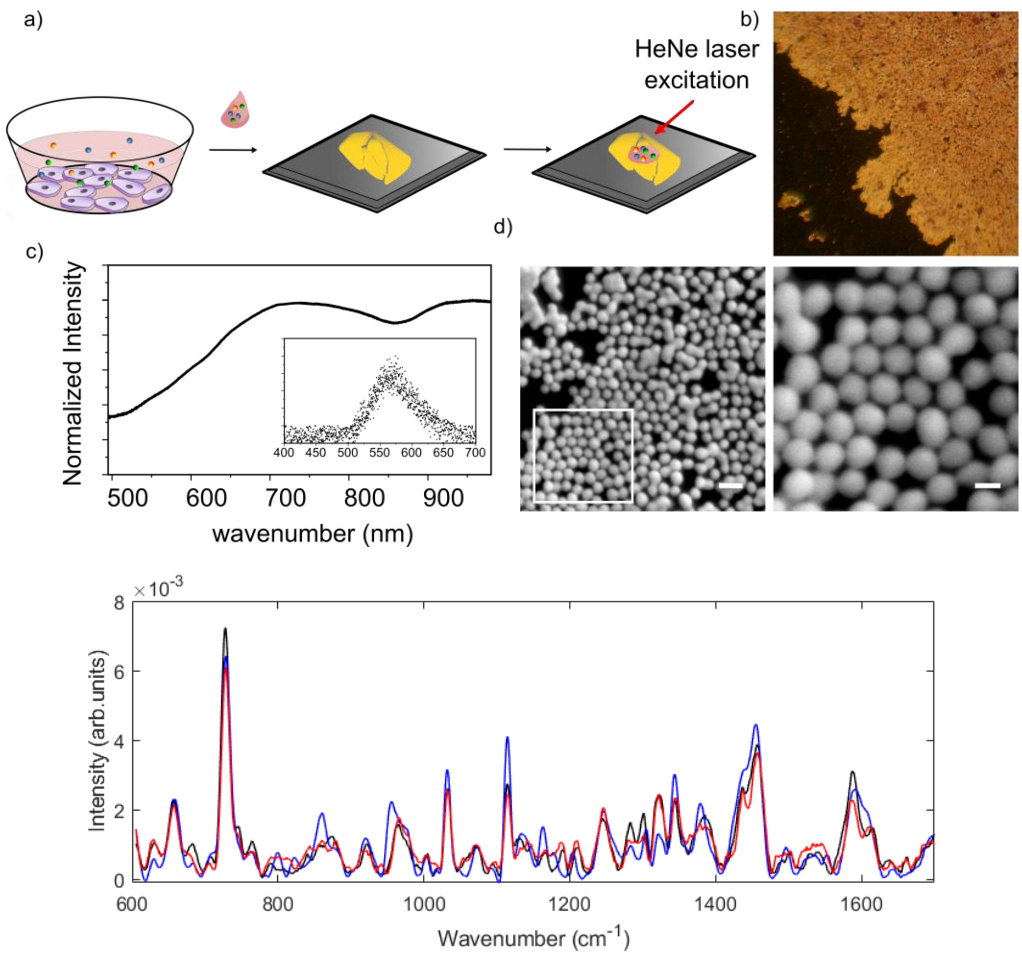

Figure 3.9 a) Schematic image of SERS measurement. b) Optical image of a gold NP (80 nm) monolayer used as SERS substrate in this work. c) Scattering spectrum of SERS substrates. Inset: Extinction spectrum of gold colloid nanoparticles. d) SEM images of a section of the gold NP film. Scale bar: 200nm (left), 100 nm (right). e) Three SERS spectra of medium collected from Caco-2 cells after 18 h of incubation with NH_2-NPs ($6x10^{12}$ NPs/mL).

performed with a laser excitation at 785 nm as it overlaps with the plasmon resonance of the gold NP film and because the fluorescence background is generally low in this wavelength range.

We recorded SERS spectra of growth medium collected from the apical compartment of the Caco-2 monolayers incubated with NH_2-PS ($1x10^{12}$ NPs/mL, $6x10^{12}$ NPs/mL) and COOH-PS ($6x10^{12}$ NPs/mL, $1x10^{14}$ NPs/mL) 6 h and 18 h after NP addition. At both time points we also measured SERS spectra of the growth medium collected from cells not incubated with NPs as well as of NH_2-PS and COOH-PS incubated in medium without cells as controls. The data analyzed in this work were collected on the same day on freshly prepared substrates. SERS measurements for each condition were performed with 5 biological replicates, each on a new SERS substrate. Five spectra were collected from one substrate, and each spectrum was obtained from a new location on the SERS substrate. Figure 3.9e shows three spectra of medium samples collected from NH_2-PS ($6x10^{12}$ NPs/mL) treated cells after 18 h of incubation. A close inspection of the three spectra recorded under identical conditions reveals some variability between the spectra. For some peaks the relative intensities differ between the spectra, while other peaks are only detectable in selected spectra. Due to the strong Raman signal intensity enhancement provided by electromagnetic hot-spots, the SERS signal recorded at a particular location of the SERS substrate depends on the chemical composition of the hot-spots. The biological medium investigated in this work has a complex composition, containing amino acids, lipids, carbohydrates, nucleic acids and other nutrients, as well as metabolites released from the cells. This chemical complexity can result in differences in the composition of the hot-spots and, thus, the recorded spectra.[208-212] In addition to the compositional heterogeneity, the hot-spots also have a morphological heterogeneity that results in differences in the E-field enhancement between individual hot-spots.[180] These two effects in addition to differences in the orientation of analyte molecules in the hot-spots are sources of variability in the recorded SERS spectra.[173]

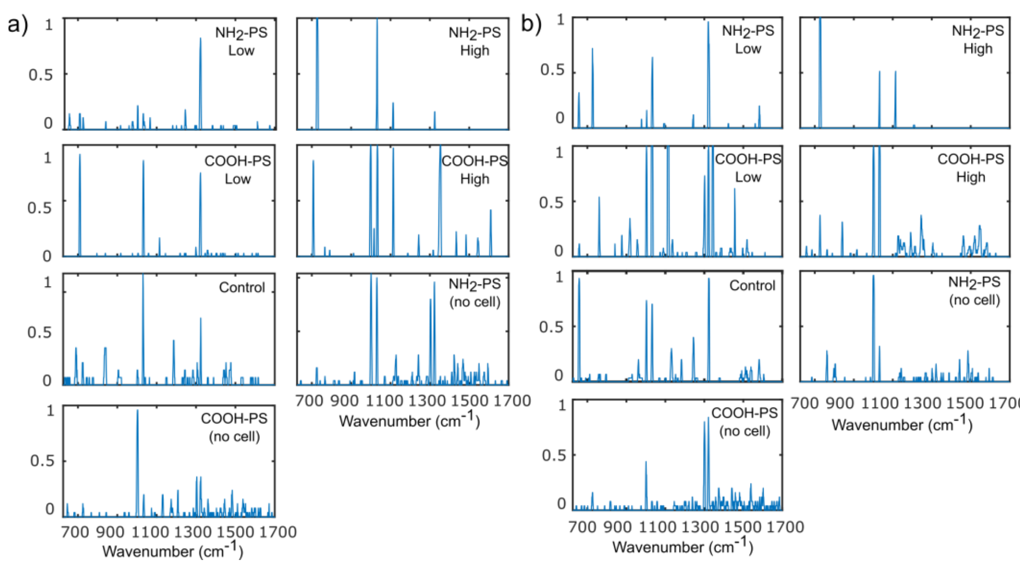

Figure 3.10 a) Histograms of the second derivative spectra collected from media incubated with NH_2-PS (1x10[12] NPs/mL (low), 6x10[12] NPs/mL (high)), COOH-PS (6x10[12] NPs/mL (low), 1x10[14] NPs/mL (high)), and no particles (NT control) for 6 h. The spectra for NH_2-PS (6x10[12] NPs/mL) and COOH-PS (1x10[14] NPs/mL) incubated in medium with cells are also included. b) Same data for 18 h.

Given the heterogeneity of the SERS spectra, each experimental condition is best described by an ensemble of spectra, and a systematic comparison between experimental conditions should be based on the analysis of the ensembles.[213] To obtain an overview of the spectral ensembles of this work, we calculated the second derivative spectra and determined the maxima, defined as all features with a negative second derivative whose absolute value was at least 2.5 standard deviations higher than the noise in each spectrum. The fraction of spectra containing the identified maxima provide a measure of the relative frequency of that feature in the ensemble. The histograms of the peak positions obtained in this way are summarized in Figure 3.10 for the different experimental conditions recorded 6 h or 18 h after addition of the NPs. A visual inspection of the histograms suggests differences in the spectra recorded for PS NP treated cells and no treatment controls as well as between the different NP conditions. To corroborate this hypothesis and to identify the spectral features that are responsible for the differences, we next applied artificial intelligence and chemometric data analysis strategies. T-distributed stochastic neighbor embedding (t-SNE) is a machine learning algorithm for dimensionality reduction and visualization that we utilized to obtain an overview of the SERS spectra recorded for the different experimental conditions in a reduced dimensionality space.[102] Each point in the t-SNE plot in Figure 3.11 represents a single SERS measurement. At 6 h (Figure 3.11a), the spectra recorded for high concentrations of NH_2-PS and COOH-PS separate clearly from each other and the no treatment and NP controls. The no treatment and NP controls also cluster at 6 h, but the individual clusters are less well defined and separated. With increasing time, the clustering overall improves and the individual clusters become more distinct at 18 h (Figure 3.11b). The clustering of the spectra in the t-SNE plots confirms that the spectra of one condition share similarities with each other and systematic differences with other conditions.

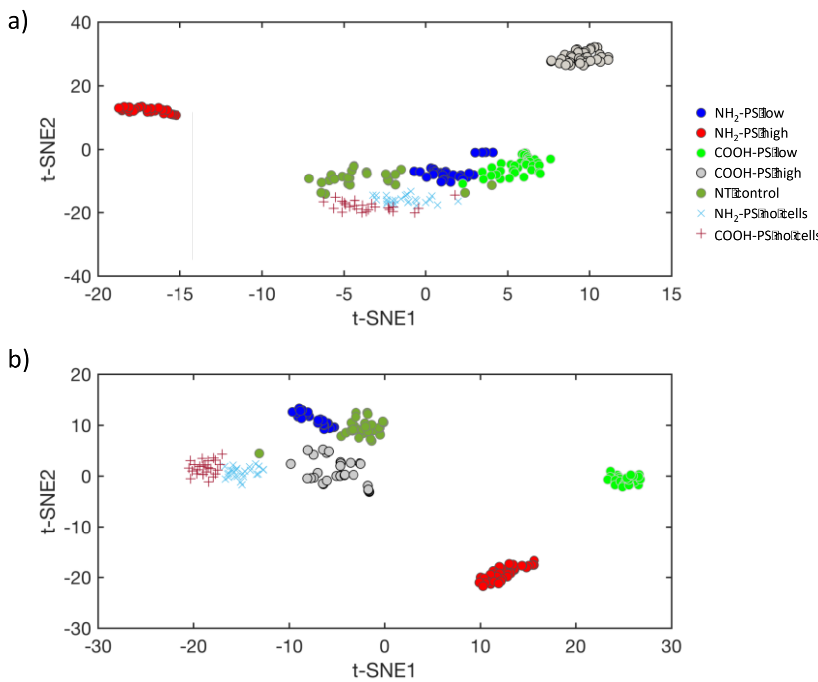

Figure 3.11 t-Distributed stochastic neighbor embedding (t-SNE) analysis of the second derivative SERS spectra of the medium collected from Caco-2 cells incubated with COOH-PS ($6x10^{12}$ NPs/mL, $1x10^{14}$ NPs/mL), NH_2-PS ($1x10^{12}$ NPs/mL, $6x10^{12}$ NPs/mL), no treatment controls (medium with NPs), and NH_2-PS and COOH-PS (NPs incubated in medium without cells) collected a) 6 h and b) 18 h after NP addition.

To further characterize the degree of similarity and dissimilarity between the different conditions, as well as to identify the spectral features that are responsible for the differences, we next performed unsupervised and supervised multivariate discriminant analyses of the second derivative spectra. Specifically, we performed Principal Component Analysis (PCA)[215] and principal component discriminant analysis (PCA-LDA)[216]. PCA is used to reduce the number of variables of a data set by projecting the data onto

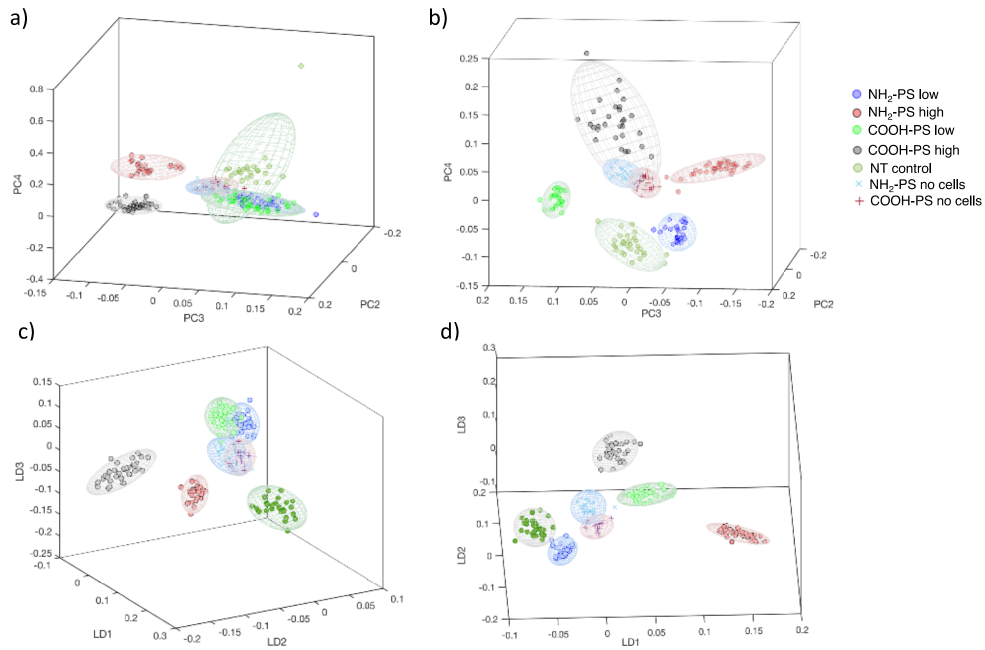

Figure 3.12 a-b) PCA score plots (PC2-4 space) of the SERS spectra recorded of medium containing cells incubated with NH_2-PS ($1x10^{12}$ NPs/mL (low) and $6x10^{12}$ NPs/mL (high)), COOH-PS ($6x10^{12}$ NPs/mL (low) and $1x10^{14}$ NPs/mL (high)), no NPs (NT control), as well as for NPs in medium without cells after a) 6h and b) 18h. c-d) PC-LDA score plots (LD1-3 space) of the SERS spectra recorded of medium containing cells incubated with NH_2-PS ($1x10^{12}$ NPs/mL (low) and $6x10^{12}$ NPs/mL (high)), COOH-PS ($6x10^{12}$ NPs/mL (low) and $1x10^{14}$ NPs/mL (high)), no NPs (NT control), as well as for NPs in medium without cells after c) 6h and d) 18h.

a lower dimensional space spanned by so-called principal components (PCs) that are weighed linear combinations of the original variables. In the reduced presentation, the individual spectra are defined by "scores" for the individual PCs. In PCA-LDA, linear discriminant analysis (LDA) is subsequently applied on the reduced data presentation to maximize the separation between the individual groups of observations, yielding a set of scores on a new set of linear discriminant (LD) axes. Importantly, the PCs and LDs that can separate the SERS spectra of different groups contain information about the spectral features that are responsible for the systematic differences.

Figure 3.12a,b shows PCA score plots in the PC2-4 space for the spectra recorded (a) 6 h and (b) 18 h after PS NP addition. After 6 h, the spectra of high concentrations COOH-PS and NH_2-PS are well separated from each other and all other conditions, which implies i.) that these two conditions have a particular strong effect on the cells and ii.) that the cellular responses to these two NPs with different surface chemistries differ. The spectra obtained for low concentrations of COOH-PS and NH_2-PS form clusters that lie close together. Likewise, the clusters of the no treatment control and of COOH-PS and NH_2-PS incubated with growth medium in the absence of cells also overlap, albeit in a separate region of the PC2-4 space than the spectra collected from cells incubated with PS NPs. Based on this clustering pattern, we can conclude that low concentrations of both flavors of PS NPs induce detectable cellular changes already after 6 h, but that the spectral differences between low concentrations of COOH-PS and NH_2-PS are still modest. After 18 h, the separation between the individual groups has overall improved, but the clusters for the low concentration of NH_2-PS and the no treatment control still overlap in the PCA score plot as do the clusters for the NH_2-PS and COOH-PS no cells controls. PCA-LDA yields overall similar trends as PCA but with further improved separation between the clusters in the LD1-3 space (Figure 3.12c, d). For the data set recorded after 6h, PCA-LDA achieves a clear separation of both high and low concentrations of COOH-PS and NH_2-PS from the no treatment and NP controls. For the data recorded after 18 h, PCA-LDA achieves more compact clusters and better separations between the clusters when compared with PCA performed at the same time point. At 18 h, the only clusters whose 90% confidence intervals still overlap in the LD1-3 space are the COOH-PS and NH_2-PS no cells controls, which are conditions for which no change in the growth medium is expected.

Overall, the multivariate data analysis is consistent with the t-SNE analysis and confirms that both COOH-PS and NH_2-PS induce changes in the composition of the growth medium and that these changes increase with the concentration of the NPs and incubation time. Intriguingly, although COOH-PS and NH_2-PS were compared under conditions that yield comparable uptake, the SERS spectra of the medium collected from cells treated with these particles can be distinguished not only from the no treatment control but also from each other. The spectra of all PS NP treated cells separate from the no treatment controls along LD1 in Figure 3.12d, while the spectra of COOH-PS and NH_2-PS separate along LD3. This finding suggests that all PS NPs elicit a significant metabolomic response, but it also implies that the cellular responses to COOH-PS and NH_2-PS are not completely identical. Information about the spectral features that are responsible for separating the different conditions in PCA or PCA-LDA score plots are contained in the loading spectra. These spectra plot the

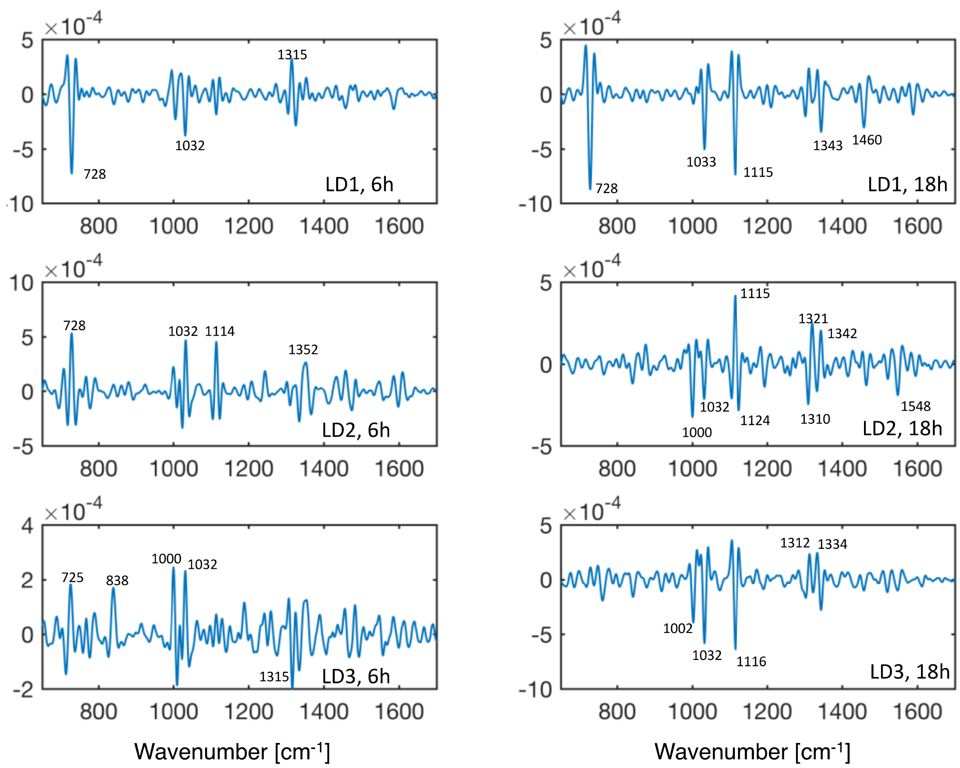

Figure 3.13 Loading spectra of the first three discriminants LD1-3 (top to bottom) for the data set recorded after 6h (left) and 18h (right).

contribution of each wavenumber to a PC or LD. We focus here on the analysis of LDs as PCA-LDA provides the clearest separation between the different experimental conditions. The loading spectra for LD1-3 after 6 h

Table 3. SERS band assignments for prominent peaks identified in PCA-LDA analysis.

SERS peak (cm^{-1})	**Vibrational mode**	**Major Assignments**
705	N-H bending	Proteins
712	C-N	Lipids, DNA/RNA
728	C-H ring bending	Hypoxanthine
1001	C-H ring stretching	Phenylalanine
1033	C-H ring bending	Phenylalanine
1115	C-N stretching	Protein
1320	C-O stretching CH2 twisting	Lipids Adenine DNA/RNA
1345	C-H stretching	Lipids
1457	C-C ring stretching N=N stretching CH_2 bending	Phospholipids Collagen
1547	C-C stretching	Protein
1610	C=O stretching	Amide I

and 18 h are plotted in Figure 3.13a, 9b. The spectral features that have prominent contributions in multiple loading spectra include peaks at (+/- 3 cm^{-1}) 728 cm^{-1} ($LD1^{6h}$, $LD2^{6h}$, $LD1^{18h}$), 1001 cm^{-1} ($LD3^{6h}$, $LD2^{18h}$, $LD3^{18h}$),1031 cm^{-1} ($LD1^{6h}$, $LD2^{6h}$, $LD1^{18h}$, $LD2^{18h}$, $LD3^{18h}$), 1115 cm^{-1} ($LD1^{6h}$, $LD2^{6h}$, $LD1^{18h}$, $LD2^{18h}$, $LD3^{18h}$), 1320 cm^{-1} ($LD3^{6h}$, $LD2^{18h}$), and 1343 cm^{-1} ($LD1^{18h}$, $LD2^{18h}$). In LDx^{y}, x specifies the number of the LD and y the time of sampling. The detailed peak assignments of all loading spectra are summarized in Table 3. The prominent feature at 728 cm^{-1} in LD1, which separates the spectra of the no treatment control and PS NP incubated

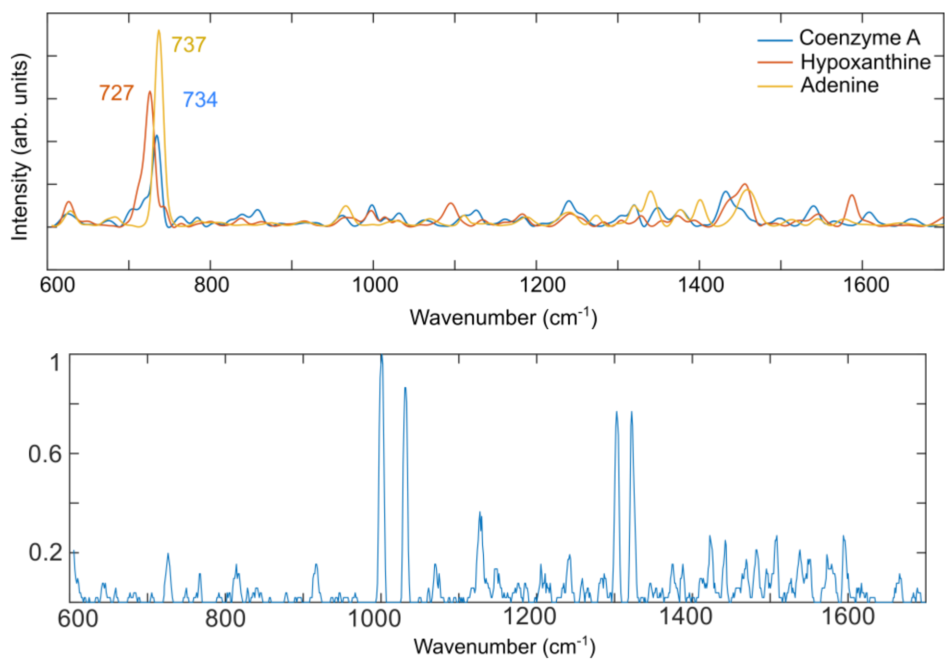

Figure 3.14 a) SERS spectrum of 1 μM of Coenzyme A, hypoxanthine and adenine in growth medium. SERS spectrum of each molecule in figure represent an average of 16 spectra. The predominant peak wavenumber of each molecule was labeled. b) Histograms of the second derivative spectra collected from growth medium background. Data in the figure includes 25 SERS spectra.

cells, is characteristic of the ring-breathing modes in purines and could indicate adenine, coenzyme A or hypoxanthine. We tested these three components under the identical experimental conditions and determined that hypoxanthine provides the best fit (Figure 3.14a). The features at 1001 cm^{-1} and 1033 cm^{-1} are characteristic of phenylalanine, 1115 cm^{-1} lies in the range of the C-C and C-N stretching modes of lipids and proteins, and 1320 cm^{-1} and 1340 cm^{-1} are assigned to C-O and C-H stretching modes. While the modes at 1001 cm^{-1}, 1033 cm^{-1}, 1115 cm^{-1}, and 1320 cm^{-1} and 1340 cm^{-1} are common in the growth medium, the 728 cm^{-1} mode is rarely detected in the spectra of plain growth medium (Figure 3.14b). The 728 cm^{-1} feature is, however, very prominent in the second derivative spectra of medium collected from cells treated with high and low concentrations of NH_2-PS for 18 h, with high concentrations NH_2-PS for 6 h, and with high concentrations of COOH-PS for 18 h (Figure 3.13). The integrated 728 cm^{-1} peak intensity, which correlates with the hypoxanthine concentration in the medium, is increased relative to the no treatment control for all PS-NP conditions (Figure 3.15a). The 728 cm^{-1} signal intensity is particularly high for high concentrations of NH_2-PS and COOH-PS at 18 h and to a somewhat lower degree for high concentrations of NH_2-PS at 6 h as well as for low concentrations of NH_2-PS at 18 h. High concentrations of NH_2-PS and COOH-PS are associated with a strong drop in TEER (Figure 3.7c), and incubation of Caco-2 membranes with low concentrations of NH_2-PS for 18 h also results in some membrane damage (Figure 3.7b). The observation of increased 728 cm^{-1} peak intensities for conditions that result in increased Caco-2 membrane damage suggest a relationship between hypoxanthine concentration in the medium and Caco-2 cell damage. To formally test this hypothesis, we correlated the peak intensity at 728 cm^{-1} with TEER (Figure 3.15b) and the area in the Caco-2 cell monolayer void of cells (Figure 3.15c). The Pearson correlations coefficients are R = -0.93 and 0.84, respectively. The strong (anti)correlation confirms that increased levels of

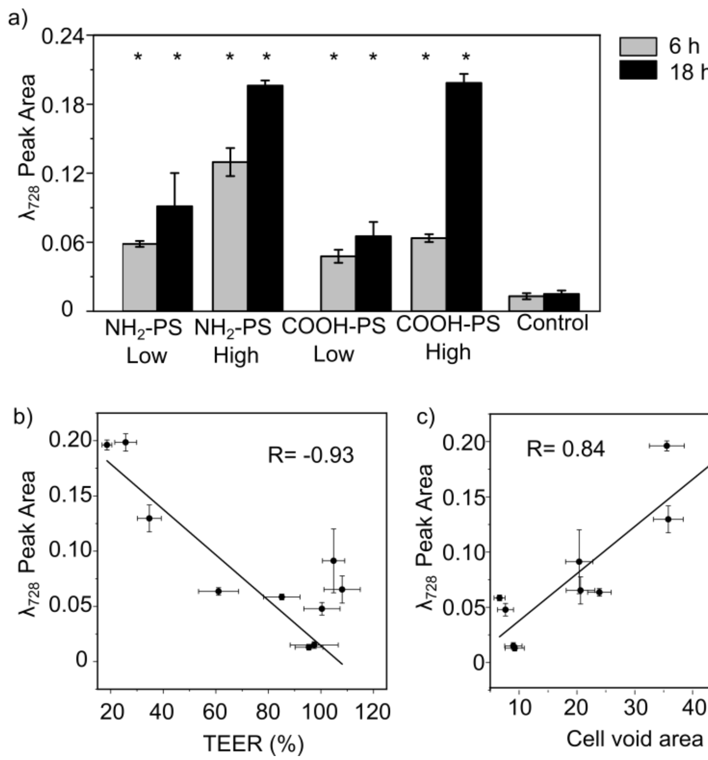

Figure 3.15 a) Integrated area of the 728 cm^{-1} peak in the SERS spectra of Caco-2 monolayers treated with NH_2-PS (1x10^{12} NPs/mL and 6x10^{12} NPs/mL), COOH-PS (6x10^{12} NPs/mL and 1x10^{14} NPs/mL) for 6 h or 18 h, and Caco-2 cells without treatment as the control group. The peak areas were determined by Lorentzian fits. b). Peak area at 728 cm^{-1} as function of TEER value. c) Peak area at 728 cm^{-1} as function of area of Caco-2 membrane void of cells in % at 18 h. n=25 ,$p<0.05$.

hypoxanthine in the medium are associated with PS NP induced cell stress and that they are particularly high under conditions that lead to cell death and increased permeability of the Caco-2 cell monolayer. Hypoxanthine acts as a marker for nanoplastics-induced damage to the Caco-2 intestinal membrane model. This interpretation is corroborated by previous studies that identified hypoxanthine as a marker for the dysregulation of epithelial cell membranes.[217] In particular, combined HPLC and TEER measurements have shown previously that hypoxanthine concentration and barrier function of an epithelial membrane are inversely correlated.[105] We determined a SERS detection limit of 10 nM for hypoxanthine in medium under our experimental conditions (Figure 3.16), which underlines the potential of SERS as sensitive diagnostics for intestinal

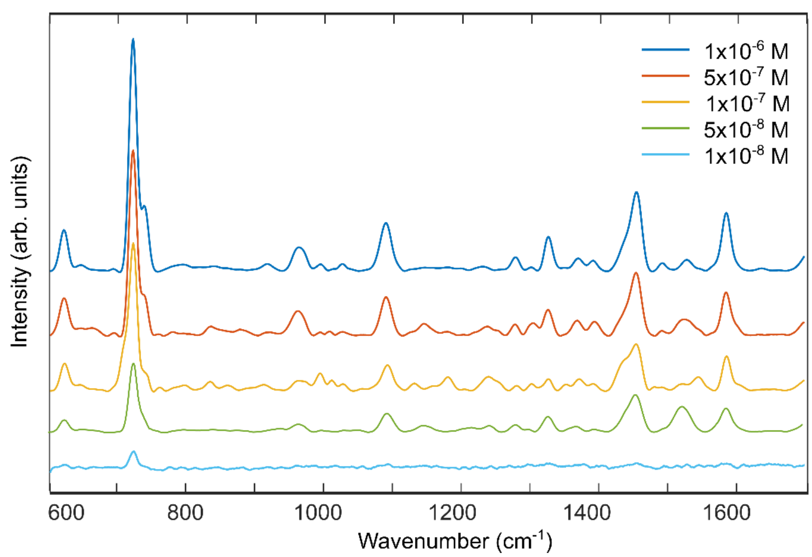

Figure 3.16 The SERS spectra of different concentration of hypoxanthine. The detection limit of hypoxanthine is 10nM. SERS spectrum of each condition in figure represent an average of 16 spectra.

stress metabolites with potential applications for monitoring intestinal membrane health both *in vitro* and *in vivo*.

3.7 **Conclusion**

Given the ubiquitous distribution of plastics in the environment, it is important to develop a better understanding of the fate of nanoscale plastic particles after uptake and how they affect the organs and cells. In this work, we investigated the impact of NH_2-PS and COOH-PS with a nominal diameter of 50 nm as nanoplastics mimic on an *in vitro* intestinal membrane model based on differentiated Caco-2 cells. Both NH_2-PS and COOH-PS triggered increased ROS levels and reduced cell viability for the concentration investigated in this work (1×10^{12} and 6×10^{12} NPs/mL for NH_2-PS; 6×10^{12} and $1x10^{14}$ NPs/mL for COOH-PS). Only the high concentration conditions of NH_2-PS and COOH-PS also achieved a continuous non-reversible decrease in TEER indicative of a loss in cell monolayer integrity. A systematic analysis of the recorded spectra through artificial intelligence (tSNE) and chemometric (PCA, LDA) analysis confirmed the existence of significant differences in the composition of the medium for the different PS NP conditions. The spectra identified hypoxanthine as a metabolite that is released by Caco-2 cells in response to PS NP exposure and that is particularly high under conditions that result in decreased TEER. These findings identify[172,175] hypoxanthine as a spectral biomarker for PS NP-induced cellular stress in differentiated Caco-

2 cell monolayers. Although the implications of this finding for intestinal membranes will need to be further evaluated in future experiments with systems that are not derived from cancer cells, which may have an altered purine metabolism[170,218,219] , the results underline the usefulness of SERS for monitoring cellular responses to nanoplastics exposure. In addition to providing a sensitive spectroscopic detection modality for the hypoxanthine metabolite, SERS – in combination with chemometric analysis – achieved a spectral "fingerprinting" of the cellular response to the different PS NP conditions. At 18 h, it was possible not only to distinguish the PS NP treated cells from the no treatment controls but also to distinguish different PS NP conditions, which differed in surface chemistry (NH_2, COOH) and concentrations, from each other. Importantly, the SERS spectra for low concentrations of NH_2-PS and COOH-PS could already be reliably distinguished from the no treatment controls after 6 h, indicating PS NP induced metabolomic changes even for the low NP conditions.

The PS NP concentrations required to induce membrane damage within a time window of 18 h investigated in this work are high, and uptake of these concentrations through food and water is unlikely. Our work does, however, not rule out more intricate metabolomic changes in response to low nanoplastics concentrations. It is conceivable that under continuous (i.e. chronic) exposure, these metabolic changes may still achieve a detrimental effect on the intestinal membrane health. The ability to detect PS-NP-induced changes in the metabolism of intestinal cells through SERS measurements of the extracellular medium could be instrumental in detecting and identifying nanoplastics-induced cellular stress and to evaluate the risk associated with nanoplastics.

3.8 Methods

Cell Culture. The human colon carcinoma Caco-2 cell lines was purchased from the American Type Culture Collection (ATCC®, HTB-37TM). The cells were cultured in advanced Minimum Essential medium (MEM) supplemented with 10% fetal bovine serum, 2 mM L-glutamine, 50 units/mL penicillin, and grown in an incubator at 37 °C, 5% CO_2 and 95% relative humidity. The Caco-2 cells were seeded at a density of 1×10^5 cells per well on to transwell polyester membrane cell culture inserts (12 mm diameter, 0.4 μm pore size, Corning®). The culture medium was changed every 3 days. The cells were left to grow and differentiate for 21 days.

Characterization of PS NPs. COOH-PS particles are commercially available from Polysciences (Fluoresbrite ® YG Carbxylate Microspheres, 0.05 μm, λ_{exc}/ λ_{em} =441 nm/ 486 nm). NH_2-PS particles are commercially available from Millipore Sigma (amine-modified polystyrene, fluorescent blue, 0.05 μm, λ_{exc}/ λ_{em} =360 nm/ 420 nm). Both PS NPs were washed with Milli-Q water in centrifugal filter units (Amicon® Ultra-4, 10 kDa) for three times before experiments. Dynamic light scattering (DLS) measurement and zeta potential measurement were performed by Zetasizer Nano ZS90 (Malvern, Worestershire, UK). The hydrodynamic diameter of nanoparticles were measured at concentration of 1×10^{12} particles/ mL in Milli-Q water. Zeta potential of nanoparticles were measured at concertation of 1×10^{12} particles/ mL in 10 mM NaCl (pH 7.0). The reported results represent the mean of 10 independent experiments.

Colloidal Au NP Synthesis. Colloidal gold seeds were prepared by heating 20 mL of $HAuCl_4{\cdot}3H_2O$ (0.26 mM, Sigma-Aldrich, wt 393.83 g), and adding 800 µL of sodium citrate dihydrate (34.00 mM, Sigma-Aldrich, wt 294.10 g) immediately after boiling. The gold seeds were then grown to an average size of 40 nm by adding dropwise 50 ml of $HAuCl_4.3H_2O$ solution (1.00 mM), and 80 mL of a mixture of sodium citrate dihydrate (0.85 mM) and L-Ascorbic acid (2.84 mM, Sigma-Aldrich, wt 176.12 g). The 80 nm gold nanoparticles were obtained by adding 80 ml of mixture prepared above. The gold solution was then boiled for 30 min and neutralized to pH 7.0 with a 10 mM aqueous solution of NaOH (Sigma-Aldrich, wt 40.00 g). Before use, the colloidal gold solution was washed by centrifugation (720g, 10 min) and resuspension in Milli-Q water.

Preparation of SERS Substrate. Aqueous solutions of 80 nm AuNPs ($1\text{x}10^{12}$ /ml, 5 ml) was synthesized and prepared via above method. 5 ml of hexane was added to form the water-hexane interface, then followed by the addition of ethanol drop wisely. The hexane layer on the top was removed, and the Au NP film formed on the water surface was carefully transferred to a glass coverslip. The prepared substrate was placed in the hood overnight to evaporate residual solvent.

Dark-Field Scattering Characterization of SERS Substrate. Scattering images of Au film were recorded using an upright microscope (Olympus BX51 WI). The scattering behavior the sample was characterized with unpolarized white light fitted with an air dark-field condenser in transmission mode. Light scattering from Au film was collected using a 60x objective (NA =0.65). The microscope featured a 303 mm focal length imaging spectrometer (Andor Shamrock) and a back-illuminated CCD detector (DU401-BR-DD). The recorded spectra was corrected by subtracting the background signal originating from an adjacent area, and normalized by divide through the excitation profile of the white light illumination source.

Quantification of PS uptake. Specified concentration of NH_2-PS and COOH-PS was placed into the apical chamber. Cells were incubated with particles at 37 °C and 5% CO_2 for 6h, 18h. Cells were washed twice with PBS and followed by detachment with cell dissociation buffer. The cell suspension were collected and move into a microplate, where the fluorescence intensity was measured at an excitation and an emission wavelength of 350 nm and 420 nm for NH_2-PS, 488 nm and 520 nm for COOH-PS using microplate reader. The number of polystyrene particles being uptaken was calculated from the standard curve of particles and corresponding fluorescent intensity.

Intercellular Particle Distribution. After PS NPs treatment, the cells were fixed with 4% (w/v) PierceTM Formaldehye (ThermoFisher) for 15 min. Subsequently, the cells were incubated with ZO-1 Monoclonal Antibody, Alexa Fluor 647 (10 ug/ml, ThermoFisher), Hoechst 33342 (400 ng/ml, Invitrogen, USA) at room temperature for 1 hour. The cells were washed three times with DPBS after each step of the fixation and labeling procedure to remove excess reagents. Samples were imaged with scanning confocal microscope (Olympus FV 1000) at 405,488 and 647 nm.

Cellular Membrane Imaging. After PS NPs treatment, Caco-2 cells were stained with Calcein-AM (2μM) and EthD-1 (4 μM) for 45 min at room temperature. The cells were imaged in an inverted microscope (Olympus IX71) through a 10x objective, and signal captured on an electron multiplying CCD (EMCCD, Andor Ixon+). The fluorescent signal of live cell was measured at an excitation and an emission wavelength of 473 nm and 510 nm. The fluorescent signal of dead cell was measured at an excitation and an emission wavelength of 580 nm and 620 nm. The exposure time for each monochromatic image was 0.5 s, and the cycle time for a full set of ten images was 5 s.

Cell Viability Measurement. Cell viability was measured by using Vybrant™ MTT Cell Proliferation Assay kit (Invitrogen, V13154). After PS NPs treatment, cell were incubated with MTT working solution (1mM) at 37 °C for 2 hours, and followed with 50 ul of DMSO. The percentage of cell viability change was compared with cell viability from the control group.

ROS Level Measurement. Caco-2 cells were treated with PS NPs for specified concentration and incubation time. Intracellular ROS level was detected using 10 uM of 2', 7' – dichlorofluorescin diacetate (DCFH-DA; Sigma Aldrich, USA) at 37 °C for 45 min. The DCF intensity was measured at an excitation and an emission wavelength of 488 nm and 525 nm. H_2O_2 (200 uM) treated Caco-2 cells were used as positive control. The percentage of ROS level change was compared with ROS level from the no treatment control group.

LDH Level Measurements. LDH leakage was measured from Caco-2 cells by using CyQUANT™ LDH Cytotoxicity Assay kit (Invitrogen, C20300). After PS NPs treatment, 50 ul of cell culture medium from apical compartment were collected and 50 ul of LDH reaction mixture was added. The wells were incubated for 30 min at room temperature, followed by 50 ul stop solution. The absorbance was measured at 490 nm. The percentage of LDH activity change was compared with LDH release from the no treatment control group.

TEER measurements. The trans-epithelial electrical resistance (TEER) of the cell monolayers were measured using the Millicell-ERS Voltammeter (Millipore Sigma). To eliminate the influence of temperature, measures were performed within 2 min after taking the culture plates out of the incubator. Within this time, samples did not show any reading drift. Before measurement, electrodes were equilibrated and sterilized according to the manufacturer's recommendations. Before particle experiment, TEER of the cell monolayer was measured every three days after seeding to assess cell confluency and tight junction functionality. Only cell with an average TEER value 700 Ohms are qualified for further experiments. During particle treatment, TEER were recorded every hour for 24 hr. Three measurements were taken per cell sample. The normalized TEER was calculated by dividing the measurements with TEER value obtained before particle treatment (t=0).

SERS Spectra. 20 µl of cell medium was pipetted onto the SERS substrate. Then a glass coverslip was placed on the top to prevent evaporation of cell medium during the SERS measurement. The spectra were obtained with a Renishaw Raman microscope (model RM-2000) using a 50 x objective. The sample were excited by a diode laser with 785 nm wavelength and an excitation power of 0.7 mW. All spectra were obtained with a 10 s integration time, and 10 spectra were accumulated.

Data Analysis. All data were imported into MatLab (The Mathworks Inc., Natick, MA) and an initial data processing and analysis was performed with the PLS toolbox (Eigenvector Research, Wenatchee, WA). The spectra were baseline corrected using a Whittaker filter (λ=200) and area-normalized (n

= 1). The second derivatives spectra was calculated after a Savitzky-Golay smoothing (filter width ω= 15, polynomial order σ= 2). The obtained second derivative spectra were converted into a barcode spectra using a home-written program. Wavenumbers with a negative second derivative whose absolute value was at least 2.5 standard deviations higher than the noise were assigned a value of 1. All other wavenumbers were assigned a value of 0. The bar code of all the spectra of one condition were added and normalized to generate histograms of the second derivative spectra. t-SNE of the second derivative spectra (no barcoding) was performed with the Matlab t-SNE function. PCA of the second derivative spectra was performed using the Matlab PCA function. The first 20 PCs were used as input for an LDA analysis implemented as described by Chen and Hsu in Matla.[220] Spectral peak areas were obtained from baseline- and area-corrected spectra through fitting of Lorentzian peak function $y = y_0 + \frac{2A}{\pi}\frac{\omega}{4(x-x_c)^2+\omega^2}$ (A= area, ω= width, xc= spectral peak).

References

(1) Vincenzo, A.; Pilot, R.; Frasconi, M.; Marago, O. M.; Lati, M. A. Surface plasmon resonance in gold nanoparticles: a review*. Journal of Physics: Condensed Matter* 2017, *29*, 203002.

(2) Willets, K. A.; Van Duyne, R. P. Localized surface plasmon resonance spectroscopy and sensing. *Annual Review of Physical Chemistry* 2007, *58*: 267-97.

(3) Lerch, S.; Reinhard, B. M. Spectral signatures of charge transfer in assemblies of molecularly-linked plasmonic nanoparticles. *International Journal of Modern Physics B* 2017, *31*, 1740002.

(4) Wu, L.; Rinhard, B.M. Probing subdiffraction limit separations with plasmon coupling microscopy: concepts and applications. *Chemical Society Reviews* 2014, *43*, 3884.

(5) Yan, B.; Boriskina, S. V.; Reinhard, B. M. Optimizing gold nanoparticle cluster configurations ($n \leq 7$) for array applications. *Journal of Physical Chemistry C* 2011, *115*, 4578–4583.

(6) Yan, B.; Boriskina, S. V.; Reinhard, B. M. Design and implementation of noble metal nanoparticle cluster arrays for plasmon enhanced biosensing. *Journal of Physical Chemistry C* 2011, *115*, 24437-24453.

(7) Yang, L.; Yan, B.; Premasiri, W. R.; Ziegler, L. D.; Dal Negro, L.; Reinhard, B. M. Engineering nanoparticle cluster arrays for bacterial biosensing: the role of the building block in multiscale SERS substrates. *Advanced Functional Materials* 2010, *20*, 2619–2628.

(8) Yan, B.; Thubagere, A.; Premasiri, W. R.; Ziegler, L. D.; Dal Negro, L.; Reinhard, B. M. Engineered SERS substrates with multiscale signal enhancement: nanoparticle cluster arrays. *ACS Nano* 2009, *3*, 1190–1202.

(9) Reinhard, B.M; Siu, M.; Agarwal, H.; Alivisatos, A. P.; Liphardt, J. Calibration of dynamic molecular rulers based on plasmon coupling between gold nanoparticles. *Nano Letter* 2005, *11*, 2246-2252.

(10) Sonnichsen, C.; Reinhard, B. M. Liphardt, J. Alivisatos, A. P. A molecular ruler based on plasmon coupling of single gold and silver nanoparticles. *Nature Biotechnology* 2005, *23*, 741-745.

(11) Deeb, C.; Zhou, X.; Plain, J.; Wiederrecht, G. P.; Bachelot, R. Size dependence of the plasmonic near-field measured via single-nanoparticle photoimaging. *Journal of Physical Chemistry C* 2013, *117*, 10669-10676.

(12) Schlucker, S. SERS microscopy: Nanoparticle probes and biomedical applications. *ChemPhysChem* 2009, *10*, 1344-1354.

(13) Amendola, V.; Meneghetti, M. Exploring how to increase the brightness of surface-enhanced Raman spectroscopy nanolabels: the effect of the Raman-active molecules and of the label size. *Advanced Functional Materials* 2012, *22*, 353-360.

(14) Schwartzberg, A. M.; Grant, C. D.; Wolcott, A.; Talley, C. E.; Huser, T. R.; Bogomolni, R.; Zhang, J. Z. Unique gold nanoparticle aggregates as a highly active surface-enhanced raman scattering substrate. *Journal of Physical Chemistry B* 2004, *108*, 19191-19197.

(15) Kim, N.; Thoma, M.R.; Bergholt, M. S.; Pence, I. J.; Seong, H.; Charchar, P.; Todorova, N.; Nagelkerke, A.; Belessiotis-Richards, A.; Payne, D. J.; Gelmi, A.; Yarovasky, I.; Stevens, M. M. Surface enhanced Raman scattering artificial nose for high dimensionality fingerprinting. *Nature Commun*ication 2020, *11*, 207.

(16) Ye, Q., Fang, J. & Sun, L. Surface-enhanced Raman scattering from functionalized self-assembled monolayers. 2. Distance dependence of enhanced Raman scattering from an azobenzene terminal group. *Journal of Physical Chemistry B* 1997, *101*, 8221–8224.

(17) Ye, J. *et al*. Excitation wavelength dependent surface enhanced Raman scattering of 4-aminothiophenol on gold nanorings. *Nanoscale* 2012, *4*, 1606–1611.

(18) Rana, S.; Bajaj, A.; Mout, R.; Rotello, V. M. Monolayer coated gold nanoparticles for delivery applications. *Advanced Drug Delivery Reviews* 2012, *64*, 200-216.

(19) Khan, A. K.; Rashi, R.; Murtaza, G.; Zahra, A. Gold Nanoparticles: Synthesis and Applications in Drug Delivery. *Tropical Journal of Pharmaceutical Res*earch 2014, *13*, 7, 1169.

(20) Ghosh, P.; Han, G.; De, M.; Kim, C. K.; Rotello, V. M. Gold nanoparticles in delivery applications. *Advanced Drug Delivery Reviews* 2008, *60*, 1307-1315.

(21) Friedman, A.D.; Claypool, S.E.; Liu, R. The smart targeting of nanoparticles. *Current Pharmaceutical Design* 2013, *19*, 6315-6329.

(22) Zhang, Q.; Reinhard, B. M. Ligand density and nanoparticle clustering cooperate in the multivalent amplification of epidermal growth factor receptor activation. *ACS Nano* 2018, 12, *10*, 10473-10485.

(23) Lemmon, M. A.; Schlessinger, J. Cell Signaling by Receptor Tyrosine Kinases. *Cell* 2010, *141*, 1117-1134.

(24) Schlessinger, J. Ligand-Induced, Receptor-Mediated Dimerization and Activation of EGF Receptor. *Cell* 2002, *110*, 669-672.

(25) Schlessinger, J. Cell Signaling by Receptor Tyrosine Kinases. *Cell* 2000, 103, 211-225.

(26) Yarden, Y.; Schlessinger, J. Self-Phosphorylation of Epidermal Growth Factor Receptor: Evidence for a Model of Intermolecular Allosteric Activation. *Biochemistry* 1987, *26*, 1434-1442.

(27) Ladbury, J. E.; Arold, S. T. Noise in Cellular Signaling Pathways: Causes and Effects. *Trends in Biochemical Sciences* 2012, *37*, 173-178.

(28) Wu, H. Higher-Order Assemblies in a New Paradigm of Signal Transduction. *Cell* 2013, *153*, 287-292.

(29) Ichinose, J.; Murata, M.; Yanagida, T.; Sako, Y. EGF Signaling Amplification Induced by Dynamic Clustering of EGFR. *Biochemical and Biophysical Research Communications* 2004, *3*, 1143-1149.

(30) Sawano, A.; Takayama, S.; Matsuda, M.; Miyawaki, A. Lateral Propagation of EGF Signaling after Local Stimulation Is Dependent on Receptor Density. *Developmental Cell* 2002, *3*, 245-257.

(31) Reynolds, A. R.; Tischer, C.; Verveer, P. J.; Rocks, O.; Bastiaens, P. I. H. EGFR Activation Coupled to Inhibition of Tyrosine Phosphatases Causes Lateral Signal Propagation. *Nature Cell Biology* 2003, *5*, 447-453.

(32) Verveer, P. J.; Wouters, F. S.; Reynolds, A. R.; Bastiaens, P. I. H. Quantitative Imaging of Lateral ErbB1 Receptor Signal Propagation in the Plasma Membrane. *Science* 2000, *290*, 1567-1570.

(33) Ichinose, J.; Murata, M.; Yanagida, T.; Sako, Y. EGF Signaling Amplification Induced by Dynamic Clustering of EGFR. *Biochemical and Biophysical Research Communications* 2004, *324*, 1143-1149.

(34) Nakase, I.; Ueno, N.; Katayama, M.; Noguchi, K.; Takatani-Nakase, T.; Kobayashi, N. B.; Yoshida, T.; Fujii, I.; Futaki, S. Receptor Clustering and Activation by Multivalent Interaction through Recognition Peptides Presented on Exosomes. *Chemical Communications* 2017, *53*, 317-320.

(35) Huskens, J.; Prins, L. J.; Haag, R.; Ravoo, B. J. Multivalency: Concepts, Research & Applications; *Wiley and Sons: Hoboken*, 2018.

(36) Mammen, M.; Choi, S.-K.; Whitesides, G. M. Polyvalent Interactions in Biological Systems: Implications for Design and Use of Multivalent Ligands and Inhibitors. *Angewandte Chemie International Edition* 1998, *37*, 2754-2794.

(37) Jiang, W.; Kim, B. Y. S.; Rutaka, J. T.; Chan, W. C. Nanoparticle-Mediated Cellular Response Is Size-Dependent. *Nature Nanotechnology* 2008*, 3*, 145-150.

(38) Vance, D.; Shah, M.; Joshi, A.; Kane, R. S. Polyvalency: A Promising Strategy for Drug Design. *Biotechnology and Bioengineering* 2008, *101*, 429-434.

(39) Hong, S.; Leroueil, P. R.; Majoros, I. J.; Orr, B. G.; Baker Jr., J. R.; Banaszak Joll, M. M. The Binding Avidity of a Nanoparticle-Based Multivalent Targeted Drug Delivery Platform. *Chemical Biology* 2007, *14*, 107-115.

(40) Poon, Z.; Chen, S.; Engler, A. C.; Lee, H. I.; Atas, E.; von Maltzahn, G.; Bhatia, S. N.; Hammond, P. T. Ligand-Clustered "Patchy" Nanoparticles for Modulated Cellular Uptake and *in Vivo* Tumor Targeting. *Angewandte Chemie International Edition* 2010, *49*, 7266-7270.

(41) Chithrani, B. D.; Ghazani, A. A.; Chan, W. C. W. Determining the Size and Shape Dependence of Gold Nanoparticle Uptake into Mammalian Cells. *Nano Letter* 2006, *6*, 662-668.

(42) Dalal, C.; Saha, A.; Jana, N. R. Nanoparticle Multivalency Directed Shifting of Cellular Uptake Mechanism. *Journal of Physical Chemistry C* 2016, *120*, 6778-6786.

(43) Weissleder, R.; Kelly, K.; Sun, E. Y.; Shtaland, T.; Josephson, L. Cell-Specific Targeting of Nanoparticles by Multivalent Attachment of Small Molecules. *Nature Biotechnology* 2005, *23*, 1418-1423.

(44) Wang, J.; Tian, S.; Petros, R.; Napier, M. E.; DeSimone, J. M. The Complex Role of Multivalency in Nanoparticles Targeting the Transferrin Receptor for Cancer Therapies. *Journal of American Chemical Society* 2010, *132*, 11306-11313.

(45) Singhai, A.; Wakefield, D. L.; Bryant, K. L.; Hammes, S. R.; Holowka, D.; Baird, B. Spatially Defined EGF Receptor Activation Reveals an F-Actin-Dependent Phospho-Erk Signaling Complex. *Biophysical Journal* 2014, *107*, 2639-2651.

(46) Stabley, D.; Retterer, S.; Marshall, S.; Salaita, K. Manipulating the Lateral Diffusion of Surface-Anchored EGF Demonstrates That Receptor Clustering Modulates Phosphorylation Levels. *Integrative Biology* 2013, *5*, 659.

(47) Greish, K. Enhanced Permeability and Retention (EPR) Effect for Anticancer Nanomedicine Drug Targeting. *Methods in Molecular Biology* 2010, *624*, 25-37.

(48) Prabhakar, U.; Maeda, H.; Jain, R. K.; Sevick-Muraca, E. M.; Zamboni, W.; Farokhzad, O. C.; Barry, S. T.; Gabizon, A.; Gradzinski, P.; Blakey, D. C. Challenges and Key Considerations of the Enhanced Permeability and Retention Effect for Nanomedicine Drug Delivery in Oncology. *Cancer Research* 2013, *73*, 1-6.

(49) Clayton, A. H. A.; Tavarnesi, M. L.; Johns, T. G. Unligated Epidermal Growth Factor Receptor Forms Higher Order Oligomers within Microclusters on A431 Cells That Are Sensitive to Tyrosine Kinase Inhibitor Binding. *Biochemistry* 2007, *46*, 4589-4597.

(50) Huang, Y.; Bharill, S.; Karandur, D.; Peterson, S. M.; Marita, M.; Shi, X.; Kaliszewski, M. J.; Smith, A. W.; Isacoff, E. Y.; Kuriyan, J. Molecular Basis for Multimerization in The Activation of The Epidermal Growth Factor Receptor. *eLife* 2016, *5*, e14107.

(51) Abulrob, A.; Lu, Z.; Baumann, E.; Vobornik, D.; Taylor, R.; Stanimirovic, D.; Johnston, L. J. Nanoscale Imaging of Epidermal Growth Factor Receptor Clustering. *Journal of Biological Chemistry* 2010, *285*, 3145-3156.

(52) Needham, S. R.; Roberts, S. K.; Arkhipov, A.; Mysore, V. P.; Tynan, C. J.; Zanetti-Domingues, L. C.; Kim, E. T.; Losasso, V.; Korovesis, D.; Hirsch, M.; Rolfe, D. J.; Parker, P. J.; Shan, Y.; Shaw, D.E.; Martin-Fernandez, M.L. EGFR Oligomerization Organizes Kinase-Active Dimers into Competent Signaling Platforms. *Nature Communication* 2016, *7*, 13307.

(53) van Lengerich, B.; Agnew, C.; Puchner, E. M.; Huang, B.; Jura, N. EGF and NRG Induce Phosphorylation of HER3/ERBB3 by EGFR Using Distinct Oligomeric Mechanisms. *Proceedings of the National Academy of Sciences* 2017, *114*, E2836-E2845.

(54) Ibach, J.; Radon, Y.; Gelleri, M.; Sonntag, M. H.; Brunsveld, L.; Bastiaens, P. I.; Verveer, P. J. Single Particle Tracking Reveals That EGFR Signaling Activity Is Amplified in Clathrin-Coated Pits. *PLoS One* 2015, *10*, e0143162.

(55) Baranov, V. I.; Quinn, Z.; Bandura, D. R.; Tanner, S. D. A Sensitive and Quantitative Element-Tagged Immunoassay with ICPMS Detection. *Analytical Chemistry* 2002, 74, 1629-1636.

(56) Schultz, S.; Smith, D. R.; Mock, J. J.; Schultz, D. A. Single-Target Molecule Detection with Nonbleaching Multicolor Optical Immunolabels. *Proceedings of the National Academy of Sciences* 2000, *97*, 996-1001.

(57) Huang, T.; Nallathamby, P. D.; Gillet, D.; Xu, X.-H. N. Design and Synthesis of Single-Nanoparticle Optical Biosensors for Imaging and Characterization of Single Receptor Molecules on Single Living Cells. *Analytical Chemistry* 2007, *79*, 7708-7718.

(58) El-Sayed, M. A. Some Interesting Properties of Metals Confined in Time and Nanometer Space of Different Shapes. *Accounts of Chemical Research* 2001, *34*, 257-264.

(59) Wu, L.; Reinhard, B. M. Probing Subdiffraction Limit Separations with Plasmon Coupling Microscopy: Concepts and Applications. *Chemical Society Reviews* 2014, 3884-3897.

(60) Willets, K. A.; Van Duyne, R. P. Localized Surface Plasmon Resonance Spectroscopy and Sensing. *Annual Review of Physical Chem*istry 2007, *58*, 267-297.

(61) Kreibig, U.; Vollmer, M. Optical Properties of Metal Clusters; *Springer: Berlin,* 1995.

(62) Yan, B.; Boriskina, S. V.; Reinhard, B. M. Optimizing Gold Nanoparticle Cluster Configurations (n </= 7) for Array Applications. *Journal of Physical Chemistry C* 2011, *115*, 4578-4583.

(63) Reinhard, B. M.; Siu, M.; Agarwal, H.; Alivisatos, A. P.; Liphardt, J. Calibration of Dynamic Molecular Rule Based on Plasmon Coupling between Gold Nanoparticles. *Nano Letter* 2005, *5*, 2246 - 2252.

(64) Wei, Q. H.; Su, K. H.; Durant, S.; Zhang, X. Plasmon Resonance of Finite One-Dimensional Au Nanoparticle Chains. *Nano Letter* 2004, *4*, 1067-1071.

(65) Maier, S. A.; Brongersma, M. L.; Kik, P. G.; Atwater, H. A. Observation of Near-Field Coupling in Metal Nanoparticle Chains Using Far-Field Polarization Spectroscopy. *Physical Review B* 2002, *65*, 193408.

(66) Rechberger, W.; Hohenau, A.; Leitner, A.; Krenn, J. R.; Lamprecht, B.; Aussenegg, F. R. Optical Properties of Two Interacting Gold Nanoparticles. *Optics Communications* 2003, *220*, 137-141.

(67) Chen, J. I. L.; Chen, Y.; Ginger, D. S. Plasmonic Nanoparticle Dimers for Optical Sensing of DNA in Complex Media. *Journal of the American Chemical Society* 2010, *132*, 9600-9601.

(68) Rong, G.; Wang, H.; Skewis, L. R.; Reinhard, B. M. Resolving Subdiffraction Limit Encounters in Nanoparticle Tacking Using Live Cell Plasmon Coupling Microscopy. *Nano Letter* 2008, *8*, 3386 - 3393.

(69) Wang, J.; Boriskina, S. V.; Wang, H.; Reinhard, B. M. Illuminating Epidermal Growth Factor Receptor Densities on Filopodia through Plasmon Coupling. *ACS Nano* 2011, *5*, 6619.

(70) Wang, J.; Yu, X.; Boriskina, S. V.; Reinhard, B. M. Quantification of Differential ErbB1 and ErbB2 Cell Surface Expression and Spatial Nanoclustering through Plasmon Coupling. *Nano Letter* 2012, *12*, 3231-3237.

(71) Yu, X.; Wang, J.; Feizpour, A.; Reinhard, B. M. Illuminating The Lateral Organization of Cell-Surface CD24 and CD44 through Plasmon Coupling between Au Nanoparticle Immunolabels. *Analytical Chemistry* 2013, *85*, 1290-1294.

(72) Aaron, J.; Travis, K.; Harrison, N.; Sokolov, K. Dynamic Imaging of Molecular Assemblies in Live Cells Based on Nanoparticle Plasmon Resonance Coupling. *Nano Letter* 2009, *9*, 3612-3618.

(73) Crow, M. J.; Seekell, K.; Ostrander, J. H.; Wax, A. Monitoring of Receptor Dimerization Using Plasmonic Coupling of Gold Nanoparticles. *ACS Nano* 2011, 5, 8532-8540.

(74) Zhang, P.; Lee, S.; Yu, H.; Fang, N.; Ho Kang, S. Super-Resolution of Fluorescence-Free Plasmonic Nanoparticles Using Enhanced Dark-Field Illumination Based on Wavelength Modulation. *Scientific Reports* 2015, *5*, 11447.

(75) Gu, Y.; Di, X.; Sun, W.; Wang, G.; Fang, N. Three-Dimensional Super Localization and Tracking of Single Gold Nanoparticles in Cells. *Analytical Chemistry* 2012, *84*, 4111-4117.

(76) Gu, Y.; Wang, G.; Fang, N. Simultaneous Single-Particle Superlocalization and Rotational Tracking. *ACS Nano* 2013, 7, 1658-1665.

(77) Lu, H. S.; Chai, J. J.; Li, M.; Juang, B. R.; He, C. H.; Bi, R. C. Crystal Structure of Human Epidermal Growth Factor and Its Dimerization. *Journal of Biological Chemistry* 2001, *276*, 34913-34917.

(78) Xu, F.; Reiser, M.; Yu, X.; Gummuluru, S.; Wetzler, L.; Reinhard, B. M. Lipid Mediated Targeting with Membrane-Wrapped Nanoparticles in the Presence of Corona Formation. *ACS Nano* 2015, *10*, 1189-1200.

(79) Torrano, A. A.; Pereira, A. S.; Oliveira, O. N.; Barros-Timmons, A. Probing the Interactions of Oppositely Charged Gold Nanoparticles with DPPG and DPPC Langmuir Monolayers as Cell Membrane Models. *Colloids Surfaces B* 2013, *108*, 120-126.

(80) van Schooneveld, M. M.; Vucic, E.; Koole, R.; Zhou, Y.; Stocks, J.; Cormode, D. P.; Tang, C. Y.; Gordon, R. E.; Nicolay, K.; Meijerink, A.; Fayad, Z. A.; Mulder, W. J. Improved Biocompatibility and Pharmacokinetics of Silica Nanoparticles by Means of a Lipid Coating: a Multimodality Investigation. *Nano Letter* 2008, *8*, 2517-1525.

(81) Estephan, Z. G.; Schlenoff, P. S.; Schlenoff, J. B. Zwitterion as an Alternative to PEGylation. *Langmuir* 2011, *27*, 6794 - 6800.

(82) Landis, R. F.; Tang, R.; Hou, S.; Yazdani, M.; Lee, Y.; Rotello, V. M. Zwitterionic Ligands Bound to CdSe/ZnS Quantum Dots Prevent Adhesion to Mammalian Cells. *Phosphorus, Sulfur and Silicon and the Related Elements* 2015, *190*, 2302-2306.

(83) Yu, X.; Xu, F.; Ramirez, N-G. P.; Kijewski, S. D. G.; Akiyama, H.; Gummuluru, S.; Reinhard, B. M. Dressing up Nanoparticles: A Membrane Wrap to Induce Formation of the Virological Synapse. *ACS Nano* 2015, *9*, 4182-4192.

(84) Yu, X.; Feizpour, A.; Ramirez, N.-G. P.; Wu, L.; Akiyama, H.; Yu, X.; Gummuluru, S.; Reinhard, B. M. Glycosphingolipid-Functionalized Nanoparticles Recapitulate CD169-Dependent HIV-1 Uptake and Trafficking in Dendritic Cells. *Nature Communication* 2014, *5*, 4136.

(85) Kolb, H. C.; Finn, M. G.; Sharpless, K. B. Click Chemistry: Diverse Chemical Function from a Few Good Reactions. *Angewandte Chemie International Edition* 2001, *40*, 2004-2021.

(86) Hedden, R. C.; Bauer, B. J. Structure and Dimensions of PAMAM/PEG Dendrimer-Star Polymers. *Macromolecules* 2003, *36*, 1829-1835.

(87) Stan, G.; DelRio, F. W.; MacCuspie, R. I.; Cook, R. F. Nanomechanical Properties of Polyethylene Glycol Brushes on Gold Substrates. *Journal of Physical Chemistry B* 2012, *116*, 3138-3147.

(88) Kratky, O.; Porod, G. Röntgenuntersuchung gelöster Fadenmoleküle. *Recueil des Travaux Chimiques des Pays-Bas* 1949, *68*, 1106-1122.

(89) Liese, S.; Netz, R. R. Influence of Length and Fleibility of Spacers on Binding Affinity of Divalent Ligands. *The Journal of Organic Chemistry* 2015, *11*, 804-816.

(90) Martinez-Veracoechea, F. J.; Leunissen, M. E. The Entropic Impact of Tethering, Multivalency and Dynamic Recruitment in Systems with Specific Binding Groups. *Soft Matter* 2013, *9*, 3213-3219.

(91) Moore, N. W.; Kuhl, T. L. The Role of Flexible Tethers in Multiple Ligand-Receptor Bond Formation between Curved Surfaces. *Biophysical Journal* 2006, *91*, 1675-1687.

(92) Hyatt, D. C.; Ceresa, B. P. Cellular Localization of the Activated EGFR Determines Its Effect on Cell Growth in MDA-MB-468 Cells. *Experimental Cell Research* 2008, *314*, 3415-3425.

(93) Villasenor, R.; Nonaka, H.; Del Conte-Zerial, P.; Kalaidzidis, Y.; Zerial, M. Regulation of EGFR Signal Transduction by Analogue to Digital Conversion in Endosomes. *eLife* 2015, *4*, e06156.

(94) Offterdinger, M.; Bastiaens, P. I. Prolonged EGFR Signaling by ERBB2-Mediated Sequestration at the Plasma Membrane. *Traffic* 2008, *9*, 147-155.

(95) Hennig, R.; Pollinger, K.; Veser, A.; Breunig, M.; Goepferich, A. Nanoparticle Multivalency Counterbalances the Ligand Affinity Loss Upon PEGylation. *Journal of Controlled Release* 2014, *194*, 20-27.

(96) Elias, D. R.; Poloukhtine, A.; Popik, V.; Tsourkas, A. Effect of Ligand Density, Receptor Density, and Nanoparticle Size on Cell Targeting. *Nanomedicine* 2013, *9*, 194-201.

(97) Hakem, I. F.; Leech, A. M.; Johnson, J. D.; Donahue, S. J.; Walker, J. P.; Bockstaller, M. R. Understanding Ligand Distributions in Modified

Particle and Particlelike Systems. *Journal of the American Chemical Society* 2010, *132*, 16593-16598.

(98) Liu, J.; Weller, G. E.; Zern, B.; Ayyaswamy, P. S.; Eckmann, D. M.; Muzykantov, V. R.; Radhakrishnan, R. Computational Model for Nanocarrier Binding to Endothelium Validated Using in Vivo, in Vitro, and Atomic Force Microscopy Experiments. *Proceedings of the National Academy of Sciences* 2010, *107*, 16530-16535.

(99) Zhou, Y.; Drummond, D. C.; Zou, H.; Hayes, M. E.; Adams, G. P.; Kirpotin, D. B.; Marks, J. D. Impact of Single-Chain Fv Antibody Fragment Affinity on Nanoparticle Targeting of Epidermal Growth Factor Receptor-Expressing Tumor Cells. *Journal of Molecular Biology* 2007, *371*, 934-947

(100) Kusumi, A.; Nakada, C.; Ritchie, K.; Murase, K.; Suzuki, K.; Murakoshi, H.; Kasai, R. S.; Kondo, J.; Fujiwara, T. Paradigm Shift of the Plasma Membrane Concept from the Two-Dimensional Continuum Fluid to the Partitioned Fluid: High-Speed Single-Molecule Tracking of Membrane Molecules. *Annual Review of Biophysics and Bimolecular Structure* 2005, *34*, 351-378.

(101) Bethani, I.; Skanland, S. S.; Dikic, I.; Acker-Palmer, A. Spatial Organization of Transmembrane Receptor Signaling. *The EMBO Journal* 2010, *29*, 2677-2688.

(102) Manders, E. M. M.; Verbeek, F. J.; Aten, J. A. Measurement of Co-localization of Objects in Dual-Colour Confocal Images. *Journal of Microscopy* 1993, *169*, 357-382.

(103) Dunn, K. W.; Kamocka, M. M.; McDonald, J. H. A Practical Guide to Evaluating Colocalization in Biological Microscopy. *American Journal of Physiology* 2011, *300*, C723-742.

(104) Lemmon, M. A.; Freed, D. M.; Schlessinger, J.; Kiyatkin, A. The Dark Side of Cell Signaling: Positive Roles for Negative Regulators. *Cell* 2016, *164*, 1172-1184.

(105) Ostman, A.; Bohmer, F. D. Regulation of Receptor Tyrosine Kinase Signaling by Protein Tyrosine Phosphatases. *Trends in Cell Biology* 2011, *11*, 258-266.

(106) Nordlander, P.; Oubre, C.; Prodan, E.; Li, K.; Stockman, M. I. Plasmon Hybridization in Nanoparticle Dimers. *Nano Letter* 2004, *4*, 899-903.

(107) Care, B. R.; Soula, H. A. Impact of Receptor Clustering on Ligand Binding. *BMC Systems Biology* 2011, *5*, 48.

(108) Mugler, A.; Bailey, A. G.; Takahashi, K.; ten Wolde, P. R. Membrane Clustering and the Role of Rebinding in Biochemical Signaling. *Biophysical Journal* 2012, *102*, 1069-1078.

(109) DeYulia, G. J., Jr.; Carcamo, J. M.; Borquez-Ojeda, O.; Shelton, C. C.; Golde, D. W. Hydrogen Peroxide Generated Extracellularly by Receptor-Ligand Interaction Facilitates Cell Signaling. *Proceedings of the National Academy of Sciences* 2005, *102*, 5044-5049.

(110) Truong, T. H.; Carroll, K. S. Redox Regulation of Protein Kinases. *Critical Reviews in Biochemistry and Molecular Biology* 2013, *48*, 332-356.

(111) Schindelin, J.; Arganda-Carreras, I.; Frise, E.; Kaynig, V.; Longair, M.; Pietzsch, T.; Preibisch, S.; Rueden, C.; Saalfeld, S.; Schmid, B.; Tinevez, J. Y.; White, D. J.; Hartenstein, V.; Eliceiri, K.; Tomancak, P.; Cardona, A. Fiji: An Open-Source Platform for Biological-Image Analysis. *Nature Methods* 2012, *9*, 676-682.

(112) Costes, S. V.; Daelemans, D.; Cho, E. H.; Dobbin, Z.; Pavlakis, G.; Lockett, S. Automatic and Quantitative Measurement of Protein-Protein Colocalization in Live Cells. *Biophysical Journal* 2004, *86*, 3993-4003.

(113) https://www.plasticseurope.org/en/resources/market-data.

(114) Shah, A. A.; Hasan, F.; Hameed, A.; Ahmed, S. Biological Degradation of Plastics: A Comprehensive Review. *Biotechnology Advances* 2008, *26*, 246-265.

(115) Frias, J. P. G. L.; Nash, R. Microplastics: Finding A Consensus on The Definition. *Marine Pollution Bulletin* 2019, *138*, 145-147.

(116) Thompson, R. C.; Olsen, Y.; Mitchell, R. P.; Davis, A.; Rowland, S. J.; John, A. W.; McGonigle, D.; Russel, A. E. Lost At Sea: Where Is All The Plastic? *Science* 2004, *304*, 838.

(117) Doyle, M. J.; Watson, W.; Bowlin, N. M.; Sheavly, S. B. Plastic Particles in Coastal Pelagic Ecosystems of The Northeast Pacific Ocean. *Marine Environmental Research* 2011, *71*, 41-52.

(118) Martins, J.; Sobral, P. Plastic Marine Debris On The Portuguese Coastline: A Matter of Size? *Marine Pollution Bulletin* 2011, *62*, 2649-2653.

(119) Desai, M. P.; Labhasetwar, V.; Amidon, G. L.; Levy, R. J. Gastrointestinal Uptake of Biodegradable Microparticles: Effect of Particle Size. *Pharmaceutical Research* 1996, *13*, 1838-1845.

(120) Frohlich, E.; Roblegg, E. Models for Oral Uptake of Nanoparticles in Consumer Products. *Toxicology* 2012, *291*, 10-17.

(121) Hillyer, J. F.; Albrecht, R. M. Gastrointestinal Persorption and Tissue Distribution of Differently Sized Colloidal Gold Nanoparticles. *Journal of Pharmaceutical Sciences* 2001, *90*, 1927-1936.

(122) Verma, A.; Stellacci, F. Effect of Surface Properties on Nanoparticle-Cell Interactions. *Small* 2010, *6*, 12-21.

(123) Septiadi, D.; Crippa, F.; Moore, T. L.; Rothen-Rutishauser, B.; Petri-Fink, A. Nanoparticle-Cell Interaction: A Cell Mechanics Perspective. *Advacned Materials* 2018, *30*, 1704463.

(124) Naasz, S.; Altenburger, R.; Kuhnel, D. Environmental Mixtures Of Nanomaterials And Chemicals: The Trojan-Horse Phenomenon and Its Relevance for Ecotoxicity. *Science of the Total Environment* 2018, *635*, 1170-1181.

(125) Borm, P. J. A. Particle Toxicology: From Coal Mining to Nanotechnology. *Inhalation Toxicology* 2002, *14*, 311-324.

(126) Balbus, J. M.; Maynard, A. D.; Colvin, V. L.; Castranova, V.; Daston, G. P.; Denison, R. A.; Dreher, K. L.; Goering, P. L.; Goldberg, A. M.; Kulinowski, K. M.; Monteiro-Riviere, N. A.; Oberdorster, G.; Omenn, G. S.; Pinkerton, K. E.; Ramos, K. S.; Rest, K. M.; Sass, J. B.; Silbergeld, E. K.;

Wong, B. A. Meeting Report: Hazard Assessment for Nanoparticles--Report from An Interdisciplinary Workshop. *Environmental Health Perspectives* 2007, *115*, 1654-1659.

(127) Lewinski, N.; Colvin, V.; Drezek, R. Cytotoxicity of Nanoparticles. *Small* 2008, *4*, 26-49.

(128) Park, M. V. D. Z.; Neigh, A. M.; Vermeulen, J. P.; de la Fonteyne, L. J. J.; Verharen, H. W.; Briede, J. J.; van Loveren, H.; de Jong, W. H. The Effect of Particle Size on The Cytotoxicity, Inflammation, Developmental Toxicity and Genotoxicity of Silver Nanoparticles. *Biomaterials* 2011, *32*, 9810-9817.

(129) Manke, A.; Wang, L.; Rojanasakul, Y. Mechanisms of Nanoparticle-Induced Oxidative Stress and Toxicity. *Biomed Research International* 2013, *2013*, 942916.

(130) Bouwmeester, H.; van der Zande, M.; Jepson, M. A. Effects of Food-Borne Nanomaterials on Gastrointestinal Tissues And Microbiota. *WIREs Nanomedicine and Nanobiotechnology* 2018, 10:e1481.

(131) Lehner, R.; Weder, C.; Petri-Fink, A.; Rothen-Rutishauser, B. Emergence of Nanoplastic in The Environment And Possible Impact on Human Health. *Environmental Science and Technology* 2019, *53*, 1748-1765.

(132) Lambert, S.; Wagner, M. Formation of Microscopic Particles during The Degradation of Different Polymers. *Chemosphere* 2016, *161*, 510-517.

(133) Ward, J. E.; Kach, D. J. Marine Aggregates Facilitate Ingestion of Nanoparticles by Suspension-Feeding Bivalves. *Marine Environmental Research* 2009, *68*, 137-142.

(134) Bhattacharya, P.; Lin, S.; Turner, J. P.; Ke, P. C. Physical Adsorption of Charged Plastic Nanoparticles Affects Algal Photosynthesis. *Journal of Physical Chemistry C* 2010, *114*, 16556-16561.

(135) Besseling, E.; Wang, B.; Lurling, M.; Koelmans, A. A. Nanoplastic Affects Growth of *S. Obliquus* And Reproduction of *D. Magna*. *Environmental Science and Technology.* 2014, *48*, 12336-12343.

(136) Alvarez-Roman, R.; Naik, A.; Kalia, Y. N.; Guy, R. H.; Fessi, H. Skin Penetration And Distribution of Polymeric Nanoparticles. *Journal of Controlled Release* 2004, *99*, 53-62.

(137) Grafmueller, S.; Manser, P.; Diener, L.; Diener, P. A.; Maeder-Althaus, X.; Maurizi, L.; Jochum, W.; Krug, H. F.; Buerki-Thurnherr, T.; von Mandach, U.; Wick, P. Bidirectional Transfer Study of Polystyrene Nanoparticles across The Placental Barrier in An *ex Vivo* Human Placental Perfusion Model. *Environmental Health Perspectives* 2015, *123*, 1280-1286.

(138) Yang, C.-S.; Chang, C.-H.; Tsai, P.-J.; Chen, W.-Y.; Tseng, F.-G.; Lo, L.-W. Nanoparticle-Based in Vivo Investigation on Blood-Brain Barrier Permeability Following Ischemia And Reperfusion. *Analytical Chemistry* 2004, *76*, 4465-4471.

(139) Elamin, E.; Jonkers, D.; Juuti-Uusitalo, K.; van Ijzendoorn, S.; Troost, F.; Duimel, H.; Broers, J.; Verheyen, F.; Dekker, J.; Masclee, A. Effects of Ethanol And Acetaldehyde on Tight Junction Integrity: *in Vitro* Study in A Three Dimensional Intestinal Epithelial Cell Culture Model. *PLos One* 2012, *7*, e35008.

(140) Elamin, E.; Masclee, A.; Juuti-Uusitalo, K.; van Ijzendoorn, S.; Troost, F.; Pieters, H.-J.; Dekker, J.; Jonkers, D. Fatty Acid Ethyl Esters Induce Intestinal Epithelial Barrier Dysfunction via A Reactive Oxygen Species-Dependent Mechanism in A Three-Dimensional Cell Culture Model. *PLoS One* 2013, *8*, e58561.

(141) Garcia-Castillo, M. D.; Chinnapen, D. J.-F.; Lencer, W. I. Membrane Transport across Polarized Epithelia. *Cold Spring Harbor Perspective in Biology* 2017, *9*, a027912.

(142) Fowler, R.; Vllasaliu, D.; Trillo, F. F.; Garnett, M. C.; Alexander, C.; Horsley, H.; Smith, B.; Whitcombe, I.; Eaton, M.; Stolnik, S. Nanoparticle Transport in Epithelial Cells: Pathway Switching through Bioconjugation. *Small* 2013, *9*, 3282-3294.

(143) Pridgen, E. M.; Alexis, F.; Kuo, T. T.; Levvy-Nissenbaum, E.; Karnik, R.; Blumberg, R. S.; Langer, R.; Farokhzad, O. C. Transepithelial Transport of Fc-Targeted Nanoparticles by The Neonatal Fc Receptor for Oral Delivery. *Science Translational Medicine* 2013, *5*, 213ra167.

(144) Yun, Y.; Cho, Y. W.; Park, K. Nanoparticles for Oral Delivery: Targeted Nanoparticles with Peptidic Ligands for Oral Protein Delivery. *Advanced Drug Delivery Reviews* 2013, *65*, 822-832.

(145) Thubagere, A.; Reinhard, B. M. Nanoparticle-Induced Apoptosis Propagates through Hydrogen-Peroxide-Mediated Bystander Killing: Insights from A Human Intestinal Epithelium *in Vitro* Model. *ACS Nano.* 2010, *4*, 3611-3622.

(146) Veiseh, O.; Tang, B. C.; Whitehead, K. A.; Anderson, D. G.; Langer, R. Managing Diabetes with Nanomedicine: Challenges And Opportunities. *Nature Reviews Drug Discovery* 2015, *14*, 45-57.

(147) des Rieux, A.; Fievvez, V.; Theate, I.; Mast, J.; Preat, V.; Schneider, Y.-J. An Improved in Vitro Model of Human Intestinal Follicle-Associated Epithelium to Study Nanoparticle Transport by M Cells. *European Journal of Pharmaceutical Sciences* 2007, *30*, 380-391.

(148) Yacobi, N. R.; Demaio, L.; Xie, J.; Hamm-Alvarez, S. F.; Borok, Z.; Kim, K.-J.; Crandall, E. D. Polystyrene Nanoparticle Trafficking across Alveolar Epithelium. *Nanomedicine* 2008, *4*, 139-145.

(149) Bannunah, A. M.; Vllasaliu, D.; Lord, J.; Stolnik, S. Mechanisms of Nanoparticle Internalization and Transport across An Intestinal Epithelial Cell Model: Effect of Size And Surface Charge. *Molecular Pharmaceutics* 2014, *11*, 4363-4373.

(150) Behrens, I.; Pena, A. I. V.; Alonso, M. J.; Kissel, T. Comparative Uptake Studies of Bioadhesive and Non-Bioadhesive Nanoparticles in Human Intestinal Cell Lines and Rats: The Effect of Mucus on Particle Adsorption And Transport. *Pharmaceutical Research* 2002, *19*, 1185-1193.

(151) Mahler, G. J.; Esch, M. B.; Tako, E.; Southard, T. L.; Archer, S. D.; Glahn, R. P.; Shuler, M. L. Oral Exposure to Polystyrene Nanoparticles Affects Iron Absorption. *Nature Nanotechnology* 2012, *7*, 264-271.

(152) Cortes, C.; Domenech, J.; Salazar, M.; Pastor, S.; Marcos, R.; Hernandez, A. Nanoplastics as A Potential Environmental Health Factor: Effects of Polystyrene Nanoparticles on Human Intestinal Epithelia Caco-2 Cells. *Environmental Science: Nano* 2020, *7*, 272.

(153) Paget, V.; Dekali, S.; Kortulewski, T.; Grall, R.; Gamez, C.; Blazy, K.; Aguerre-Chariol, O.; Chevillard, S.; Braun, A.; Rat, P.; Lacroix, G. Specific Uptake And Genotoxicity Induced by Polystyrene Nanobeads with Distinct Surface Chemistry on Human Lung Epithelial Cells and Macrophages. *PLoS One* 2015, *10*, e0123297.

(154) Pinto, M.; Robine-Leon, S.; Appay, M. D. Enterocyte-Like Differentiation And Polarization of The Human-Colon Carcinoma Cell-Line Caco-2 in Culture. *Biology of the Cell* 1983, *47*, 323-330.

(155) Artursson, P. Epithelial Transport of Drugs in Cell-Culture .I: a Model for Studying The Passive Diffusion of Drugs over Intestinal Absorptive (Caco-2) Cells. *Journal of Pharmaceutical. Sciences* 1990, *79*, 476-482.

(156) Hilgers, A. R.; Conradi, R.; Burton, P.S. Caco-2 Cell Monolayers as A Model for Drug Transport across The Intestinal Mucosa. *Pharmaceutical Research* 1990, *7*, 902-910.

(157) Artursson, P.; Borchardt, R. T. Intestinal Drug Absorption And Metabolism in Cell Cultures: Caco-2 and Beyond. *Pharmaceutical Research* 1997, *14*, 1655-1658.

(158) Konsoula, R.; Barile, F. A. Correlation of *in Vitro* Cytotoxicity with Paracellular Permeability in Caco-2 Cells. *Toxicology In Vitro* 2005, *19*, 675-684.

(159) Okada, T.; Narai, A.; Matsunga, S.; Fusetani, N.; Shimizu, M. Assessment of The Marine Toxins by Monitoring The Integrity of Human Intestinal Caco-2 Cell Monolayers. *Toxicology In Vitro* 2000, *14*, 219-226.

(160) Sha, X.; Yan, G.; Wu, Y.; Li, J.; Fang, X. Effect of Self-Microemulsifying Drug Delivery Systems Containing Labrasol on Tight Junctions in Caco-2 Cells. *European Journal of Pharmaceutical Sciences* 2005, *24*, 477-486.

(161) Domenech, J.; Hernandez, A.; Rubio, L.; Marcos, R.; Cortes, C. Interactions of Polystyrene Nanoplastics with *in Vitro* Models of The Human Intesintal Barrier. *Archives of Toxicology* 2020, *94*, 2997-3012.

(162) Liu, S.; Wu, X.; Gu, W.; Yu, J.; Wu, B. Influence of The Digestive Process on Intestinal Toxicity of Polysytrene Microplastics as Determined by *in Vitro* Caco-2 Models. *Chemosphere* 2020, *356*, 127204.

(163) Win, K. Y.; Feng, S.-S. Effects of Particle Size And Surface Coating on Cellular Uptake of Polymeric Nanoparticles for Oral Delivery of Anticancer Drugs. *Biomaterials* 2005, *26*, 2713-2722.

(164) Hu, C.-S.; Chiang, C.-H.; Hong, P.-D.; Yeh, M.-K. Influence of Charge on FITC-BSA-Loaded Chondroitin Sulfate-Chitosan Nanoparticles upon Cell Uptake in Human Caco-2 Cell Monolayers. *International Journal of Nanomedicine* 2012, *7*, 4861-4872.

(165) Loh, J. W.; Saunders, M.; Lim, L.-Y. Cytotoxicity of Monodispersed Chitosan Nanoparticles against Caco-2 Cells. *Toxicology and Applied Pharmacology* 2012, *262*, 273-282.

(166) Bouwmeester, H.; Poortman, J.; Peters, R. J.; Wijma, E.; Kramer, E.; Makama, S.; Puspitaninganindita, K.; Marvin, H. J. P.; Peijnenburg, A. A. C. M.; Hendriksen, P. J. M. Characterization of Translocation of Silver Nanoparticles And Effects on Whole-Genome Gene Expression Using an *in Vitro* Intestinal Epithelium Coculture Model. *ACS Nano* 2011, *5*, 4091-4103.

(167) Wu, S.; Wu, M.; Tian, D.; Qiu, L.; Li, T. Effects of Polystyrene Microbeads on Cytotoxicity And Transcriptomic Profiles in Human Caco-2 Cells. *Environmental Toxicology* 2020, *35*, 495-506.

(168) Jin, C.; Liu, Y.; Sun, L.; Chen, T.; Zhang, Y.; Zhao, A.; Wang, X.; Cristau, M.; Wang, K.; Jia, W. Metabolic Profiling Reveals Disorder of Carbohydrate Metabolism in Mouse Fibroblast Cells Induced by Titanium Dioxide Nanoparticles. *Journal of Applied Toxicology* 2013, *33*, 1442-1450.

(169) Bo, Y.; Jin, C.; Liu, Y.; Yu, W.; Kang, H. Metabolomic Analysis on The Toxicological Effects of TiO_2 Nanoparticles in Mouse Fibroblast Cells: from The Perspective of Perturbations in Amino Acid Metabolism. *Toxicology Mechanisms and Methods* 2014, *24*, 461-469.

(170) Zhang, J. L.; Zhou, Z. P.; Pei, Y.; Xiang, Q. Q.; Chang, X. X.; Ling, J.; Shea, D.; Chen, L. Q. Metabolic Profiling of Silver Nanoparticle Toxicity in Microcystis Aeruginosa. *Environmental Science: Nano* 2018, *5*, 2519.

(171) Shim, W.; Paik, M. J.; Nguyen, D.-T.; Lee, J.-K.; Lee, Y.; Kim, J.-H.; Shin, E.-H.; Kang, J. S.; Jung, H.-S.; Choi, S.; Park, S.; Shim, J. S., Lee, G. Analysis of Changes in Gene Expression And Metabolic Profiles Inudced by Silica-Coated Magnetic Nanoparticles. *ACS Nano* 2012*, 6*, 7665-7680.

(172) Plou, J.; Garcia, I.; Charconnet, M.; Astobiza, I.; Garcia-Astrain, C.; Matricardi, C.; Mihi, A.; Carracedo, A.; Liz-Marzan, L. M. Multiplex SERS Detection of Metabolic Alterations in Tumor Extracellular Media. *Advced Functional Materials* 2020, *30*, 1910335.

(173) Lussier, F.; Missirlis, D.; Spatz, J. P.; Masson, J.-F. Machine-Learning-Driven Surface-Enhanced Raman Scattering Optophysiology Reveals Multiplexed Metabolite Gradients Near Cells. *ACS Nano* 2019, *13*, 1403-1411.

(174) Ali, M. R. K.; Wu, Y.; Han, T.; Zang, X.; Xiao, H.; Tang, Y.; Wu, R.; Fernandez, F. M.; EI-Sayed, M. A. Simultaneous Time-Dependent Surface- Enhanced Raman Spectroscopy, Metabolomics, And Proteomis Reveal Cancer Cell Death Mechanisms Associated with Gold Nanorod Photothermal Therapy. *Journal of the American. Chemical Society* 2016, *38*, 15434-15442.

(175) Premasiri, W. R.; Lee, J. C.; Sauer-Budge, A.; Theberge, R.; Costello, C. E.; Ziegler, L. D. The Biochemical Origins of The Surface-Enhanced Raman Spectra Of Bacteria: A Metabolomics Profiling by SERS. *Analytical. Bioanalytical Chemistry* 2016, *408*, 4631-4647.

(176) Shalabaeva, V.; Lovato, L.; La Rocca, R.; Messina, G. C.; Dipalo, M.; Miele, E.; Perrone, M.; Gentile, F.; De Angelis, F. Time Resolved And Label Free Monitoring of Extracellular Metabolites by Surface Enhanced Raman Spectroscopy. *PLoS One* 2017, *12*, e0175581.

(177) Sherman, L.M.; Petrov, A. P.; Karger, L. F. P.; Tetrick, M. G.; Dovichi, N. J.; Camden, J. P. A Surface-Enhanced Raman Spectroscopy Database of 63 Metabolites. *Talanta* 2020, *210*, 120645.

(178) Lee, C. H.; Hankus, M. E.; Tian, L.; Pellegrino, P. M.; Singamaneni, S. Highly Sensitive Surface Enhanced Raman Scattering Substrates

Based on Filter Paper Loaded with Plasmonic Nanostrucutres. *Analytical Chemistry* 2011, *83*, 8953-8958.

(179) Haynes, C. L.; McFarland, A. D.; Van Duyne, R. P. Surface-Enhanced Raman Spectroscopy. *Analytical Chemistry* 2005, *77*, 338a-346a.

(180) Yan, B.; Thubagere, A.; Premasiri, R. W.; Ziegler, L. D.; Dal Negro, L.; Reinhard, B. M. Engineered SERS Substrates with Multiscale Signal Enhancement: Nanoparticle Cluster Arrays. *ACS Nano* 2009, *3*, 1190 - 1202.

(181) Yang, L.; Yan, B.; Premasiri, R. W.; Ziegler, L. D.; Dal Negro, L.; Reinhard, B. M. Engineering Nanoparticle Cluster Arrays for Bacterial Biosensing: The Role of the Building Block in Multiscale SERS Substrates. *Advanced Functional Materials* 2010, *20*, 2619-2628.

(182) Yan, B.; Boriskina, S. V.; Reinhard, B. M. Design and Implementation of Noble Metal Nanoparticle Cluster Arrays for Plasmon Enhanced Biosensing. *Journal of Physical Chemistry C* 2011, *115*, 24437-24453.

(183) Cedervall, T.; Lynch, I.; Lindman, S.; Berggard, T.; Thulin, E.; Nilsson, H.; Dawson, K. A.; Linse, S. Understanding The Nanoparticle-Protein Corona Using Methods to Quantify Exchange Rates And Afinities of Proteins to Nanoparticles. *Proceedings of the National Academy of Sciences* 2007, *104*, 2050-2055.

(184) Lundqvist, M.; Stigler, J.; Elia, G.; Lynch, I.; Cedervall, T.; Dawson, K. A. Nanoparticle Size And Surface Properties Determine The Protein Corona with Possible Implications for Biological Impacts. *Proceedings of the National Academy of Sciences* 2008, *105*, 14265-14270.

(185) Xu, F.; Reiser, M.; Yu, X.; Gummuluru, S.; Wetzler, L.; Reinhard, B. M. Lipid Mediated Targeting with Membrane-Wrapped Nanoparticles in The Presence of Corona Formation. *ACS Nano* 2016, *10*, 1189-1200.

(186) He, B.; Lin, P.; Jia, Z.; Du, W.; Qu, W.; Yuan, L.; Dai, W.; Zhang, H.; Wang, X.; Wang, J.; Zhang, X.; Zhang, Q. The Transport Mechanisms of Polymer Nanoparticles in Caco-2 Epithelial Cells. *Biomaterials* 2013, *34*, 6082-6098.

(187) Song, Q.; Yao, L.; Huang, M.; Hu, Q.; Lu, Q.; Wu, B.; Qi, H.; Rong, Z.; Jiang, X.; Gao, X.; Chen, J.; Chen, H. Mechanisms of Transcellular Transport of Wheat Germ Agglutinin-Functionalized Polymeric Nanoparticles in Caco-2 Cells. *Biomaterials* 2012, *33*, 6769-6782.

(188) Sheng, J.; Han, L.; Qin, J.; Ru, G.; Li, R.; Wu, L.; Cui, D.; Yang, P.; He, Y.; Wang, J. *N*-Trimethyl Chitosan Chloride-Coated PLGA Nanoparticles Overcoming Multiple Barriers to Oral Insulin Absorption. *ACS Applied Material Interfaces* 2015, *7*, 15430-15441.

(189) van der Zande, M.; Undas, A. K.; Kramer, E.; Monopoli, M. P.; Peters, R. J.; Garry, D.; Fernandes, E. C. A.; Hendriksen, P. J.; Marvin, H. J. P.; Peijnenburg, A. A.; Bouwmeester, H. Different Responses of Caco-2 And MCF-7 Cells to Silver Nanoparticles Are Based on Highly Similar Mechanisms of Action. *Nanotoxicology* 2016, *10*, 1431-1441.

(190) Zhang, W.; Kalive, M.; Capco, D. G.; Chen, Y. Adsorption of Hematite Nanoparticles onto Caco-2 Cells And The Cellular Impairments: Effects of Particle Size. *Nanotechnology* 2010, *21*, 355103.

(191) Gerloff, K.; Fenoglio, I.; Carella, E.; Kolling, J.; Albrecht, C.; Boots, A. W.; Forster, I.; Schins, R. P. Distinctive Toxicity of TiO_2 Rutile/Anatase Mixed Phase Nanoparticles On Caco-2 Cells. *Chemical Research in Toxicology* 2012, *25*, 646-655.

(192) Zijno, A.; De Angelis, I.; De Berardis, B.; Andreoli, C.; Russo, M. T.; Pietraforte, D.; Scorza, G.; Degan, P.; Ponti, J.; Rossi, F.; Barone, F. Different Mechanisms Are Involved in Oxidative DNA Damage and Genotoxicity Induction by ZnO And TiO_2 Nanoparticles In Human Colon Carcinoma Cells. *Toxicology In Vitro* 2015, *29*, 1503-1512.

(193) Abramov, E.; Cassiola, F.; Schwob, O.; Karsh-Bluman, A.; Shapero, M.; Ellis, J.; Luyindula, D.; Adini, I.; D'Amato, R. J.; Benny, O. Cellular Mechanism of Oral Absorption of Solidified Polymer Micelles. *Nanomedicine* 2015, *11*, 1993-2002.

(194) Tenzer, S.; Docter, D.; Kuharev, J.; Musyanovych, A.; Fetz, V.; Hecht, R.; Schlenk, F.; Fischer, D.; Kiouptsi, K.; Reinhardt, C.; Landfester, L.; Schild, H., Maskos, M.; Knauer, S. K.; Stauber, R. H. Rapid Formation of Plasma Protein Corona Critically Affects Nanoparticle Pathophysiology. *Nature Nanotechnology* 2013, *8*, 772-781.

(195) Kim, H. R.; Andrieux, K.; Gil, S.; Taverna, M.; Chacun, H.; Desmaele, D.; Taran, F.; Georgin, D.; Couvreur, P. Translocation of Poly(ethylene glycol-*co*-hexadecyl)cyanoacrylate Nanoparticles into Rat Brain Endothelial Cells: Role of Apolipoproteins in Receptor-Mediated Endocytosis. *Biomacromolecules* 2007, *8*, 793-799.

(196) Yacobi, N. R.; Malmstadt, N.; Fazollahi, F.; DeMaio, L.; Marchelletta, R.; Hamm-Alvarez, S. F.; Borok, Z.; Kim, K.-J.; Crandall, E. D. Mechanisms of Alveolar Epithelial Translocation of A Defined Population of Nanoparticles. The *American Journal of Respiratory Cell and Molecular Biology* 2010, *42*, 604-614.

(197) Meindl, C.; Ohlinger, K.; Ober, J.; Roblegg, E.; Frohlich, E. Comparsion of Fluorescence-Based Methods to Determine Nanoparticle Uptake by Phagocytes And Non-Phagocytic Cells *in Vitro*. *Toxicology* 2017, *378*, 25-36.

(198) Kumar, R.; Roy, I.; Ohulchanskyy, T. Y.; Goswami, L. N.; Bonoiu, A. C.; Bergey, E. J., Tramposch, K. M.; Maitra, A.; Prasad, P. N. Covalently Dye-Linked, Surface-Controlled, And Bioconjugated Organically Modified Silica Nanoparticles as Targeted Probes for Optical Imaging. *ACS Nano* 2008, *2*, 449-456.

(199) Abstiens, K.; Figueroa, S. M.; Gregoritza, M.; Goepferich, A. M. Interaction of Functionalized Nanoparticles with Serum Proteins And Its Impact on Colloidal Stability And Cargo Leaching. *Soft Matter* 2019, *15*, 709-720.

(200) Lesniak, A.; Salvati, A.; Santos-Martinez, M. J.; Radomski, M. W.; Dawson, K. A.; Aberg, C. Nanoparticle Adhesion to The Cell Membrane And Its Effect on Nanoparticle Uptake Efficiency. *Journal of the American Chemical. Society* 2013, *135*, 1438-1444.

(201) Gerloff, K.; Albrecht, C.; Boots, A. W.; Foster, I.; Schins, R. P. F. Cytotoxicity And Oxidative Damage by Nanoparticles in Human Intestinal Caco-2 Cells. *Nanotoxicology* 2009, *3*, 355-364.

(202) Gerloff, K.; Pereira, D. I. A.; Faria, N.; Boots, A. W.; Kolling, J.; Forster, I.; Albrecht, C.; Powell, J. J.; Schins, R. P. F. Influence of Simulated Gastrointestinal Conditions on Particle-Induced Cytotoxicity And Interleukin-8 Regulation in Differentiated And Undifferentiated Caco-2 Cells. *Nanotoxicology* 2013, *7*, 353-366.

(203) Kang, T.; Guan, R.; Chen, X.; Song, Y.; Jiang, H.; Zhao, J. *In Vitro* Toxicity of Different-Sized ZnO Nanoparticles in Caco-2 Cells. *Nanoscale Research Letters* 2013, *8*, 496.

(204) Li, L.; Xiao, R.; Wang, Q.; Rong, Z.; Zhang, X.; Zhou, P.; Fu, H.; Wang, S.; Wang, Z. SERS Detection of Radiation Injury Biomarkers in Mouse Serum. *RSC Advances* 2018, *8*, 5119.

(205) Wang, Z.-y.; Li, W.; Gong, Z.; Sun, P.-r.; Zhou, T.; Cao, X.-w. Detection of IL-8 in Human Serum Using Surface-Enhanced Raman Scattering Coupled with Highly-Branched Gold Nanoparticles And Gold Nanocages. *New Journal of Chemistry* 2019, *43*, 1733.

(206) Shalaev, V. M.; Botet, R.; Tsai, D. P.; Kovacs, J.; Moskovits, M. Fractals: Localization of Dipole Excitations and Giant Optical Polarizabilities. *Physica A* 1994, *207*, 197-207.

(207) Yan, B.; Boriskina, S. V.; Reinhard, B. M. Optimizing Gold Nanoparticle Cluster Configurations ($n \leq 7$) for Array Applications. *Journal of Physical Chemistry C* 2011, *115*, 4578-4583.

(208) Sun, F.; Ella-Menye, J.-R.; Galvan, D. D.; Bai, T.; Hung, H.-C.; Chou, Y.-N.; Zhang, P.; Jiang, S.; Yu, Q. Stealth Surface Modification of Surface-Enhanced Raman Scattering Substrates for Sensitive And Accurate Detection in Protein Solutions. *ACS Nano* 2015, *9*, 2668-2676.

(209) Sun, F.; Hung, H.-C.; Sinclair, A.; Zhang, P.; Bai, T.; Galvan, D. D.; Jain, P.; Li, B.; Jiang, S.; Yu, Q. Hierarchical Zwitterionic Modification of A SERS Substrate Enable Real-Time Drug Moniotring in Blood Plasma. *Nature Communication* 2016, *7*, 13437.

(210) Yonzon, C. R.; Haynes, C. L.; Zhang, X.; Walsh, J. T.; Van Duyne, R. P. A Glucose Biosensor Based on Surface-Enhanced Raman Scattering: Improved Partition Layer, Temporal Stability, Reversibility , And Resistance to Serum Protein Interference. *Analytical Chemistry* 2004, *76*,78-85.

(211) Miranda, O. R.; Creran, B.; Rotello, V. M. Array-Based Sensing with Nanoparitles: "Chemcial Noses" for Sensing Biomolecules And Cell Surfaces. *Current Opinion in Chemical Biology* 2010, *14*, 728-736.

(212) Kim, N.; Thomas, M. R.; Bergholt, M. S.; Pence, I. J.; Seong, H.; Charchar, P.; Todorova, N.; Nagelkerke, A.; Belessiotis-Richards, A.; Payne, D. J.; Gelmi, A.; Yarovsky, I.; Stevens, M. M. Surface Enhanced Raman Scattering Artificial Nose for High Dimensionality Fingerpriting. *Nature Communication* 2020, *11*, 13615.

(213) Yan, B.; Hong, Y.; Chen, T.; Reinhard, B. M. Monitoring Enzymatic Degradation of Pericellular Matrices through SERS Stamping. *Nanoscale* 2012, *4,* 3917-3925.

(214) van der Maaten, L.; Hinton, G. Visualizing Data Using t-SNE. *Journal of Machine Learning Research* 2008, *9*, 2579-2605.

(215) Lever, J.; Krzywinski, M.; Altman, N. Principal Component Analysis. *Nature Methods* 2017, *14*, 641-642.

(216) Ye, J.; Janardan, R.; Li, Q. Two-Dimensional Linear Discriminat Analysis. In *Advances in Neural Information Processing Systems* 2005, *17*, 1569-1576.

(217) Lee, J. S.; Wang, R. X.; Alexeev, E. E.; Lanis, J. M.; Battista, K. D.; Glover, L. E.; Colgan, S. P. Hypoxanthine Is A Checkpoint Stress Metabolite in Colonic Epithelial Energy Modulation And Barrier Function. *Journal of Biological Chemistry* 2017, *293*, 6039-6051.

(218) Antonioli, L.; Blandizzi, C.; Pacher, P.; Hasko, G. Immunity, inflammation and Cancer: A Leading Role for Adenosine. *Nature Reviews Cancer* 2013, *1*3, 842-857.

(219) Tan, E. Y.; Richard, C. L.; Zhang, H.; Hoskin, D. W.; Blay, J. Adenosine Downregulates DPPIV on HT-29 Colon Cancer Cells by Stimulating Protein Tyrosine Phosphatase(S) and Reducing ERK1/2 Activity via A Novel Pathway. *The American Journal of Physiology-Cell Physiology* 2006, *291*, C433-C444.

(220) Chen, C.; Hsu, A. High Dimensional Data Visualization by PCA and LDA, Hsinchu, Taiwan: National Tsing Hua University.

Curriculum Vitae

Qianyun Zhang

EDUCATION
Boston University, Boston, MA
September 2015-Present
PhD Candidate in Chemistry

University of Minnesota-Twin Cities, Minneapolis, MN
September 2011- May 2015
Bachelor of Science in Chemistry, Minor in Mathematics

RESEARCH EXPERIENCE
Advisor: Björn M. Reinhard, PhD, Boston University, Boston, MA
Metabolomics study of Nanoplastic-induced Damage in an Intestinal Membrane
Understanding EGFR Signaling Pathway via Lipid Nanoparticle

WORK EXPERIENCE
Summer Intern –Novartis Institute for Biomedical Research
May 2019-August 2019

AWARDS
2018 3 Minute Thesis Competition Finalists
BU Nanotechnology Innovation Center Best Poster Prize
GRS Research Fellowship Scholarship and Fellow Stipend
2014 APS/DFD Gallery of Fluid Motion Award Winners
Gold Global Excellence Scholarship
Undergraduate Research Opportunities Program Award

PUBLICATIONS
(2018) Zhang Q, Reinhard B.M. Ligand density and nanoparticle clustering cooperate in the multivalent amplification of EGF Receptor Activation. *ACS Nano*.
(2015) Zhang Q, Gao M, Zhao R, Cheng X. Scaling of liquid-drop impact craters in wet granular media. *Phys. Rev. E*.
(2014) Zhao R, Zhang Q, Tjugito H, Cheng X. Granular Impact cratering by liquid drops: Understanding raindrop imprints through an analogy to asteroid strikes. *PNAS*.
(2014) Zhao R, Zhang Q, Tjugito H, Cheng X. Raindrop impact on sandy surface. 2014 DFD Virtual Pressroom. *APS Physics*.